Assessment of tibial fracture healing using dual energy X-ray absorptiometry

Cook, Juliette Emma

ASSESSMENT OF TIBIAL FRACTURE HEALING USING DUAL ENERGY X-RAY ABSORPTIOMETRY

Submitted by

Juliette Emma Cook

to the University of Durham

as a thesis for the degree of

Master of Science

in the School of Engineering

and Computer Science

December 1993

I certify that all the material in this thesis which is not my own work has been identified and that no material is included for which a degree has previously been conferred upon me.

LIST OF CONTENTS

	Page
List of Contents	*i*
List of Figures	*iv*
List of Tables	*iix*
Abstract	*x*
Acknowledgements	*xii*
CHAPTER 1 — Introduction and Literature Review	*1*
1.1 Structure and Function of Bone	*2*
1.1.1 Structure	*2*
1.1.2 Bone Cells	*5*
1.1.3 Collagen and Calcification	*7*
1.2 Fracture Healing	*8*
1.2.1 Inflammatory Phase	*10*
1.2.2 Cartilaginous Phase	*11*
1.2.3 Mineralisation Phase	*12*
1.2.4 Remodelling Phase	*13*
1.2.5 Speed of Healing	*15*
1.3 Callus Properties	*16*
1.4 Post-Trauma Osteoporosis	*19*
1.5 Fracture Treatment and Technique	*20*
1.5.1 Bracing and Casts	*21*
1.5.2 Intramedullary Nailing	*21*
1.5.3 Plating	*22*
1.5.4 External Fixation	*23*

Page

1.6 Fracture Healing Measurement *24*

1.6.1 Ultrasound *25*

1.6.2 Stresswave Propagation *26*

1.6.3 Resonant Vibration *27*

1.6.4 Fracture Stiffness Measurements *27*

1.6.5 Scintigraphy *28*

1.6.6 Computed Tomography *29*

1.6.7 Quantitative Radiographic Densitometry *30*

1.6.8 Photon Absorptiometry *31*

1.6.9 Dual Energy X-ray Absorptiometry *32*

1.7 Dual Energy X-ray Absorptiometry *33*

1.7.1 Theory *34*

1.7.2 Optimum Energy Levels *39*

1.7.3 Precision and Accuracy *40*

1.7.4 DXA Systems *42*

1.7.5 Scanning Phantom Materials *45*

1.8 Phantoms *46*

1.8.1 Tissue Equivalence *47*

1.8.2 Phantom Materials *51*

CHAPTER 2 — Phantom Trials *53*

2.1 Materials and Methodology *53*

2.1.1 Phantoms *53*

2.1.2 Scanner *56*

Page

2.2 Results *57*

2.2.1 Soft Tissue Effects *57*

2.2.2 ROI Size *61*

2.2.3 Relationship of Measured and True Density *63*

2.2.4 Gap Size and Orientation *67*

2.2.5 Low Density *75*

2.3 Summary *77*

CHAPTER 3 — Patient Trials *79*

3.1 Patients and Methodology *79*

3.1.1. Patients *79*

3.1.2. Scanner *80*

3.1.3. Analysis *82*

3.2 Results *84*

3.2.1 Lunar Software *84*

3.2.2 Reproducibility *85*

3.2.3 Healthy Non-fractured Limb *88*

3.2.4 External Fixation *89*

3.2.5 Internal Fixation *110*

3.2.6 Complex Fixation *121*

CHAPTER 4 — Discussion *129*

CHAPTER 5 — Conclusions and Future Work *139*

REFERENCES *142*

LIST OF FIGURES

Figure		*Page*
1.1.	Mature compact bone.	*3*
1.2.	Three-dimensional representation of the diaphyseal cortex in a long bone.	*4*
1.3.	Bone cells.	*6*
1.4.	The effect of fracture on the medullary and periosteal blood supply to the tibia.	*9*
1.5.	The inflammatory phase.	*10*
1.6.	The proliferative phase.	*12*
1.7.	Direct and indirect healing.	*13*
1.8.	The cutting cone.	*14*
1.9.	The remodelling phase.	*15*
1.10.	Variation with energy of the linear attenuation coefficient for soft tissue and cortical bone.	*38*
1.11.	Transmission of monoenergetic photons through soft tissue.	*39*
1.12.	Dual-kV spectrum after transmission.	*43*
1.13.	Principles of K-edge filtration.	*44*
1.14.	Photon interactions and attenuation mechanisms.	*48*
1.15.	The interaction probability by photoelectric or Compton effect with the atomic number of a material.	*50*
2.1.	The aluminium and perspex phantoms A, B, and C.	*54*
2.2.	The phantom tibial fractures 1, 2 and 3.	*55*
2.3.	The variation of BMD with aluminium thickness and phantom soft tissue material.	*58*

Figure		Page
2.4.	The effect of different phantom soft tissue materials on the BMD output.	*59*
2.5.	The change in coefficient of variation for an aluminium phantom analysed using different ROI sizes.	*62*
2.6.	The change in average bone mineral density for an aluminium phantom analysed using different ROIS sizes.	*62*
2.7.	The variation of BMD along the length of an aluminium and perspex phantom with a transverse fracture gap.	*68*
2.8.	A comparison of the theoretical and experimental BMD values across a phantom fracture gap.	*69*
2.9.	The oblique fracture phantom, 3.	*71*
2.10.	The detection of an oblique fracture gap orientated parallel to the x-ray beam.	*72*
2.11.	The detection of an oblique fracture gap orientated perpendicular to the x-ray beam.	*73*
2.12.	The theoretical variation of BMD for an aluminium and perspex phantom with an oblique fracture gap.	*74*
2.13.	Comparison between the actual mass of calcium hydroxyapatite and the bone mineral content values given for the scanner.	*75*
2.14.	Comparison between the actual area density of calcium hydroxyapatite and the bone mineral density values given for the scanner.	*76*

Figure		Page
3.1.	Schematic representation of a fractured tibia showing the location of the regions of interest.	*83*
3.2.	BMD profile for Patient 12 with an intramedullary nail, analysed using the Lunar orthopaedic software.	*85*
3.3.	The coefficient of variation versus the bone mineral density obtained from the repeated scanning of a patient's fractured tibia.	*86*
3.4.	The variation of the standard deviation against the bone mineral density obtained from the repeated scanning of one fractured patient tibia.	*87*
3.5.	Bone mineral density profiles of the healthy, unfractured tibia for Patient 9.	*89*
3.6.	Lunar software computer display during analysis of Patient 3 with an external fixator.	*90*
3.7	BMD profile of Patient 1 with an external fixator.	*91*
3.8.	X-ray of Patient 1 showing the fractured tibia before fixation.	*92*
3.9.	X-ray of Patient 1 showing the fractured tibia after fixation.	*93*
3.10.	X-ray of Patient 1 showing the fractured tibia after removal of the fixator.	*95*
3.11	BMD profile of Patient 3 with an external fixator.	*97*
3.12	BMD profile of Patient 4 with an external fixator.	*99*
3.13	BMD profile of Patient 6 with an external fixator.	*101*
3.14.	X-ray of Patient 9 showing the fractured tibia before fixation.	*103*
3.15.	X-ray of Patient 9 showing the fractured tibia after fixation.	*104*
3.16	BMD profile of Patient 9 with an external fixator.	*105*
3.17	BMD profile of the unfractured limb for Patient 9.	*107*

Figure		*Page*
3.18.	BMD profile of Patient 10 with an external fixator.	*109*
3.19.	Lunar software computer display during analysis of Patient 2 with an intramedullary nail.	*110*
3.20	Lateral side BMD profile of Patient 2 with an intramedullary nail.	*112*
3.21	Medial side BMD profile of Patient 2 with an intramedullary nail.	*114*
3.22	Lateral side BMD profile of Patient 8 with an intramedullary nail.	*116*
3.23	Medial side BMD profile of Patient 8 with an intramedullary nail.	*117*
3.24.	X-ray of Patient 8 showing the fractured tibia before fixation.	*118*
3.25.	X-ray of Patient 8 showing the fractured tibia after 3 months with the fixator.	*120*
3.26.	Lunar software computer display during analysis of Patient 7 with an Ilizarov frame.	*121*
3.27.	BMD profile of Patient 5 with complex fixation.	*123*
3.28.	X-ray of Patient 7 showing the fractured tibia before fixation.	*125*
3.29.	X-ray of Patient 7 showing the fractured tibia after fixation with an Ilizarov fixator.	*126*
3.30.	BMD profile of Patient 7 with an Ilizarov fixator.	*127*
4.1.	Variation with time of the BMD across the fracture site.	*136*

LIST OF TABLES

Table		*Page*
1.1.	Mechanical properties of hard and soft tissues.	*17*
1.2.	Comparison of the techniques for the measurement of bone mass.	*41*
1.3.	Mass attenuation coefficients for biological and phantom equivalent materials.	*45*
1.4.	Elemental composition of hard and soft tissues by weight.	*49*
1.5.	Table of material densities.	*50*
2.1.	The acquisition data level settings of the forearm software for the phantom trials.	*56*
2.2.	The effects of varying the depth of water above the aluminium phantom on the value of BMD output by the scanner.	*60*
2.3.	Summary of the effects of varying the soft tissue substitutes with the aluminium phantom.	*60*
2.4.	Mass attenuation coefficients for biological and phantom equivalent materials.	*64*
2.5.	Theoretical relationship between phantom materials and bone mineral density output from scanner.	*65*
2.6.	Experimental relationship between phantom materials and bone mineral density output from scanner.	*66*
3.1.	Details of the type, location and fixation method used for 14 patients with tibial fractures.	*80*
3.2.	Table of the average standard deviation and coefficient of variation for the repeated scanning of 3 patients' unfractured tibias.	*88*
3.3.	The BMD values along the fractured tibia of Patient 1 expressed as a percentage of the BMD values obtained at the same location on 19-Feb-93.	*94*

Table		Page
3.4.	The BMD values along the fractured tibia of Patient 3 expressed as a percentage of the BMD values obtained at an equivalent location on the healthy contra-lateral limb 16-Jul-93.	*96*
3.5.	The BMD values along the fractured tibia of Patient 4 expressed as a percentage of the BMD values obtained at an equivalent location on the healthy contra-lateral limb 27-Jul-93.	*98*
3.6.	The BMD values along the fractured tibia of Patient 6 expressed as a percentage of the BMD values obtained at an equivalent location on the healthy contra-lateral limb on 18-May-93.	*100*
3.7.	The BMD values along the fractured tibia of Patient 9 expressed as a percentage of the BMD values obtained at an equivalent location on the healthy contra-lateral limb on 7-Sep-93.	*106*
3.8.	The BMD values along the fractured tibia of Patient 10 expressed as a percentage of the BMD values obtained at an equivalent location on the healthy contra-lateral limb on 2-Sep-93.	*108*
3.9.	The BMD values along the lateral and medial side of the fractured tibia of Patient 2 expressed as a percentage of the BMD values obtained at the same location on 18-Nov-92.	*111*
3.10.	The BMD values along the lateral and medial side of the fractured tibia of Patient 8 expressed as a percentage of the BMD values obtained at the same location on 15-Oct-92.	*119*
3.11.	The BMD values along the fractured tibia of Patient 7 expressed as a percentage of the BMD values obtained at an equivalent location on the healthy contra-lateral limb on 3-Feb-93.	*126*
4.1.	Summary of the results of the fracture healing study for the patients with external fixation.	*131*
4.2.	Summary of the results of the fracture healing study for the patients with intramedullary nailing.	*134*

ABSTRACT

Assessment of Tibial Fracture Healing using Dual Energy X-Ray Absorptiometry

The assessment of fracture healing is largely a matter of clinical judgement, often based on observing x-rays showing the formation of bridging callus or obscuration of the fracture line and an impression of fracture stiffness obtained by manual loading. In circumstances where these assessment methods are compromised, for example in fractures stabilised using either external fixation or intramedullary nailing, the determination of healing can be problematic. Dual Energy X-ray Absorptiometry (DXA) provides a quick, non-invasive and quantitative method of measuring bone density, which could enable the change in mineral content at a healing site to be monitored. This study evaluated the viability of using DXA to assess the healing of tibial fractures stabilised using intramedullary nails and external fixators.

Trials have been undertaken on a Lunar DPX-L scanner situated at South Cleveland Hospital, Middlesbrough. Aluminium and hydroxyapatite phantoms have been used to determine the accuracy, sensitivity and reproducibility of the DXA measurements. Small fracture gaps of less than 0.05 mm were detectable on both simulated transverse and oblique fractures. BMD values which one might expect at a fracture site could be accurately measured down to 0.16 g cm^{-2}

14 Patients with tibial fractures (6 with intramedullary nails and 8 with external fixators) have been measured at 4 week intervals following trauma. The bone mineral

density (BMD) at regions of interest along the fractured tibial shaft were compared to the non-fractured contra-lateral. Anatomical landmarks were used to relocate the regions of interest between scans and good reproducibility of results (coefficient of variation = 3.36 %) was obtained. After an initial fall in the first month, the BMD at the fracture site gradually increased to the original unfractured value by approximately the fifth month post-fracture. Proximal and distal to the trauma site there was a gradual decrease in BMD in all of the patients, which persisted for about 5 months post-fracture.

ACKNOWLEDGEMENTS

I would like to acknowledge and thank my supervisor, Dr. J.L.Cunningham for his continued enthusiasm, support and advice, especially during the writing of this thesis.

The author extends her thanks also to Mrs Bates, Dr. Fordham, Mr. Muckle, and Mrs Pitcher of South Cleveland hospital in Middlesbrough, for their invaluable help with this project.

Finally I would like to acknowledge the Wishbone Trust of the British Orthopaedic Association who have funded this study.

CHAPTER 1

Introduction and Literature Review

The assessment of fracture healing remains largely a matter of clinical judgement based upon a subjective impression of fracture stiffness made by manual loading, and an assessment of radiological union by observing the presence of bridging callus or the obscuration of the fracture line. In certain circumstances the fracture management method may compromise the qualitative assessment by both manual sensing and radiographic appearance, for example in fractures managed by external skeletal fixation or intramedullary nailing. As a consequence timing the removal of the fixator may be problematic. In certain long bone fractures, of which the tibial shaft is a prime example, fracture union may not progress satisfactorily and despite modern methods of treatment the rate of non-union or delayed union remains high (Oni *et al.*, 1988). A reliable non-invasive and accurate method of evaluating the union of fractures would be a useful tool in avoiding unnecessarily long periods of immobilisation and treatment. Conversely if an early signal could be identified which indicated impending delayed or non-union, surgical intervention could occur at an earlier stage and improve patient rehabilitation time (Lewallen *et al.*, 1988).

1.1 Structure and Function of Bone

The human skeleton contains on average 206 bones. In combination they support the soft tissues, protect the internal organs from damage, provide levers and struts for movement and store a supply of vital minerals for the body. Various requirements imposed upon the skeleton have resulted in specialised bony elements being developed ranging from the large, elongated bones used for support, to the small, dense bones in the ear used to transmit sound waves. Wolff's law states that the physical characteristics of bone are matched to the routine structural demands placed upon it (Wolff, 1892). All bones share a similar structure, an outer shell of cortical bone surrounding a body of internal cancellous bone.

1.1.1 Structure

Three types of bone can be identified. Woven bone which has randomly organised collagen fibres, lamellar bone which has highly ordered collagen bundles and cancellous bone.

Woven bone is usually present at sites where ligaments or tendons attach to the bone and in fracture callus. It is the type of bone deposited in any initial bone formation, for example where rapid repair is needed. In general it has a low and unevenly distributed mineral content. There are more osteocytes present than in lamellar bone and the canaliculae also vary in size and orientation (Gray, 1964).

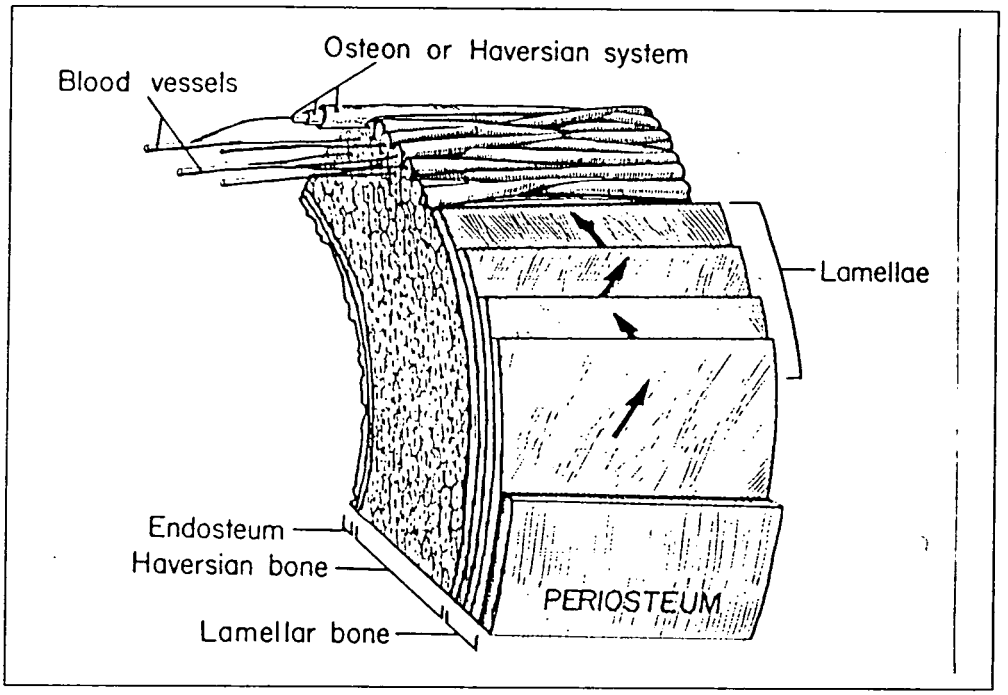

Figure 1.1. Mature compact bone. The outer region is lamellar bone, made up of circumferential lamellae. The fibre orientation varies from lamella to lamella. The inner region is Haversian bone, in which blood vessels are surrounded by concentric tubes of bone tissue. Its basic unit is the osteon, a vascular canal plus its surrounding rings (From Shipman *et al.*, 1985).

Lamellar bone, which is mature bone, has a laminated structure whether present in cortical or cancellous bone. The collagen fibres form bundles called lamellae which organise themselves in the manner shown in Figure 1.1. The basic unit of lamellar bone is the osteon, in which 15-20 lamellae are arranged in concentric tubes around an opening for a blood vessel. The vascular canals in osteons form the Haversian system which supplies nourishment to the bone tissue. The Haversian canals are oriented more or less longitudinally within the bone and are connected to each other, to the marrow cavity and to the surface of the skeletal element in a vascular network called the Volkmann's canals. The Volkmann's canals are transversely orientated and are not surrounded by concentric lamellae (Figure 1.2.)

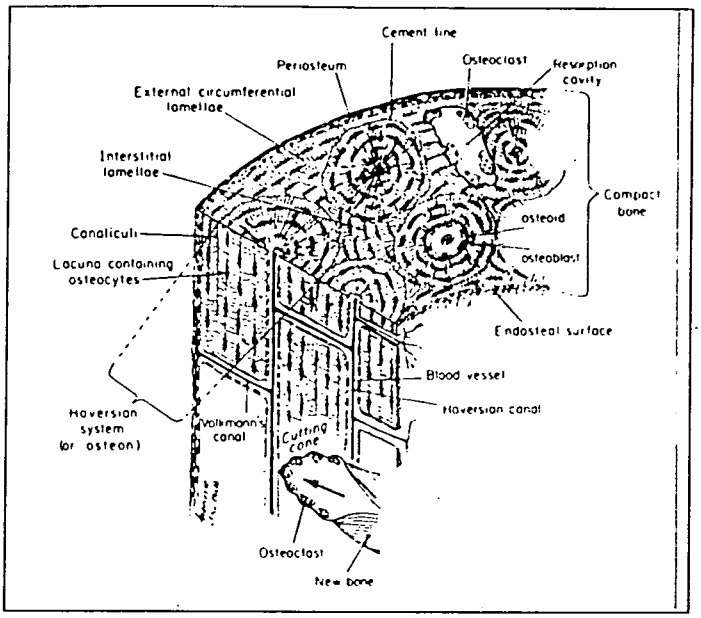

Figure 1.2. Three-dimensional representation of the diaphyseal cortex in a long bone showing both the transverse and the longitudinal structure (From Albright *et al.*, 1987).

Fine cancellous bone appears where transient reinforcement is needed and remodelling cannot occur rapidly enough to produce bone of sufficient strength. For example it may appear in the jaw of an animal when a new tooth is erupting and the stresses involved in chewing have increased. The surface of fine cancellous bone is ridged which is caused by small vascular canals being separated by small ridges of new bone.

Long bones are comprised of two types of bony tissue, cortical and cancellous. Cortical (or compact) bone makes up the diaphysis and the shell that surrounds the metaphyses (White, 1991). It has a porosity of less than 15 % (Le Veau, 1992). Cancellous (or trabecular) bone forms an interconnecting network of trabeculae within the metaphyses and epiphyses. It has a porosity of greater than 70 % (Le Veau, 1992). Bone strength and stiffness vary inversely with increasing porosity. The mechanical properties of cancellous and cortical bone differ greatly because of their different densities and porosities (Le Veau, 1992). However, many researchers believe that despite morphological similarities between cortical and cancellous bone, they are distinct materials with different mechanical properties, not due to density and porosity

differences alone (Schaffler *et al.*, 1988). The mechanical properties of trabecular bone can vary as much two orders of magnitude depending on its location (Goldstein *et al.*, 1983). This complies with Wolff's law which predicts a response to different loading conditions which exist across the bone (Mow *et al.*, 1991).

1.1.2 Bone Cells

There are three major types of bone cells, osteoblasts, osteocytes and osteoclasts. See Figure 1.3.

Osteoblasts are the bone building cells and produce large quantities of the uncalcified collagen matrix, called osteoid. Osteoblasts are derived from osteoprogenitor cells which are present in the blood vessels of the Haversian vascular system and the periosteum. Osteoprogenitor cells will divide frequently in initial bone production and at fracture sites, but once they have transformed into osteoblasts they rarely divide.

Osteocytes are derived from osteoblasts which become trapped in the matrix and cease to produce osteoid. The osteocytes have a regulatory function and maintain bone tissue. They reside in a space called a lacuna and develop long dendritic arms, called canaliculi, which act as a communication network between adjacent osteocytes and enable the living cells to survive in a heavily mineralised environment. As these cells mature they resorb calcium or phosphate from the surrounding tissues, in response to hormonal signals. This process is known as osteolysis and it maintains the necessary levels of circulating calcium.

Osteoclasts are involved with bone resorption rather than production and are found in hollow depressions in the bone tissue known as Howship's lacunae. The resorptive surface of the cell, which is enfolded in a ruffled border, removes apatite crystals and collagen from the bony tissue.

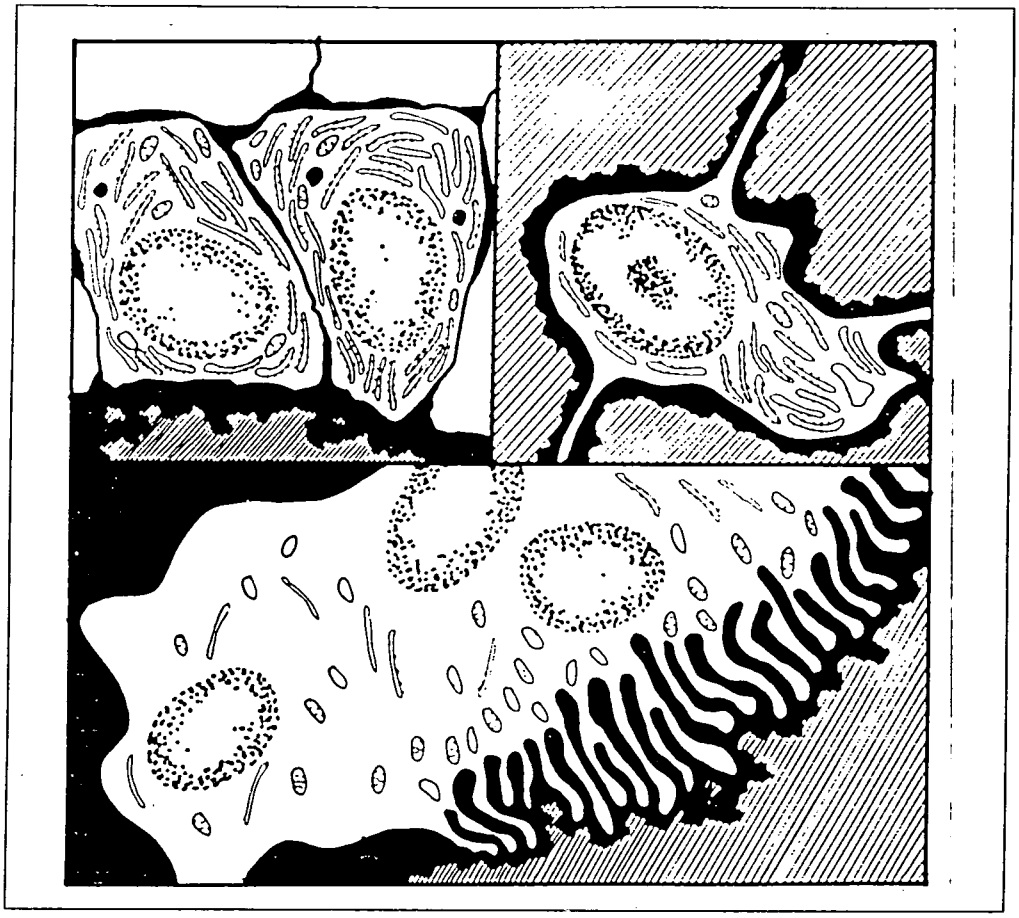

Figure 1.3. Bone cells. The diagonally shaded areas are bone. Osteoblasts, responsible for secreting osteoid, are typically columnar in shape and have many rough endoplasmic reticulum (Top left). Osteocytes are osteoblasts trapped in lacunae in the osteoid. They communicate with other cells through long dendritic processes lying in canaliculi (Top right). Osteoclasts are large cells with many nuclei that are responsible for resorbing bone tissue. Resorption occurs at the ruffled border, to the right, where digestive enzymes are released, creating rounded depressions known as Howship's lacunae (Bottom). Within cells, the stippled structures are nuclei; short ovals are mitochondria; and elongate ovals are either rough endoplasmic reticulum (studded edges) or Golgi apparati (plain edges) (From Shipman *et al.*, 1985).

The components of the cell which carry out specific functions are called organelles. One such organelle is the Golgi apparatus. Its activities include concentrating and packaging proteins and lipids and secreting macromolecules from the bone cell. The mitochondrion, another organelle, stores carbohydrates, releasing energy for various metabolic functions. The endoplasmic reticulum organelle which contains compartments of proteins and other substances, contains the instructions to synthesise these products when required by the body.

1.1.3 Collagen and Calcification

Bone tissue is a composite material. About 90 % is the protein molecule, collagen, which forms flexible, slightly elastic fibres in bone (Le Veau, 1992). It is produced from procollagen which is derived from osteoblasts. The remaining 10 % by weight of solid bone tissue is inorganic bone mineral. The collagen is stiffened by the bone mineral which consists of calcium hydroxyapatite (Cameron *et al.*, 1978). This is an inorganic crystal which impregnates the collagen matrix (Folkens, 1991).

The formation of bone by the calcification of the osteoid is a complex process. This mineralisation is localised to bones despite the presence of collagen in many sites throughout the body. Calcium phosphate is stored in or near mitochondria, in the osteoblasts and provides sufficient minerals for the crystals of hydroxyapatite to form. A substance triggers the growth of the crystals, although the precise trigger mechanism is not yet fully understood (Seligson, 1985). A group of proteins serve to localise the calcification of osteoid.

1.2 Fracture Healing

Fracture healing involves the restoration of normal strength to the bone to prevent fracture reoccurring and to provide sufficient skeletal support. It is quite a unique form of tissue repair, in that bone is regenerated rather than forming a scar (McKibbin, 1978). When fracture occurs the normal skeletal homeostasis is disrupted. The blood supply is damaged (Figure 1.4), stability to the limb is lost and metabolic changes occur. The blood vessels of the Haversian canals, the periosteum and the marrow are normally damaged by the trauma. A state of hypoxia (a deficiency of oxygen) in the tissue exists, the local environment is acidic (Heppenstall, 1980) and the bone edges of the fracture site become necrotic. Blood flows into the fracture site and coagulates to form a hematoma (McKibbin, 1978). The pain which accompanies trauma causes a reflex muscle contraction which aids immobilisation of the fracture.

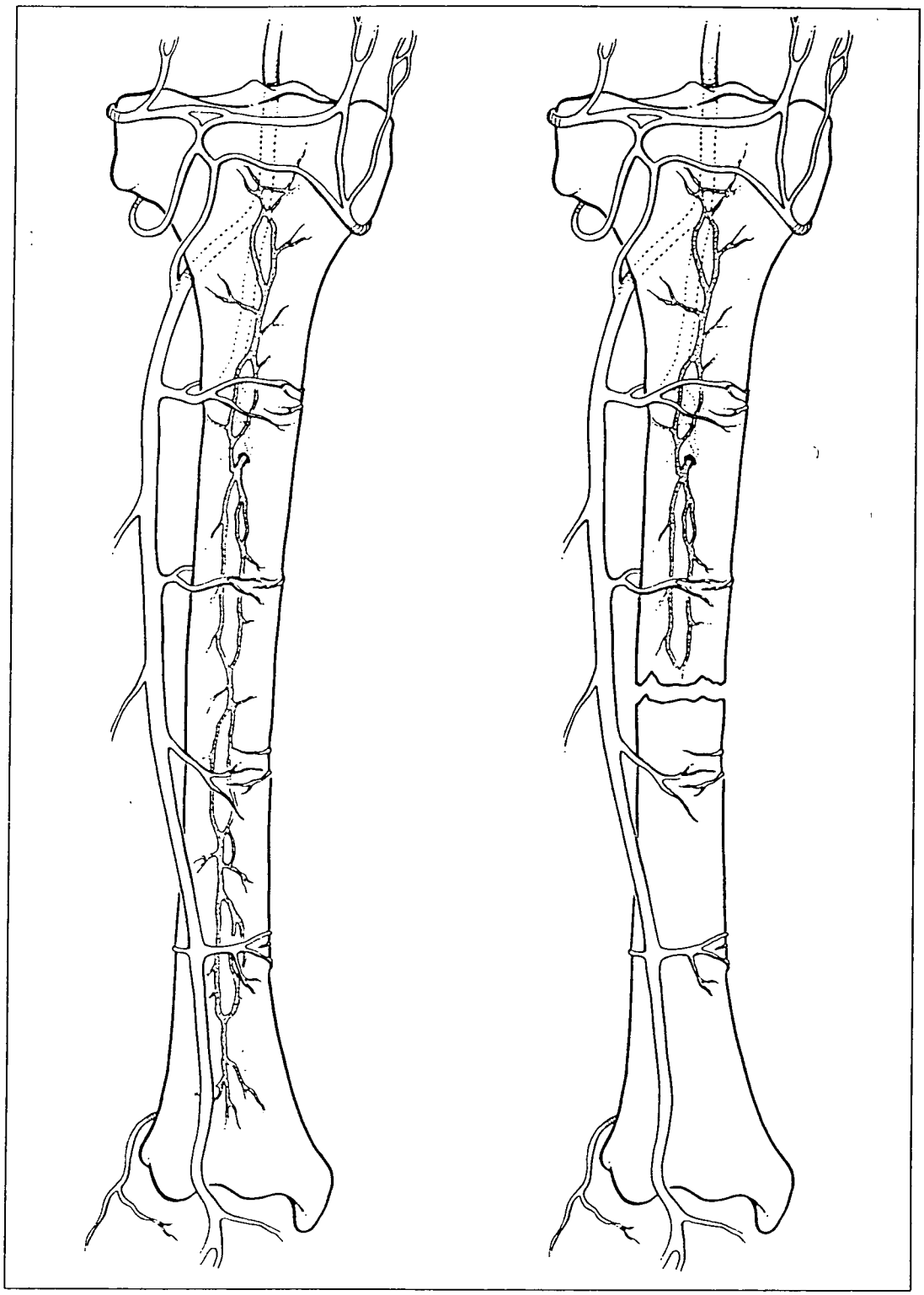

Figure 1.4. Schematic representation of the effect of fracture on the medullary and periosteal blood supply to the tibia. The endosteal blood supply is disrupted across the fracture site and the periosteum torn (From Seligson, 1985).

1.2.1 Inflammatory Phase

The formation of a hematoma is accompanied by an inflammatory response (Rockwood *et al.*, 1984). Vasodilatation occurs with the blood vessels increasing in diameter and an exudate of proteins, plasma and white cells escape into the trauma region. A soft tissue cuff forms around the fracture site which increases both the cross-sectional area and the moment of inertia of the bone, thus greatly increasing the stiffness of the fracture. Prostaglandins are also released which are associated with bone resorption, bone collagen synthesis and general cleanup of the fracture (Pan *et al.*, 1992). The trauma phase lasts about 5 days in adults (Figure 1.5.). It has been postulated that a large oxygen gradient across the fracture site is responsible for triggering the initial healing mechanisms (Heppenstall, 1980).

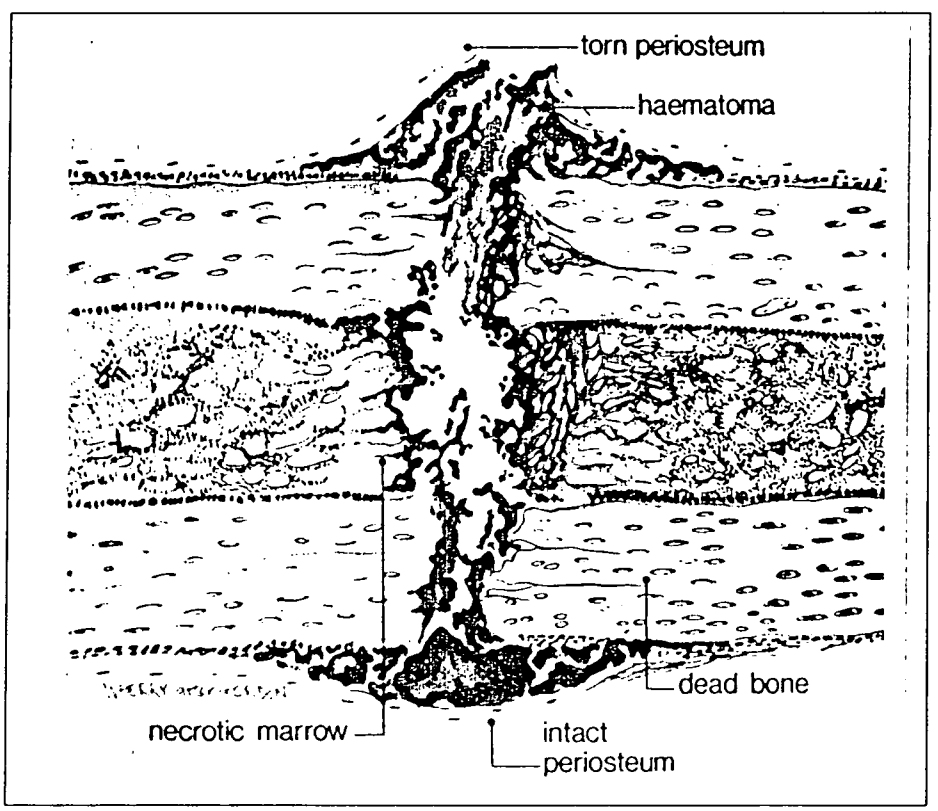

Figure 1.5. During the inflammatory phase of bone healing, hematoma develops around and through broken bone, even when the periosteum remains intact. Hematoma formation is essential for callus formation (From Radin, 1987).

1.2.2 Cartilaginous Phase

This phase is sometimes described as the proliferative or soft callus phase. The fracture hematoma is invaded by blood capillaries and mesenchymal cells (cells concerned with newly developing tissue). The periosteum which surrounds the bone is the site where new active bone cells proliferate during fracture repair (McKibbin, 1978). These cells differentiate into fibroblasts, chondroblasts and osteoblasts depending on the local requirements (Heppenstall, 1980). The production of fibrous tissue, cartilage and osteoid by the mesenchymal cells forms the callus tissue (Figure 1.6.). By approximately the second week after fracture the callus will be fairly solid due to some cartilage calcification and new bone formation. There is a marked increase in the quantity of type I collagen, which indicates the development of osteoblasts and the onset of remodelling of woven bone to cancellous bone (Pan *et al.*, 1992). Medullary callus also develops and the blood supply is slowly restored to the medullary canal.

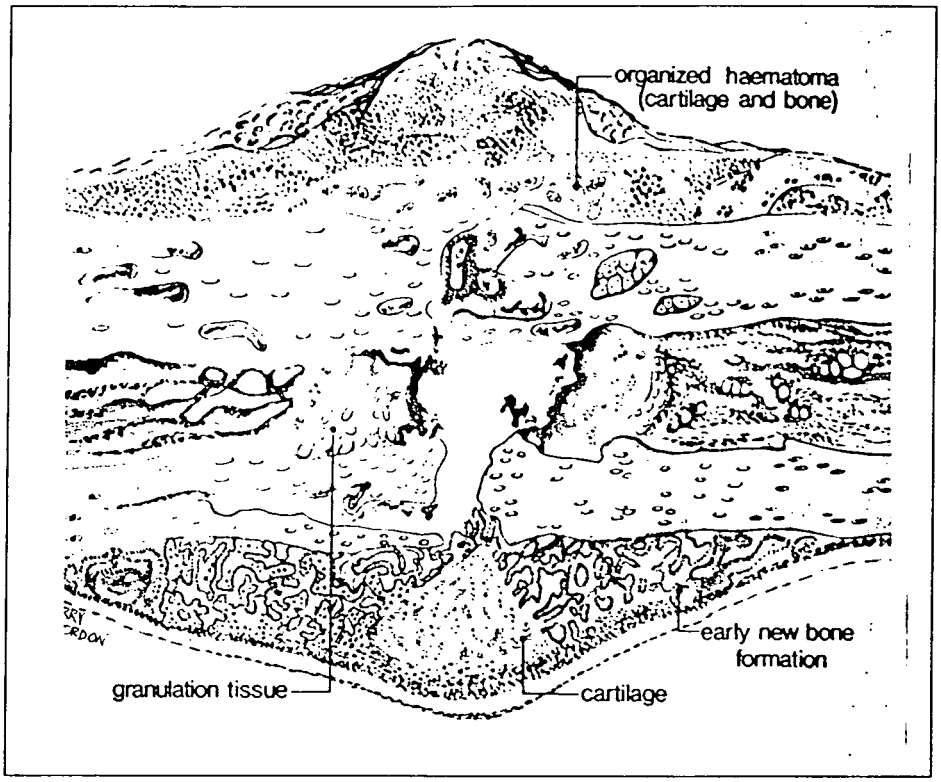

Figure 1.6. In the proliferative phase the hematoma is organised and by the second or third week will be somewhat "bony" due to cartilage calcification and periosteal new-bone formation (From Radin, 1987).

1.2.3 Mineralisation Phase

This stage, sometimes referred to as the hard callus phase or bony phase (Peltonen *et al.*, 1992), commences at 3 to 4 weeks post fracture and continues until new bone unites the bone fragments, at about 3 to 4 months post fracture for long bones in adults. The pH of the matrix reverts to neutral at this phase (Heppenstall, 1980). Depending upon the rigidity of the fracture fixation, direct union may occur (Figure 1.7.). In the case of a mechanically stable fracture, where the rigidity is high and the alignment of the bony ends is good, very little cartilaginous tissue is formed. Instead a thin layer of hard callus bridges the gap. In these conditions healing occurs by direct Haversian remodelling, with the small areas of cartilage quickly resorbed into the surrounding bony trabeculae. At least 17 families of non-collagenous proteins are involved in the mineralisation phase of fracture healing. These non-collagenous

proteins make up about 2 % of the total bone mass. One of these families, proteoglycans, are thought to facilitate the mineralisation of the fracture callus. Also, the enzyme alkaline phosphatase shows a peak activity 14-17 days post-fracture at the trauma site and is associated with the deposition of hydroxyapatite crystals in the osteoid matrix (Pan *et al.*, 1992).

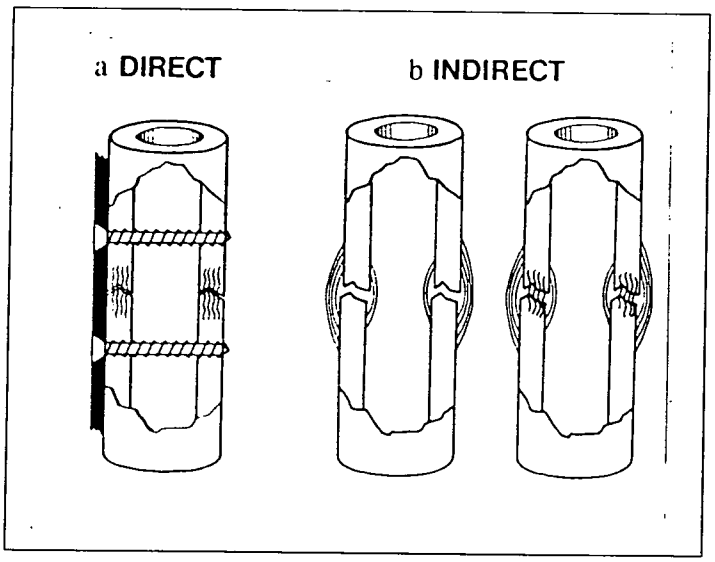

Figure 1.7. The healing process. (a) Rigid fixation may permit direct union, but it inhibits callus. (b) When a fracture heals "naturally", without rigid fixation, callus forms first, then bone grows across the fracture. The process may be less direct but it has distinct advantages (From Apley, 1982).

1.2.4 Remodelling Phase

Remodelling of the bone occurs by cutting cones composed of osteoclasts followed by matrix depositing osteoblasts. Capillaries slowly penetrate the woven bone creating a hole by removing the old bone. The filling cone is tapered and extends a further distance longitudinally than the cutting cone, reflecting the greater time required for filling. The cutting cones can advance at a rate of 50 to 60 microns per 24 hours (Heppenstall, 1980). When these cones have gradually resorbed the woven bone of the callus, they lay down the Haversian bone that was present prior to fracture (Figure

1.8.). Non-collagenous proteins known as osteopontin, osteonectin, vitamin K and vitamin D dependent proteins and growth factors are thought to regulate bone development, however their precise involvement in the remodelling phase of healing is not yet fully understood (Pan *et al.*, 1992).

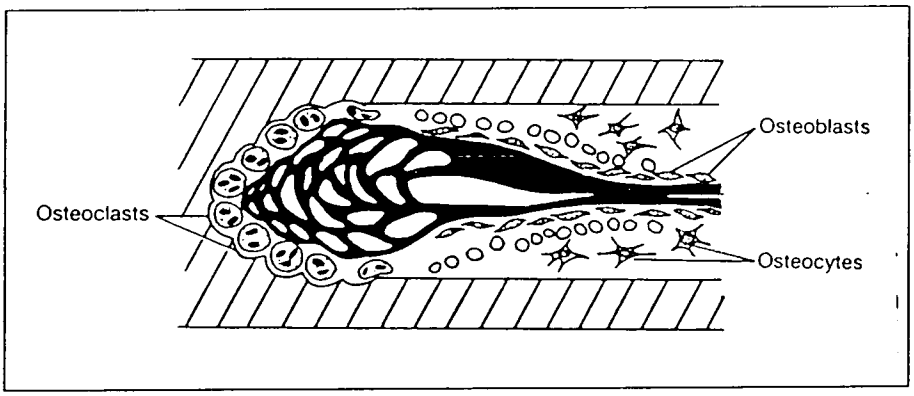

Figure 1.8. This schematic cutting cone is moving right to left through bone. At the tip osteoclasts resorb bone; osteoblasts lay down new bone, are engulfed by the matrix they form, and become osteocytes. New osteoblasts are produced from the capillary walls as the cutting cone moves along (From Radin, 1987).

Cortical bone is much slower to heal than cancellous bone. The marrow around cancellous bone provides a ready source of osteoblasts and there is less bone to resorb during the remodelling phase. Osteoclasts also remodel the cuff of callus to reduce its size. With favourable conditions cancellous bone may be solidly united after just 4 weeks (Radin, 1987). Cortical bone usually requires about 8-12 weeks to heal (Figure 1.9.).

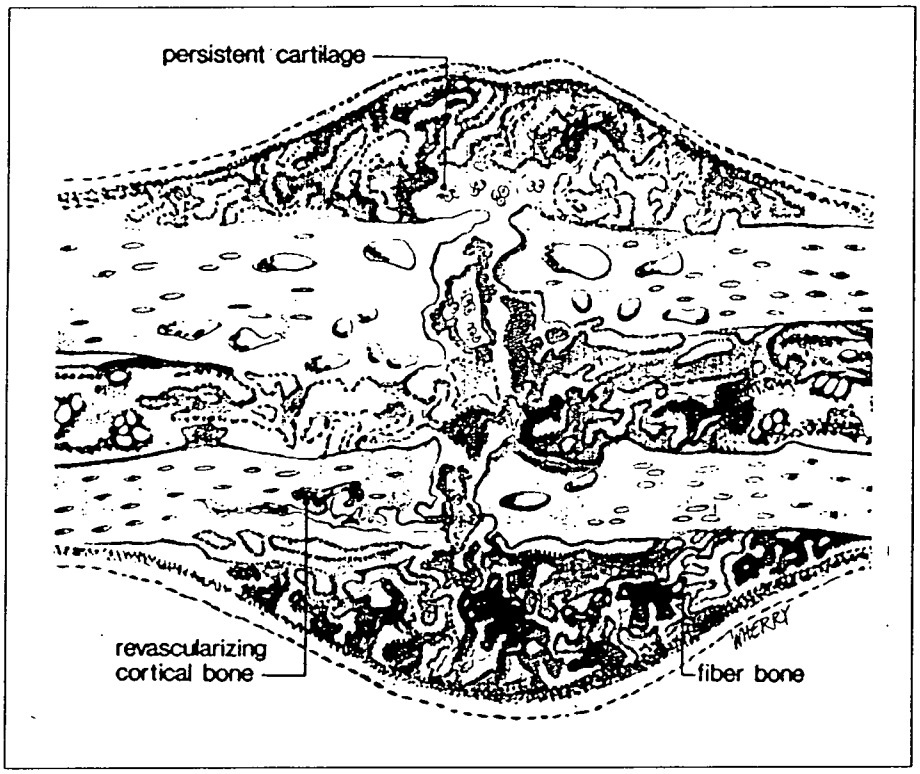

Figure 1.9. During the remodelling phase, the callus is resorbed and new bone is laid by capillary ingrowth and osteoblastic bone formation (From Radin, 1987).

1.2.5 Speed of Healing

Nicoll studied 705 tibial fractures and noted that the factors most conducive to delayed or non-union were initial displacement, comminution, associated soft tissue injury and infection (Nicoll, 1964). However, a basic requirement for good healing is an adequate blood supply for capillary ingrowth and nutrient supply. During the inflammatory phase the fracture should be completely immobilised so that the vascular supply may be reinstated (Rockwood *et al.*, 1984). The rate of fracture healing depends upon the vascularity of the trauma site, the greater the severity of the injury the higher the incidence of delayed or non-union (Ellis, 1958). In addition the two fracture ends must be in relatively close proximity to each other for bridging callus to form.

Bone is a piezoelectric material. At the site of an injury a small direct current arises (Cameron *et al.*, 1978) and it appears that bone formation favours electronegativity (Heppenstall, 1980). Attempts have been made to apply electric currents directly to a human fracture or via the use of non-invasive electromagnets to improve the rate of healing. Some reports believe the results of improved healing times are inconclusive (McKibbin, 1978). However, in a double blind patient trial to study the effect of pulsed electromagnetic fields on 45 tibial fractures with delayed union, it was concluded that significant improvements in the healing of patients occurred with active electromagnetic stimulation (Sharrard, 1990)

The amount of callus which forms indicates the amount of movement present at the fracture site and the healing rate can be increased by allowing small movements of the fracture site to occur. Both Panjabi *et al.*, (1977) and Goodship and Kenwright, (1985) demonstrated that cyclic loading producing a small (≤1 mm) amount of micromovement of a fracture can favour healing.

1.3 Callus Properties

The appearance of fracture callus on a radiograph can offer a subjective impression of fracture healing, but does not impart any information on the strength of union. During each phase of healing the fracture gap contains tissue with mechanical properties which correspond to the degree of movement present in the fracture during that phase. Table 1.1. shows the properties of these tissues, sequenced in the order that they develop during healing, and demonstrates the changing properties required. At the commencement of healing the gap has to be filled with a tissue capable of considerable elongation, so that movement of the fracture does not cause the new tissue to tear. At the end of the fracture healing process a stiff material with a high ultimate tensile stress is required to withstand normal stresses without breaking.

Tissue		Elongation in %	Modulus of elasticity (kp/mm^2)	Ultimate tensile strength (kp/mm^2)
Parenchyma (Granulation tissue)		100	0.005	0.01
Perichondrium (Connective tissue)	1	17	40	1.18
	2	12	1.67	0.2
Tendon	1	9.5	100	6
	2	5	25	1.2
Fibrous cartilage	1	12.8	80	1.9
	2	10	2	0.4
Vertebral cancellous bone	1	2.5	8	0.16
	2	0.58	18	0.12
Compact bone	1	2	1060	13
	2	1.49	1830	14.1

Table 1.1. Mechanical properties of tissues. 1: low strain; 2: high strain. (From Perren *et al.*, 1978)

Following trauma it is probable that sufficient strength exists for normal limb function after a relatively short period of time (approximately 15 to 20 weeks) when stiffness of the fracture is such that the fractured limb is able to withstand normal forces exerted by the muscles and weight bearing. In animal osteotomy experiments this occurs in one third to one half the time for complete remodelling of the fracture site. The return of the ultimate strength of the bone is an indication of the end of healing (Black *et al.*, 1984). However, measuring strength and stiffness of a fracture *in vivo* is not always possible.

Aro *et al.* (1989) attempted to correlate the mineral density in the external fracture callus of the rat with the mechanical properties and morphological characteristics of the callus. The callus reached its maximum diameter two weeks after fracture, after which mineralisation commenced. The formation of callus increases the effective cross-section of bone and consequently offers greater resistance to bending, *i.e.* increased stiffness of the fracture (Perren *et al.*, 1978). Markel *et al.* (1990) investigated the association between the material and structural properties of healing

tibiae in dogs and it was observed that maximum callus diameter was achieved 6 weeks after fracture. Callus hardness was found to increase slowly for the first 3 weeks and then rapidly between 3 and 4 weeks, after which it reached a plateau; calcium content of the callus was exponentially correlated with the callus hardness (Aro *et al.*, 1989). The dependence of the mechanical properties of the callus on its morphological properties have been described by a power-law relationship, similar to the relationship which exists for both compact and cancellous bone (Chakkalakal *et al.*, 1990 and Markel *et al., 1990).* One explanation for the exponential increase in callus stiffness may be due to the maturation of the calcium hydroxyapatite crystal lattice (Markel *et al.*, 1990).

Experiments by Black *et al.* (1984) studying fracture healing in rabbit osteotomies showed that normal stiffness of the limb returned faster than strength. This would indicate that stiffness values would be a preferable indicator for resuming normal functional loading. From the experiments of Markel *et al.* it was noted from radiographs that the periosteal callus was beginning to resorb after 6 weeks, thus implying that its role to anchor the bone ends and bridge the fracture gap had been completed and the osteotomy was sufficiently rigid to allow remodelling to commence (Markel *et al.*, 1990).

The progressive stiffness and strength at the site of a healing fracture is governed by the material properties of the callus and the cross-sectional area of the bone (Aro *et al.*, 1989). However, when very rigid fixation is applied there is little or no external callus formation to indicate the extent of healing and in addition direct measurement of fracture stiffness may be compromised (Perren *et al.*, 1978). The mechanical properties of the callus are related to its bone mineral density (Currey, 1969), so in situations where fracture stiffness measurement may be difficult and unreliable, the non-invasive evaluation of bone mineral density across a fracture site may be a useful

method of assessing fracture healing (Markel *et al.*, 1990 and Chakkalakal *et al.*, 1990).

1.4 Post-trauma Osteoporosis

Even before the advent of radiographs, local changes in bone following trauma were observed by Von Volkmann in 1862 (Nilsson, 1966). During the 1950s it was observed in many rat experiments that at the fracture site there was a rapid increase in bone mineral content following trauma. In the rest of the injured limb a marked decrease in bone mineral density was observed when compared to the contra-lateral, which lasted longer than the physiological time to healing (Ulivieri *et al.*, 1990). It appeared that the loss of bone from an injured limb was due to an increased rate of bone resorption (Wand et al, 1992) and large resorption cavities were seen in the cortical bone from increased osteoclast activity (Young *et al.*, 1983).

Nilsson (1966) studied the loss of bone mineral using a single photon source, in the distal end of the femur following trauma of the tibial shaft. The result was that the mineral content on the fractured side reduced to a value approximately 25 % lower than on the non-fractured side. Ulivieri *et al.* (1990) studied bone mineral loss using dual photon absorptiometry in the tibia after a tibial shaft fracture in 7 patients. Bone mineral density decreased for the duration of the study of 120 days, to approximately half of the pre-fracture level. Also, studies by Andersson *et al.* (1979) on the distal tibia of 27 patients with tibial shaft fractures showed that bone mineral decreased rapidly after fracture for about 5 months to approximately 45 % of the initial bone mineral value. Towards the end of the first year there was a slow restoration of bone mineral so that only 25 % was missing.

Nilsson (1966) also found that the loss of bone mineral was more pronounced in severe fractures and with long periods of convalescence. Loss of bone mineral has been

shown to exhibit no correlation with the method of treatment; fractures treated with internal fixation lost as much bone as those treated with plaster casts (Sarangi *et al.*, 1993). The difference between limbs took approximately 6 to 7 years in males to disappear, but in females the post-traumatic osteoporosis remained for the duration of the study, at least 15 years (Nilsson, 1966). Post-traumatic osteoporosis could therefore lead to permanent weakness of the bone and a predisposition to refracture (Wand *et al.*, 1992).

It has been shown experimentally that physical activity is an important determinant of osteoblast activity (Wand *et al.*, 1992). As a result it is considered that reduced functional loading of a limb is the main cause of post- traumatic osteoporosis (Le Veau, 1992 and Whalen *et al.*, 1988). However, the increased bone resorption in response to fracture is also likely to be a contributory factor (Sarangi *et al.*, 1993). Disuse osteoporosis was studied in monkey tibias by Young *et al.* (1983). After 6 months of restraint bone mineral had decreased by between 23 % to 31 % of original levels, with a corresponding decreases in bone stiffness. It took over 8 months of recovery for the normal bending properties of the limb to be restored, but the bone mineral content did not always return to previous levels (Young *et al.*, 1983).

1.5 Fracture Treatment and Technique

Tibial shaft fractures can be caused by direct violent impact such as motorcycle and car accidents or indirect injuries, for example from sports accidents and falls (Rockwood *et al.*, 1984). High energy impact usually results in greater soft tissue damage, skin loss, bone displacement and comminution. The fracture is often transverse, whereas a low energy impact usually results in an oblique or spiral fracture. Surgeons often use a system to classify the severity of the injury in order to decide on a prognosis. There are many such systems including those of Weissman, Nicoll, Gustilo and Ellis (Rockwood, 1984). The AO (Arbeitsgemeinschaft fur Osteosynthesefragen) fracture

classification of long bones is also often used to describe the complexity, fragmentation and location of the fracture using a code of letters and numbers (Müller *et al.*, 1991). The accompanying skin, muscle, tendon and neurovascular injuries can be graded in a similar manner.

Following a trauma of the lower limb, fixation is utilised to maintain alignment and stability during union of the bone. The different fixation methods available can provide various combinations of stiffness and stability, biological invasion and flexibility of use. The particular method chosen will depend on the extent of damage to the soft tissue and bone.

1.5.1 Bracing and Casts

For a simple fracture, the fracture is reduced and a plaster cast applied from the knee to the ankle. A plaster cast offers good control of angulation but poor control of rotation and length (Latta *et al.*, 1991). Braces are easily adjustable to compensate for the changing leg volume so that soft tissue compression and stability can be maintained. However, their use is limited to fractures with minimal initial shortening and soft tissue damage so that the limb is relatively stable when commencing treatment. The patient is encouraged to start weight bearing at between 10 to 16 days post-fracture as this is reported to reduce muscle atrophy and tissue oedema and shorten the time to successful rehabilitation (Rockwood *et al.*, 1984).

1.5.2 Intramedullary Nailing

Internal fixation developed in the late 19th century following the discovery of anaesthesia and the advance of diagnostic radiology, although early complications occurred due to fatigue failure and material corrosion (Gautier *et al.*, 1992). Internal fixation can be subdivided into intramedullary fixation (via intramedullary nailing) and

extra-medullary fixation (via plates and screws (Section 1.5.3)). Intramedullary fixation is useful for short oblique fractures where there has been extensive angulation or displacement, but is often contra-indicated for use in comminuted fractures (Rockwood *et al.*, 1984). An intramedullary nail takes most of the bending, torsion and compression loads applied to a healing fracture and as a result minimal interfragmentary movement occurs and direct healing of the cortical bone can occur by remodelling. However, if a relatively flexible nail is utilised some secondary healing may occur with the presence of external callus. Intramedullary nailing allows full joint motion and good soft tissue repair. The main disadvantage of this technique is that it is surgically traumatic and leads to a high incidence of infections, non-union and refracture (Gautier *et al.*, 1992). Intramedullary nails which require reaming of the bone disrupt up to 70 % of the cortical blood supply (Whittle *et al.*, 1992). There is also a risk of mechanical failure of either the nail or the fixation screws due to the high loading they sustain (Latta *et al.*, 1991).

1.5.3 Plating

Segmental fractures and intra-articular fractures involving the tibial shaft and knee or ankle joint are best handled with plating (Rockwood *et al.*, 1984). The plate is not as capable as the intramedullary nail at resisting high bending moments and rotation, but does provide very rigid fixation (Gautier *et al.*, 1992). The strength and rigidity obtained with a plate is adequate for immediate early function of the limb, this being only limited by the pain of injury and surgical insult. Healing occurs by primary bone healing with minimal callus formation (Heppenstall, 1980). The major problem of plate fixation is devitalisation of adjacent tissue, subsequent skin breakdown and wound sepsis (Rockwood *et al.*, 1984). With initial plate application there is an immediate alteration of stresses in the bone from the normal physiological stresses to which the bone is accustomed. This may lead to stress fractures at the junction of the plate with the bone. Stress protection under the plate causes osteopenia temporarily,

compromising overall bone strength for at least 6 months post fracture (Latta *et al.*, 1991). When the plate is removed refracture of the tibia may occur due to the disuse osteoporosis (Rockwood *et al.*, 1984). Recent efforts to improve plate fixation techniques include less rigid plates, biodegradable materials, early removal and improvements in plate bone interface. A wave plate was an early attempt to reduce the plate interference with the cortical blood supply and more recently a limited contact dynamic compression plate (LC-DCP) has been developed to improve the periosteal blood supply (Gautier *et al.*, 1992).

1.5.4 External Fixation

The main indication for use of external fixation is severe soft tissue injury. Stabilisation of fractures enhances the healing of adjacent soft tissue and in open fractures reduces the infection rate. It relieves pain and allows mobilisation of muscles, joints and the rest of the patient (Kenwright, 1992). External fixation reduces the need to dissect soft tissue adjacent to the fracture site and may also be applied rapidly. An external fixator can be adjusted to satisfy a particular treatment regime, for example allowing very rigid fixation or to give flexible fixation to allow micromovement. The normal cyclical mechanical loading and strain in a tibia is disrupted if a very rigid fixator is applied, by reintroducing the stimulus of micromovement, for example by using a flexible fixator, improved osteogenesis at the fracture site may be observed (Goodship *et al.*, 1985, Egger *et al.*, 1993). Circular frames offer even greater versatility of treatment. They can resist rotary and angulatory deformation yet allow axial deflection which theoretically improves fracture healing. However, they are difficult to apply and care is needed not to damage muscles, tendons or the neurovascular system (Rockwood *et al.*, 1984). External fixators are liable to pin-tract infection which can lead to loosening and decrease stability (Latta *et al.*, 1991).

1.6 Fracture Healing Measurement

The evaluation of fracture healing often depends on a clinician's assessment of stability, radiographs, time elapsed since fracture and the patient's judgement of pain (Heppenstall, 1980). Manual methods of assessing stability are difficult, especially when a method of fixation is present. Similarly radiographic evidence is open to interpretation and regions of interest may be obliterated if metalwork is present in the image. Time since the fracture is not a reliable method of predicting healing since this varies depending on each individual case. Assessment of pain is very subjective and is also not a good indication of union.

A reliable, non-invasive and accurate method of evaluating the union of fractures would be a useful tool in avoiding unnecessarily long periods of immobilisation and treatment. Also if impending delayed or non-union could be detected, surgical intervention could occur at an earlier stage and improve patient rehabilitation time (Lewallen *et al.*, 1988). Many different techniques and approaches have been employed to try and assess fracture healing with varying degrees of success. These non-invasive methods of assessing bone status can be split into two groups, radiologic and non-radiologic (Hangartner, 1986). For example one method of non-radiologic assessment is to measure fracture stiffness directly. This indicates when sufficient stability of a limb has been obtained to enable functional loading to take place without external support (Richardson *et al.*, 1992). It has also been shown that stiffness is related to the mineralisation of the fracture gap and *in vitro* studies have demonstrated that bone mineral density accounts for 80 % to 90 % of the measured variation of bone strength (Mazess, 1990). Hence, a non-invasive technique for radiologically measuring the mineral density may give a good indication of fracture healing (Chakkalakal, 1990). The earliest attempts to measure bone mineral were of teeth in the 1930s (Goodwin, 1987). Some of the techniques for assessing fracture healing are described below.

1.6.1 Ultrasound

The term ultrasound refers to sound waves over 20 kHz, which are not audible to the human ear. There are two parameters which can be measured using ultrasound; the velocity and the attenuation of an ultrasound wave.

Ultrasound velocity is determined by the wave path divided by the transit time, hence for a known thickness of bone and a measurement of the time for an ultrasound wave to transverse through it, the speed of sound (SOS) through the bone may be calculated (Langton, 1992). It has been reported that there is a significant decrease in ultrasound velocity in cases of non-union (Heppenstall, 1980). Gill *et al.* (1992) observed an immediate fall in ultrasound velocity after a fracture of a long bone, which continued until the callus become radiologically visible, after which time the ultrasound velocity began to gradually increase to the pre-fracture level. The velocity measurements in demineralised bone were significantly slower than through mineralised bone. However, the SOS through intact bone is the same as that through bone which has been transversely sectioned but has its ends closely approximated. If soft tissue is present between the bone ends, the SOS decreases according to the thickness of soft tissue present.

To measure the attenuation of ultrasound through bone the reduction in ultrasound signal amplitude resulting from the propagation through bone is measured. Broadband Ultrasonic Attenuation (BUA) describes the increase in ultrasound attenuation over a particular frequency range, normally 0.2 MHz to 0.6 MHz (Langton, 1992). However, the use of BUA raises conflicting views. There are its advocates who believe the attenuation is related to both the bone mineral content in the path of the beam and also its structure (Tothill, 1989), and those who believe it gives no indication of bone integrity (Mazess, 1990). Both ultrasound techniques are still being evaluated and

have the potential to offer a quick and non-ionising radiation method of monitoring bone (Alhava, 1991).

1.6.2 Stress Wave Propagation

In this technique a small dynamic load is applied to a bony prominence on the proximal tibia to generate a stress wave. An accelerometer is applied to the distal tibia to measure the transmitted wave. This approach would not work if internal or external fixation were present. Changes in the characteristics of a propagating flexural wave occur when a discontinuity such as fracture is introduced into a long bone. This method has unsatisfactory reproducibility due to the boundary conditions at the loading and recording ends of the limb (Heppenstall, 1980). One method employed to overcome this was the application of direct coupling to the bone, thus eliminating the effects of the surrounding soft tissue (Sonstegard and Matthews, 1976). Hypodermic needles were used to provide direct attachment to bone at excitation and sensing locations. An input signal was provided by tapping the excitation needle and unidirectional piezoelectric accelerometers were attached in a vertical orientation at the fracture site. Propagation velocity, amplitude and slope ratios of the incoming and transmitted waves were used to characterise fracture healing (Heppenstall, 1980). Limited clinical trials by Sonstegard and Matthews indicated that this approach had potential for diagnosis of fracture healing. However, the insertion of needles directly into the bone limit the application of this method.

1.6.3 Resonant Vibration

Steady state resonant vibration was studied as a non-invasive measure of bone integrity by Markey and Jurist (1974). The main problem encountered, was that this index depends on the ratio of stiffness to mass. A bone with a reduced load carrying capacity may have a reduced stiffness and also a reduced mass, so may display normal resonant frequency characteristics (Heppenstall, 1980). The resonant frequency of a long bone is related to its flexural rigidity and the speed of sound in bone tissue. It is believed that with improved healing, both the tibial resonant frequency and the amplitude of the resonant peak would increase. Markey and Jurist drew a normal healing curve by plotting the squares of the ratios of the resonant frequency of fractured tibiae to their controls as a function of time. This technique may have useful applications as a predictive tool for assessing healing rates, but repeatability and soft tissue effects still leave doubt as to the accuracy of this method (Heppenstall, 1980).

1.6.4 Fracture Stiffness Measurement

Judging the timing of removal of a fixator may be problematic. If it is removed prematurely there is a risk of refracture or subsequent angulation of the limb. When a fracture is sufficiently healed to enable functional loading to occur, the external fixator can be removed and the stiffness of the limb alone is sufficient for healing to continue (usually through remodelling of the fracture callus) and for normal bone strength to return. Fracture stiffness can be determined from the displacement of the fracture resulting from a known load (Richardson *et al.*, 1992). When an external fixator is utilised and its stiffness known, strain gauges or transducers may be attached to obtain absolute measurements of fracture stiffness. Jernberger (1970) designed an external fixator which was fitted to both the fractured and unfractured limb under local anaesthetic, to measure the deflection from an applied load. The deflection of the

unfractured limb was subtracted from the defection of fractured limb to give a measure of the deflection of the actual fracture site. Hence the flexural rigidity of the fracture callus could be obtained to indicate the level of healing (Jernberger, 1970). Richardson *et al.* (1992) attempted to establish a threshold value of fracture stiffness at which independent weight bearing could be permitted. They studied 120 patients with tibial fractures, stabilised with external fixators and measured the stiffness at the time of removal of the fixator. A strain gauge transducer was fitted to the fixator column and the patient's leg loaded in anterior / posterior bending. It was found that no refractures or angulation occurred above a stiffness of 15 Nm degree^{-1} in the sagital plane. Jernberger gave a mean value of stiffness for an intact male tibia to be 65 Nm degree^{-1}, which would indicate functional loading could occur when rigidity of the fractured limb was 20 % to 25 % the value of the contra-lateral healthy limb. Black *et al.* (1984) tested bone rigidity by applying strain gauges to the connecting rod of the external fixator. They found that as callus increased, the rigidity approached 50 % of the healthy contra-lateral limb and no deflection occurred. At this point they considered the fracture sufficiently strong to remove the fixation device and for the patient to commence weight bearing. There are many sources of inaccuracy associated with fracture stiffness methods. Soft tissues and the stability of the fixator and pins will effect the results. The calculation of rigidity depends on the assumptions made about the stiffness of the fixator system and these will effect the accuracy of the calculation.

1.6.5 Scintigraphy

At the site of a fracture there is an increased uptake of a radionuclide bone scanning agent, than in normal bone. The first report of using a radionuclide to evaluate bone viability following fracture was reported by Tucker (1950). Several different agents have been used to investigate fracture healing since that date including Phosphorus, Strontium, Fluorine and compounds of Technetium (Smith *et al.*, 1987). Technetium-methelyne diphosphonate (MDP) has been shown to be the most promising

(Auchincloss *et al.*, 1982, Smith *et al.*, 1987). Scintigraphy has been evaluated to assess whether a single scintigraphic investigation would give a satisfactory prediction of the final outcome of a fracture. Smith *et al.* (1987) suggested the hypothesis that disrupted blood flow may be related to non-union and that a scintigraphic scan taken 10 to 14 days post-fracture, when the blood supply is at its maximum and about 5 minutes after the agent has been injected when its uptake is predominantly related to blood flow, would be a good predictive tool for non-union. Control regions in the fractured limb were used to compare radionuclide uptake. The ratio obtained between the uptake at the fracture site and at normal bone adjacent to it 2 weeks post-fracture, could predict non-union occurring six months later in a patient with reasonable sensitivity and specificity. Auchincloss *et al.* (1982) carried out scintigraphy 6 weeks post-fracture and concluded that it gave a good indication of the time to fracture healing but that it could not predict non-union. Scintigraphy has the disadvantage of injecting the patient with a radioactive source and there still remains a lot of controversy regarding the accuracy and sensitivity of results obtained.

1.6.6 Computed Tomography

Radiographic assessment of fracture healing alone is difficult. It relies on viewing loss of the fracture line, visible callus and bony bridging. In computed tomography (CT) a thin transverse slice through a body is imaged and can be quantified to give a distribution of attenuation coefficients and a measure of bone mineral density (Tothill, 1989). Experiments were carried out to evaluate the contribution computed tomography could make in assessing fracture healing in association with plain radiographs (Braunstein *et al.*, 1986). 15 Sheep had mid shaft osteotomies and intramedullary nails to stabilise their segmental fractures. The animals were sacrificed at 3, 6, 12, 24 and 36 weeks post-fracture. Plain radiographs were taken of the femoral specimens and computed tomography scans were then taken with the intramedullary nail removed. At 3 weeks the radiographs clearly showed bridging

callus and the formation of trabecular arching, which appeared earlier than on the computed tomography scans. At 12 weeks the fracture lines were quite indistinct when viewed on the radiographs, due to abundant callus formation. However the computed tomography scans gave a much clearer impression of the extent of remodelling and the progression towards healing. The study of Braunstein *et al.* (1986) indicated that plain radiography and computed tomography appear to complement each other in the evaluation of fracture healing. Plain radiographs have good spatial resolution and allow early detection of callus formation. However they do have poor sensitivity, for example in the presence of profuse callus, while computed tomography can clearly show the extent of primary healing, an x-ray cannot. CT scanners are also prohibitively expensive for use in bone mineral density measurements (Tothill, 1989). Quantitative computed tomography (QCT) has been used to investigate the relationship between bone mineral density and fracture characteristics in the vertebra by Dickie *et al.* (1988). It was concluded that only in a limited number of cases was it possible to link the bone strength of the vertebra to its density measured by computed tomography. CT has limited accuracy due to bone marrow fat deposition affecting results (Sartoris *et al.*, 1990). However, the major disadvantage of computed tomography is that it cannot be used with metallic internal fixation, so its application is restricted. QCT may be unreliable, is generally not widely available for densitometry, has exposure times 10 to 100 longer than for photon absorptiometry (Eyres *et al.*, 1993 (a) and Mazess, 1990) and the radiation dosage (100 to 1000 mrem) to the patient is much higher than for an equivalent DXA scan (1 to 3 mrem) (Johnston *et al.*, 1991).

1.6.7 Quantitative Radiographic Densitometry

As early as 1901 a copper wedge was used to calibrate an x-ray in an attempt to evaluate the density of bone from the grey levels of the image (Hangartner, 1986). Photometric methods were developed by Mack *et al.* (1949) to measure bone density by gauging the intensity of light transmitted through a plain radiograph (Goodwin,

1987). Tiedeman *et al.* (1990) carried out studies using dogs with standard tibial osteotomies. Optical densitometry of plain radiographs was compared with direct measurements of fracture rigidity for each dog. The radiographic density of the osteotomised tibiae was exponentially related to its bending rigidity, with a high correlation coefficient. Tiedeman *et al.* (1990) concluded that this quantitative method of assessing radiographs provides a more reliable and accurate method of assessing fracture healing than the subjective interpretation of x-rays clinicians currently use. This method may also be useful in predicting the rigidity of a fractured limb in a non-invasive manner when rigidity cannot be directly measured. It is also a relatively cheap technique (Alhava, 1991). However the method is limited by the quality of the radiograph which tends to be relatively insensitive and cannot detect new bone formation until a considerable amount has been laid down (Eyres *et al.*, 1993 (b)). Problems also exist with variations in tube voltage, x-ray intensity, exposure, film characteristics, film processing and attenuation from uneven thicknesses of soft tissue. Most of these can be minimised with the use of a calibration wedge placed next to the limb during radiography (Tothill, 1989).

1.6.8 Photon Absorptiometry

Single photon absorptiometry (SPA) was first introduced in by Sorenson and Cameron in 1963 (Tothill 1989). Compared to radiographic densitometry the use of single photon absorptiometry has many advantages. For example the use of a scintillation detector eliminates problems incurred with non-uniform film sensitivity. Measurements of callus density can also be used to predict fracture stiffness and thus the time to clinical union (Richardson *et al.*, 1992). Aro *et al.* (1988) studied the use of single photon absorptiometry in monitoring fracture mineralisation in rat tibiae. Standard closed fractures were created and stabilised with intramedullary nails. Single photon absorptiometry scans were carried out after the animals had been sacrificed to calculate the mineral distribution. The bone mineral content along the length of the

tibiae was compared to the hardness and calcium content along its length and these three properties all exhibited similar time related changes. In particular the mineral content of the callus correlated closely with its Brinell hardness value. High resolution SPA appeared therefore to provide a promising non-invasive method of quantifying the distribution of bone mineral in and around the fracture site. This method also showed potential for detecting union of cortical bone even in the presence of fracture callus (Aro *et al.*, 1988). SPA in theory is limited to two components, *i.e.* bone and homogeneous soft tissue. The soft tissue must be of constant thickness, which is achieved by surrounding the limb with a known thickness of soft tissue equivalent material; normally the limb is immersed in a water bath (Genant *et al.*, 1991). Often an irregular amount of fat is present which causes inaccurate results (Pye, 1991). Dual photon absorptiometry (DPA), by using two different photon energies can calculate bone mineral for varying soft tissue thicknesses and does not require the utilisation of a water bath. Both SPA and DPA machines require regular replacements of their expensive radioactive sources, which is recommended every 6 to 12 months (Sartoris *et al.*, 1990)

1.6.9 Dual Energy X-ray Absorptiometry

During the 1960s and the 1970s the first approach of using a dual energy x-ray source for bone densitometry was pioneered in Scandinavia (Sartoris *et al.*, 1990). Dual energy x-ray absorptiometry has many advantages over DPA including higher spatial resolution, improved precision and shorter scan times (Mazess, 1990). Dual energy x-ray absorptiometry (DXA) has been used to monitor new bone formation during leg lengthening by Eyres *et al.* (1993 (a)) in which six patients undergoing leg lengthening of the tibia or femur were scanned using DXA preoperatively and at 2 to 4 week intervals subsequently. Scans were performed on both the operated and non-operated limbs. Bone density changes could be monitored longitudinally or transversely across the bone. It was found that the rate of mineralisation could be determined for newly

generated bone. DXA would therefore appear to be a useful tool for leg lengthening procedures where too fast a distraction rate may cause mineralisation defects or too slow a distraction rate may lead to premature fusion. In most of the patients of Eyres' study the fixator was removed and further stress protection afforded by the fixator eliminated, when the bone density had reached about 75 % of control values (these being either those of the contra-lateral healthy limb or pre-operative levels). There may therefore be an optimum level of bone recovery when the fixator could be removed. The disadvantage of DXA is that it is a two dimensional method so defects in the bone may not be detected unless they lie in the correct plane.

1.7 Dual Energy X-ray Absorptiometry

Dual energy x-ray absorptiometry is also known as dual-energy radiography, dual-energy radiographic absorptiometry, quantitative digital radiography and dual x-ray absorptiometry (Kellie, 1992). These expressions are often abbreviated to acronyms such as DEXA, DER, DRA, QDR and DPX (Genant *et al.*, 1992). To avoid confusion the abbreviation adopted for dual energy x-ray absorptiometry will be DXA. This is the term that has been accepted by the International Standards Committee, which discusses calibration standards, terminology and measurement units (Genant *et al.*, 1992).

Dual energy x-ray absorptiometry (DXA) provides a quick, non-invasive and quantitative method of measuring bone density. It allows very site specific studies to be made of bone mineral density. Potentially DXA could quantify callus density and determine both normal and abnormal changes in bone mineral density (BMD) in and around the fracture site. It may be particularly useful since early mineralisation may be seen more readily using DXA than by viewing conventional radiographs. It has been established that a relationship exists between the mechanical properties of bone such as its stiffness and the bone mineral density (Currey, 1969). Therefore the non-invasive

evaluation of bone mineral could be a useful tool for monitoring fracture healing (Markel *et al.*, 1990 and Chakkalakal *et al.*, 1990). The deficiency of, or late onset of mineralisation of the callus may also provide an early indication of a fracture progressing towards delayed or non-union. In addition, different patterns of healing by different treatment modalities may be also be observed.

Conventional dual energy bone densitometers for measuring bone composition used a radionuclide source to generate the photon beam. Dual energy x-ray absorptiometry (DXA) is the successor of dual photon absorptiometry (DPA), in which the radionuclide source is replaced with an x-ray tube. It first became commercially available in 1987 (Kellie, 1992). The advantages of DXA are that due to its higher photon intensity than DPA, it has faster scan times, improved precision, no radionuclide to decay over time, lower patient dose and better image resolution (Lunar Corp., 1988). The measurements are normally expressed as BMC (bone mineral content) measured in grams and as BMD (bone mineral density), which is an area density in units of g cm^{-2}. BMD describes the bone mass per unit of projected volume or the average mass per pixel (Mazess *et al.*, 1990).

1.7.1 Theory

Using two different photon energies allows bone mineral measurements of parts of the body which do not have soft tissue and bone of constant thicknesses. The bone mineral content of a region of interest can be calculated by solving two simultaneous equations obtained at each energy level. In discussing the theory behind DXA, the following designations and units will be used.

I = Intensity of obstructed radiation, photons/sec.

I_0 = Intensity of unobstructed radiation, photons/sec.

b = index for bone mineral.

s = index for soft tissue.

a = index for aluminium.

p = index for perspex.

μ = mass attenuation coefficient, cm^2g^{-1}.

m = amount of absorber in the path of the beam, g cm^{-2}.

To analyse a given number of substances, attenuation measurements are required for the same number of discreet photon energies. Assuming the radiation quality and geometry are such that the photon energies obey Lambert's Law (Equation 1.1) then it is assumed that the photon energies are exponentially attenuated on passing through a patient (Storm *et al.*, 1958). The simultaneous equations obtained from Lambert's law can be solved only if there are as many independent equations as unknowns. The intensity of a photon beam after passing through m kg m^{-2} of matter is given by Equation 1.1.

Lambert's Law. $I = I_0 e^{-\mu m}$ Equation 1.1.

For a given material the mass attenuation coefficient, μ (in cm^2 $g^{-1)}$ is proportional to the photoelectric cross-section, σ_{TOT} (in cm^2 $atom^{-1}$) (Equation 1.2.). Where N_a is Avogadro's number, in atom mol^{-1} and M is the atomic weight of the absorber material, in g mol^{-1} (Hubbell, 1982).

$$\mu = \sigma_{TOT} \frac{N_a}{M}$$ Equation 1.2.

The photoelectric cross-section varies approximately as the fourth power of the atomic number of the material and inversely as the third power to the photon energy (Webb, 1990).

Two photon energies would therefore allow discrimination of two substances in a given system. If only two substances are present, the technique is capable of high accuracy. In the case where more than two substances are present, the accuracy with which the two substances of interest can be measured depends on the number of additional substances, their attenuation characteristics, and the fraction of the total which they represent. It is not possible to use a third photon energy to compensate for a third tissue component, for example fat, since the attenuation of a wide range of tissues and energies can be expressed in terms of only two components, to within 0.5 %. Therefore a three component system could not be solved (Tothill, 1989). Clinically, a two component system can be defined as consisting of bone mineral and soft tissue. Equation 1.3. and Equation 1.4. describe the attenuation of two photon energies, passing through a bone tissue mass.

Low energy. $I = I_0 e^{-\mu_s m_s - \mu_b m_b}$ Equation 1.3.

High energy. $I' = I'_0 e^{-\mu'_s m_s - \mu'_b m_b}$ Equation 1.4.

The suffixes s and b refer to soft tissue and bone respectively. The photon intensity after passing through the system can be measured directly and the attenuation coefficients can be determined by various methods, the simplest being the use of published values. Solving Equations 1.3 and 1.4, with reference to m_b gives Equation 1.5.

$$m_b = \frac{\mu'_s \ln \frac{I_0}{I} - \mu_s \ln \frac{I'_0}{I'}}{\mu'_s \mu_b - \mu_s \mu'_b} \qquad \text{Equation 1.5.}$$

The Equation 1.5. can be simplified with the following designations.

$$D_{sb} = \mu'_s \mu_b - \mu_s \mu'_b$$

$$N = \mu'_s \ln \frac{I_0}{I} - \mu_s \ln \frac{I'_0}{I'}$$

A numerical value for N can be calculated from the known values of μ_s and μ'_s and the count measurements of I_0, I, I'_0 and I'. N is a constant for a given machine and material. D_{sb} can be considered a constant for a certain measurement geometry, which depends on the ratio of bone mineral to soft tissue (Roos, 1984). The relationship between linear attenuation coefficient and photon energy is shown in Figure 1.10. A typical value of the ratio between soft tissue mass attenuation coefficients at high and low photon energies, μ_s / μ'_s, is about 1.34. Higher values are obtained for lean patients (1.37) and lower values obtained for obese patients (1.31) (Lunar Corp., 1991). The attenuation coefficient depends on both the photon energy and the effective atomic number of the medium (Hubbell, 1969).

Therefore simplification of Equation 1.5. gives the following expression for m_b.

$$m_b = \frac{N}{D_{sb}} \qquad \text{Equation 1.6.}$$

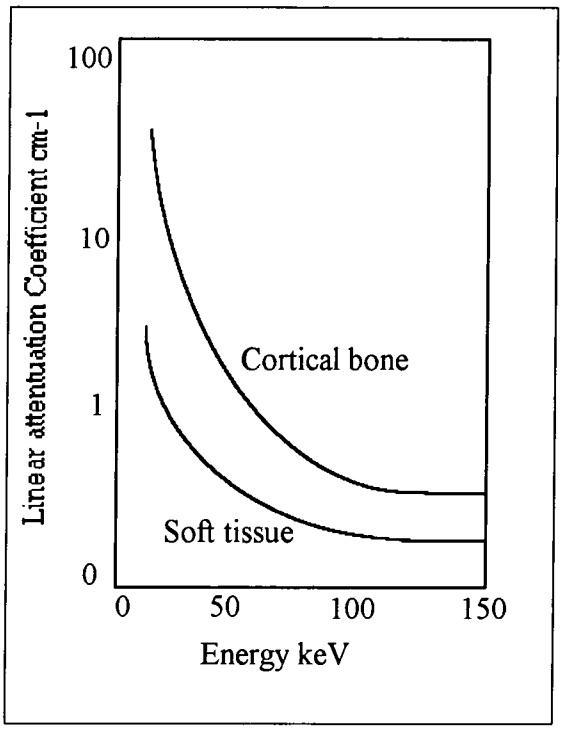

Figure 1.10. Variation with energy of the linear attenuation coefficient for soft tissue and cortical bone (From Webb, 1990).

Approximately 60 % of the weight of hydrated bone is due to bone mineral and 38 % of the bone mineral is calcium. The non-mineral components of bone include fat, collagen, and water of hydration. The composition of the bone mineral is essentially invariable, while the non-mineral components of bone and the composition of surrounding soft tissue vary considerably between individuals and over time. The data reduction algorithm used by Lunar makes corrections for the variability in the soft tissue composition. Data are corrected for dead time, spillover from the 70 keV channel into the 40 keV channel, background radiation, and beam hardening (Lunar Corp., 1991).

1.7.2 Optimum Energy Levels

It is possible in theory to perform dual energy absorptiometry measurements with any pair of energies, however a compromise needs to be made between patient dose and precision. With DPA photon energies were limited to the natural emissions of the radionuclide sources. However with DXA optimum energies can be selected by controlling the x-ray source.

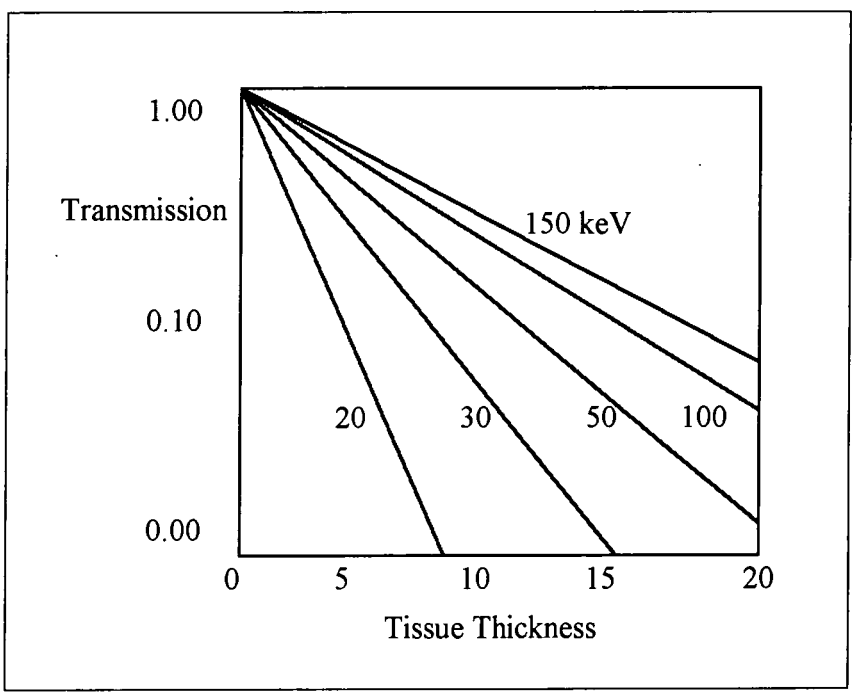

Figure 1.11. Transmission of monoenergetic photons through soft tissue. Curves are shown for photon beams with energies 20, 30, 50, 100 and 150 keV (From Webb, 1990).

It has been previously shown that the low energy photon level was critical in determining bone mineral measurements, not the high energy level. The low energy photons enable detection of very small changes in the two component system. Figure 1.11. shows the relationship between transmission and tissue thickness through soft tissue. For patients approximately 20 cm thick, scanned on a Lunar machine, the best

performance was achieved at 40 keV (Lunar Corp., 1988). For the high photon energy little improvement was observed in performance above 70 keV.

1.7.3 Precision and Accuracy

Mazess *et al.* (1989) evaluated a DXA (Lunar DPX) densitometer normally used for spine and femur scans, for accuracy and precision. Accuracy errors were determined by measuring the bone mineral content (BMC) of a bone phantom consisting of known quantities of calcium hydroxyapatite in flat plastic bags. Accuracy indicates how close a measured value is to the actual value. There was a linear increase of measured BMC with increasing calcium hydroxyapatite. To obtain good accuracy *in vivo* requires the results to remain stable for varying tissue thicknesses. Experiments carried out on different thicknesses of water ranging from 10 cm to 24 cm, observed no significant changes in measured bone mineral density (BMD) (Mazess *et al.*, 1989). Johnson *et al.* (1991) carried out similar trials with an aluminium phantom for the duration of 9 months with water thickness between 25.2 cm and 20.3 cm. Measured BMD and BMC remained stable. However, the measured BMD of an aluminium phantom studied over 9 months with a water thickness of 27.9 cm showed a steady updrift (Johnson *et al.*, 1991). This thickness of water is equivalent to a soft tissue thickness of over 30 cm which is rarely encountered. The accuracy error becomes larger for bones that are large and non-uniform in geometry. In such bones the accuracy error is estimated to be 4 % (Wahner *et al.*, 1985).

Precision is the ability of a methodology to repeatedly obtain the same value. The long term precision over six months of a spine phantom 18 cm thick was 0.6 % using a Lunar DPX scanner (n=195). The long term precision in one male subject was about 0.7 % (n=50) (Mazess *et al.*, 1989). Using the updated Lunar DPX-L scanner with a radiation flux 4 times larger than the Lunar DPX reportedly reduces precision errors by 50 % (Mazess *et al.*, 1992). Whilst precision *in vitro* is determined by fluctuations in

dose or radiation flux, the precision *in vivo* is affected by factors such as patient positioning, patient variability and relocating regions of interest.

Table 1.2. shows how various techniques of measuring bone mineral mass compare when considering accuracy, precision, examination time, absorbed dose of radiation and cost. Although each method is not always comparable in terms of scan site, an impression can be obtained of the relative performance of each densitometry technique. DXA has the best precision and accuracy.

Techniques for the measurement of bone mass.						
Technique	Site	Precision [1]	Accuracy [2]	Scan time	Absorbed dose of radiation[3]	Cost per scan
		%	%	min	mrem	$
Single photon absorptiometry	Proximal and distal radius, calcaneus	1-3	5	15	10-20	75
Dual energy photon absorptiometry	Spine, hip, total body	2-4	4-10	20-40	5	1-150
Dual energy x-ray absorptiometry	Spine, hip, total body	0.5-2	3-5	3-7	1-3	75-150
Quantitative computed tomography	Spine	2-5	5-20	10-15	100-1000	100-200

Table 1.2. Techniques for the measurement of bone mass. (From Johnston *et al.*, 1991). [1]Precision is the coefficient of variation for repeated measurements over a short period of time in young, healthy persons. [2]Accuracy is a measure of variation for measurements in a specimen whose mineral content has been determined by other means, *e.g.* ashed weight. [3]To convert millirems to millijoules per kilogram of body weight, multiply by 0.01.

1.7.4 DXA Systems

There are three different makes of DXA systems in Europe and North America; Hologic, Lunar and Norland. They all consist of an x-ray source, producing two different photon energies, a photon detector and a computer system for analysing the images with respect to the bone mineral content (BMC) and the bone mineral density (BMD) in specific regions of interest. However, the machines vary in how they produce the two energy sources.

The Hologic machine uses a dual-kV technique. Two sequential measurements at different kilovoltages are made. Figure 1.12. shows an example of dual-kV spectra. The x-ray tube is switched to produce alternate peak energies of 70 keV and 140 keV. Typically different beam filters are mechanically moved in and out of the beam between exposures. It also contains an internal calibration system, with a rotating filter wheel composed of a bone equivalent material, air and a soft tissue equivalent material. The detector on the Hologic machine measures photon transmission at each energy level separately and does not require energy discrimination.

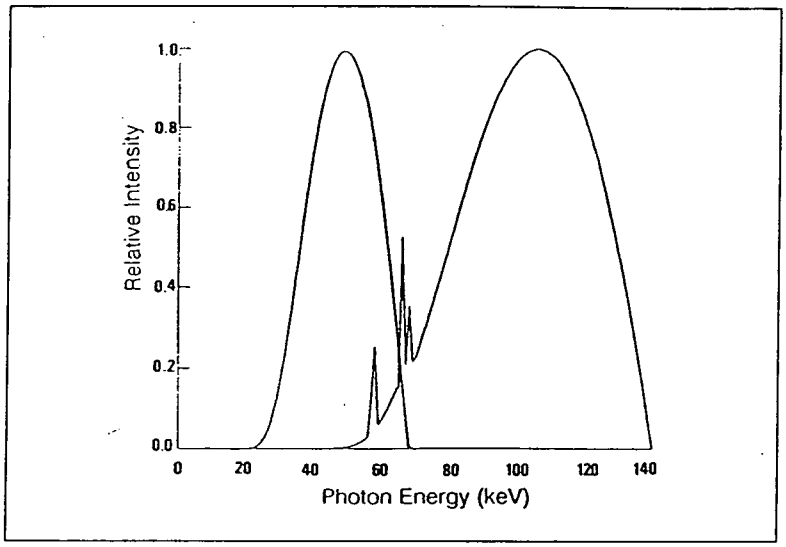

Figure 1.12. Dual-kV spectrum after transmission through 20 cm of water, with a 4 mm aluminium inherent filter and a 3.1 mm added copper filter in a 140 keV beam. (From Sorenson *et al.*, 1989)

The Lunar and Norland machines use a K-edge filter with the x-ray source to produce two photon energies. Figure 1.13. shows the principle of K-edge filtration. The output from the x-ray tube is filtered by a material that attenuates the photons above the K-shell absorption edge. From an initial broadband energy spectrum two relatively narrow energy bands are created. The Lunar DPX-L used for this research operates with energy bands of 40 keV and 70 keV. Lunar and Norland measure both energy levels simultaneously using an energy discriminating sodium iodide detector, so only a single exposure is required. The Norland detector consists of a thin and thick sodium iodide crystal, the thin crystal stops low energy photons and the high energy photons are transmitted and detected by the thick crystal (Kellie, 1992).

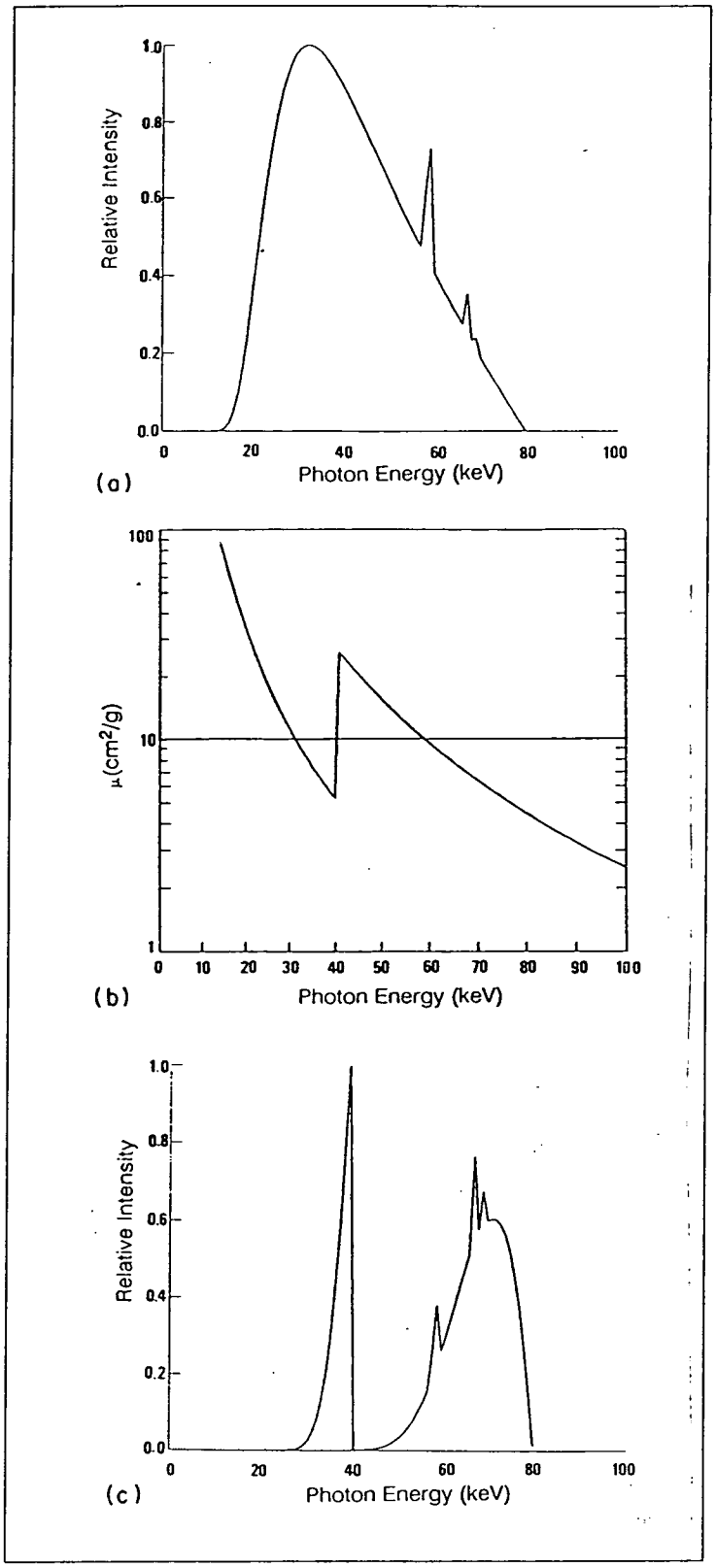

Figure 1.13. Principles of K-edge filtration. (a) Unfiltered output from the x-ray tube, 80 keV spectrum. (b) Attenuation coefficient versus energy for the filter material, cerium. (c) 80 keV spectrum filtered by 400 mg cm^{-2} cerium after transmission through 20 cm of water. (From Sorenson *et al.*, 1989)

1.7.5 Scanning Phantom Materials

When a phantom material is scanned using a machine that is set up for monitoring patients, the machine's algorithms may output incorrect values of data. The Lunar DPX-L scanner assumes that the materials in the scan path will be soft tissue and bone. When scanning a phantom corrections will have to be made, for example when using aluminium and perspex, in order to obtain accurate results for these materials.

The mass attenuation coefficients for bone, soft tissue and the phantom equivalent materials used for this project at 40 keV and 70 keV are listed in Table 1.3 (Hubbell, 1982). The chemical name for Perspex is polymethylmethacrylate (PMMA) (Brandrup *et al.*, 1989). Mass absorption coefficients for composite materials may be calculated by taking the average value of the absorption coefficients for the constituents weighted in proportion to their abundance by weight (Parthasaradhi *et al.*, 1992).

Table of mass attenuation coefficients ($cm^2\ g^{-1}$)				
Energy Level (keV)	Cortical Bone μ_b	Aluminium μ_a	Soft Tissue μ_s	Perspex μ_p
40	0.6400	0.5830	0.2605	0.2340
70	0.2651	0.2389	0.1921	0.1835

Table 1.3. Mass attenuation coefficients for biological and phantom equivalent materials.

Jonson gives slightly different values for aluminium of $\mu = 0.568\ cm^2\ g^{-1}$ at 40 keV and of $\mu = 0.230\ cm^2\ g^{-1}$ at 70 keV (Jonson, 1993). Using Lambert's law given in Equation 1.1. expressions can be obtained for the attenuation of the x-ray beams through a phantom of aluminium and perspex (Kaye, 1986). A prime superscipt denotes values at high energy levels.

Low energy $$\ln \frac{I_0}{I} = \mu_p m_p + \mu_a m_a$$ Equation 1.7.

High energy $$\ln \frac{I_0'}{I'} = \mu_p' m_p + \mu_a' m_a$$ Equation 1.8.

The scanner calculates the BMD from the algorithm given in Equation 1.5. with the mass attenuation coefficients being set for bone mineral and soft tissue. The scanner gives on output for the area density of the bone substitute denoted by m_{output}. If Equation 1.7. and Equation 1.8. for the phantom, are substituted into the scanner algorithm, the following equation is obtained. The ratio, in terms of mass per area of region of interest, g cm^{-2} for perspex to aluminium is given by $m_p = x\, m_a$.

$$m_{output} = \frac{\mu_s'\left[\mu_p m_p + \mu_a m_a\right] - \mu_s\left[\mu_p' m_p + \mu_a' m_a\right]}{\mu_s'\mu_b - \mu_s\mu_b'}$$ Equation 1.9.

Substituting $m_p = x m_a$ into Equation 1.9. gives Equation 1.10.

$$m_{output} = \frac{m_a\left[x\left[\mu_s'\mu_p - \mu_s\mu_p'\right] + \left[\mu_s'\mu_a - \mu_s\mu_a'\right]\right]}{\mu_s'\mu_b - \mu_s\mu_b'}$$ Equation 1.10.

Basically Equation 1.10. is a linear equation where x is the ratio of the mass of perspex to aluminium in the region of interest, and can be written in the form $y = j\,x + k$. This expression, for a particular phantom, gives the measured bone mineral density value of the bone substitute that is calculated and output by the densitometer, which assumes actual bone and soft tissue are present in the scan path and not aluminium and perspex.

1.8 Phantoms

Following the discovery of x-rays, materials were sought that would attenuate x-rays in the same manner as different patient tissues. These "patient substitutes" are referred to as phantoms. Water was the first tissue substitute used in radiation measurements followed by wax in 1923 (White *et al.*, 1986). More recently plastics and rubbers have been used for tissue simulation. These materials allow a range of complex organ and body phantoms to be manufactured. Since 1970 tissue substitutes have been

formulated which have radiation absorption and scattering characteristics within 5 % of the corresponding real tissue. The "reference man" data by the International Commission on Radiological Protection (ICRP) has been used in the development of many different phantom tissue types, ranging from soft to skeletal tissue and from brain to thyroid (White *et al.*, 1988).

1.8.1 Tissue Equivalence

The definition of a tissue equivalent material is one that has radiation absorption and scattering properties within 1 % of the tissue material it is trying to simulate (White *et al.*, 1988). Materials whose properties less accurately match are described as tissue substitutes. Ideally the phantom material used should have matching radiation absorbing characteristics for photon, electron and neutron interaction, the same effective atomic number and the same specific gravity as the corresponding real tissue.

When an x-ray passes through matter, *e.g.* body tissue, energy is given to the tissue and the intensity of the beam is reduced or attenuated. In the interaction, some of the energy is scattered and some is absorbed. Absorption can cause excitation in which an electron is released to a higher energy level within the atom or molecule. Alternatively ionisation may occur in which the electron is removed. There are basically four attenuation mechanisms (Figure 1.14.).

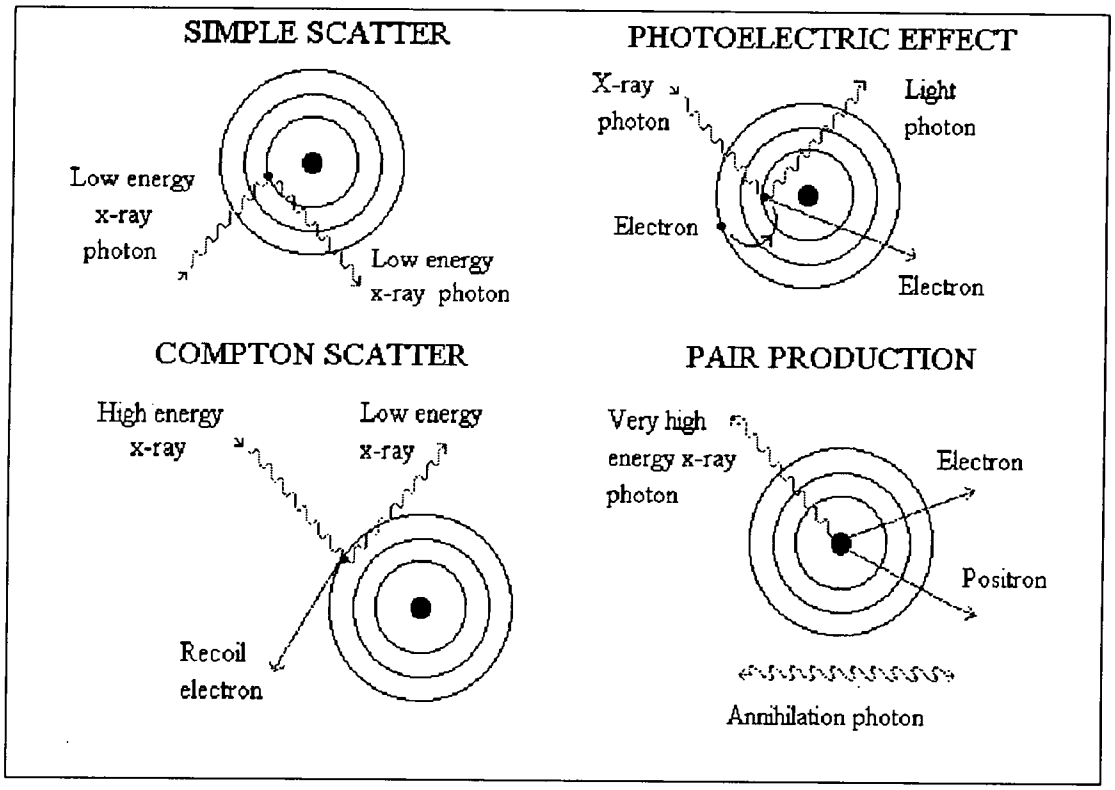

Figure 1.14. Photon interactions and attenuation mechanisms.

Simple scatter occurs when the energy of the x-ray photon (E) is smaller than the binding energy (E_b) required to remove an electron from an atom. The photoelectric effect occurs when the photon energy is slightly greater than E_b and ejects an electron from the atom. Another electron then "drops" into the vacancy, emitting light photons (Cullity, 1967). Compton scatter occurs when the photon has much more energy than E_b. Consequently a photon of reduced energy is scattered from the interaction with the ejected electron, which is known as a recoil electron. At very high energies pair production occurs. The photons interact with the atomic nucleus. The photon disappears and an electron and positron emerge. These lose their energy by ionisation until a positron is annihilated by an electron generating two identical photons (Hollins, 1991). Virtually all of the photon interactions using a Lunar DPX-L scanner will be due to the photoelectric effect and compton scatter.

Primarily it is the atomic number (Z) of the material which governs the interaction of x-rays with a material. The atomic numbers should match as closely as possible between the phantom and the real tissue, thus maintaining a similar ratio between photoelectric effect and Compton scattering interactions. It is the size of the nucleus which is most important. From the data in Table 1.4. an effective atomic number can be calculated for each tissue. The effective atomic number for cortical bone given by Aird (1975) was Z=13. Aluminium has the same value of Z=13 hence for this reason it is often used as a phantom material for cortical bone.

Elemental Composition											
Tissue	H	C	N	O	Na	Mg	P	S	Cl	K	Ca
Atomic number	1	6	7	8	11	12	15	16	17	19	20
Cortical bone	3.39	15.5	3.97	44.1	0.06	0.21	10.2	0.31	-	-	-
Inner bone	8.66	40.3	2.58	40.4	0.08	0.06	2.30	0.46	-	0.23	4.97
Adipose	12.0	64.0	0.80	22.9	0.05	-	0.02	0.07	0.12	0.03	-

Table 1.4. Elemental composition of hard and soft tissues by weight (White *et al.*, 1988).

The probability of interaction by photoelectric effect is proportional to Z^4 of the material. The probability of interaction by Compton scattering is proportional to the electron density, which is relatively constant for most materials. Therefore by keeping the atomic number of the phantom similar to actual tissue, the ratio of photoelectric effect and Compton scattering will remain constant (Figure 1.15.).

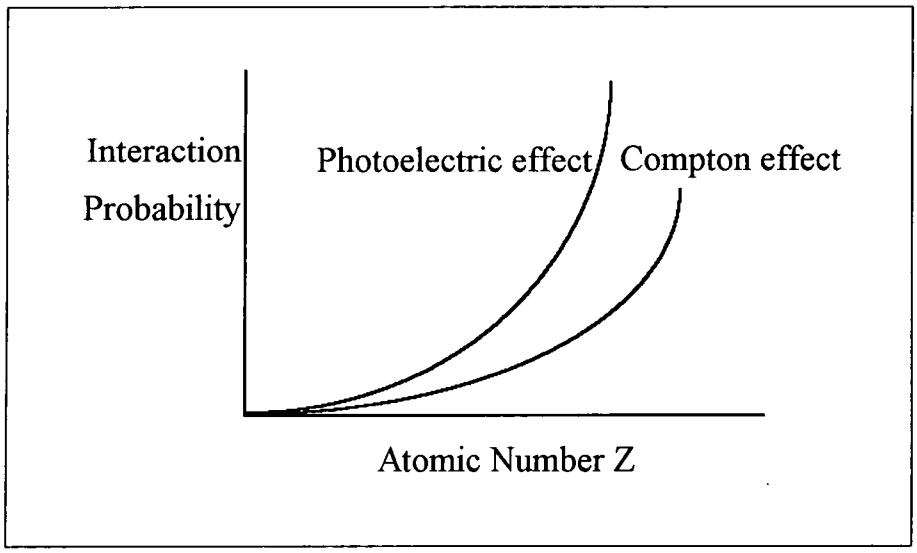

Figure 1.15. The interaction probability by photoelectric or Compton effect with the atomic number of a material.

As was mentioned previously, the density of the tissue equivalent material should match the real tissue. Table 1.5. shows the density values for various tissues and their phantom equivalents.

Material Density			
Tissue	Density (kg m^{-3})	Tissue	Density (kg m^{-3})
Cortical bone [1.]	1850	B110 [1., 2.]	1790
Inner bone [1.]	1120	Aluminium	2700
Soft tissue [1.]	1030	Perspex	1190
Adipose tissue [1.]	920	Glycerol	1262
		Water	998

Table 1.5. Table of material densities. [1.]From White *et al.* (1988). [2.]Cortical bone phantom material.

Pair production need not be considered as it requires photon energies above 1.2 MeV. These values are very high and are not used for dual energy x-ray absorptiometry.

1.8.2 Phantom Materials

Many soft tissue substitutes have been produced from ICRP reference man data. TST/L3, a total soft tissue material is a water based substitute containing urea, ethanol, and ethylene glycol (White *et al.*, 1988). Perspex (polymethylmethacrylate), glycerol and water can be used individually as close approximations to soft tissue. They all have similar mass attenuation coefficients and densities, and additionally they are cheap and readily available.

The composition of cortical bone adopted by the ICRP's reference man in 1970 was derived from Woodard's work in 1962 and was used to replace the International Commission on Radiological Units' (ICRU) definition of bone (Spokas *et al.*, 1982). Using this composition a cortical bone substitute for phantoms was designed called B110. The components of B110 were chosen to satisfy the criteria for tissue equivalence. To provide adequate neutron response this cortical bone simulation had 3.97 % Nitrogen and 3.39 % Hydrogen by weight. The minimum free carbon content was 14 % to provide sufficient electrical conductivity. To set the photon response at both a high and a low energy, equal to the response of real bone, the Compton mass attenuation and the total photon mass attenuation values were also set to Woodard's values. Tests carried out on the new mixture to assess the photon and electron interactions demonstrated a high degree of equivalence over the energy range 0.01 to 100 MeV (Spokas *et al.*, 1982). B110 is the most accurate simulated cortical bone material currently available and is ideally suited for radiographic and dosimetric studies in diagnostic radiology. It has good mechanical properties and is suitable for machining, but it is very expensive.

Other bone phantoms may be used including solutions of calcium or potassium salts, similar suspensions in plastic and actual bone or ivory. Proposals for a standard phantom for use in QCT or DXA measurements of spinal bone mineral used calcium hydroxyapatite in an epoxy-resin-based material as a bone substitute (Kalender, 1992). This allows the density of the phantom to be easily varied. Alloys of aluminium with zinc and other elements provide very close approximations to bone. However, the most readily available and cheapest bone phantom material is aluminium (Tothill, 1989).

CHAPTER 2
Phantom Trials

2.1 Materials and Methodology

Studies were carried out using phantoms to assess the viability of using dual energy x-ray absorptiometry (DXA) for the monitoring of tibial fracture healing in patients. The factors under consideration included whether the machine was sensitive enough to detect small fracture gaps of different configurations and whether the scanner was able to measure small areas of low mineral density which one would expect at a fracture site. A methodology for the analysis of patient data was also established using the phantoms and the reproducibility of results was determined. Three different groups of phantoms were designed for these trials and these will be described below.

2.1.1 Phantoms

The first group of phantoms consisted of a simple aluminium block and a perspex section; these were used to simulate bony tissue and soft tissue respectively. Three aluminium plates were manufactured with thicknesses of 10 mm (Phantom A.), 20 mm (Phantom B.) and 30 mm (Phantom C.), each of width 25 mm and length 150 mm. They were positioned upon a perspex block of thickness 39 mm (Figure 2.1.). Both aluminium and perspex are good tissue equivalent materials for bone and soft tissue respectively, which are cheap, easy to manufacture and readily available (White *et al.*, 1988). The aluminium phantoms, A, B and C were each scanned 5 times to examine

the variation of bone mineral density (BMD) with aluminium thickness. In addition the phantoms were each scanned 5 times with no soft tissue substitute present. These experiments were used to establish whether the simple aluminium phantom could be successfully scanned and to establish the appropriate data collection and analysis method for the specimens. The relationship between the true area density of aluminium and the mineral density output from the scanner was also obtained from these experiments.

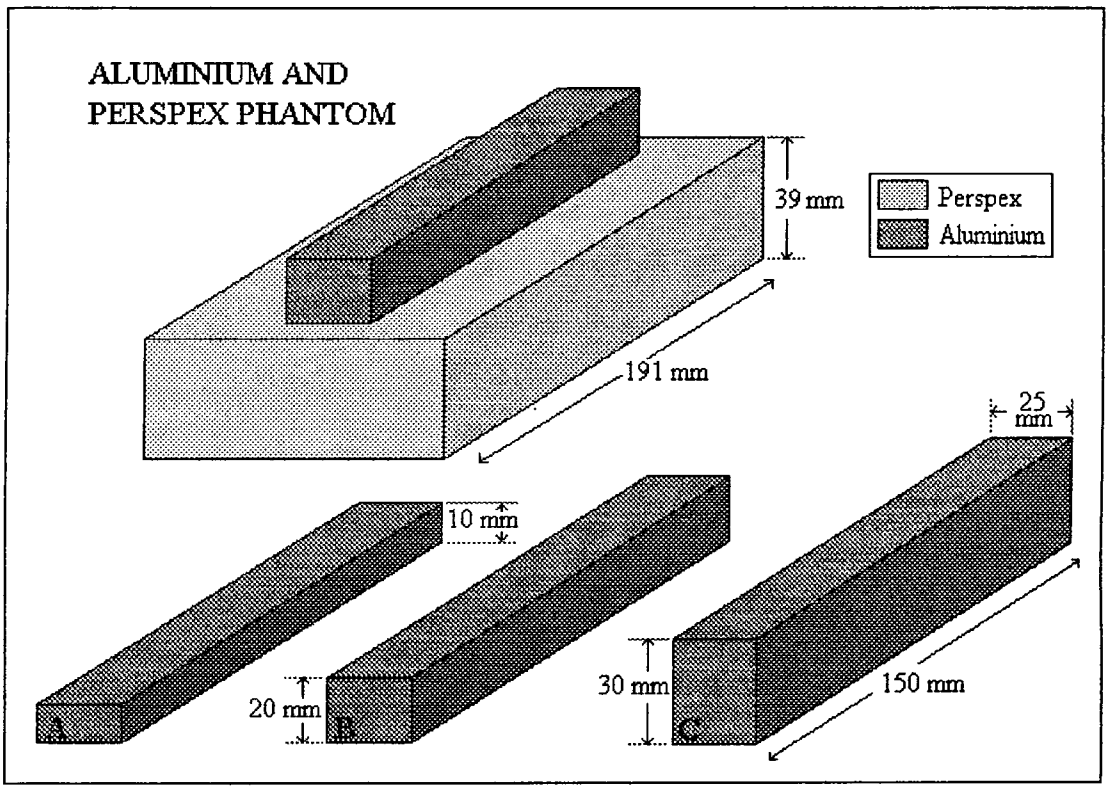

Figure 2.1. Diagram of the aluminium and perspex phantom consisting of 3 aluminium blocks of length 150 mm and width 25 mm. The thickness of A is 10 mm, B is 20 mm and C is 30 mm.

The second group of phantoms, labelled 1, 2 and 3, consisted of a cylindrical aluminium tube, giving a better representation of tibial geometry, mounted on a perspex block (Figure 2.2). One of the aluminium tubes was bisected to represent a transverse fracture and another had an oblique fracture created, oriented at 60° to the longitudinal axis. To study soft tissue effects, phantom 1 was scanned 5 times with the perspex base and subsequently the experiment was repeated with a variety of soft

tissue substitutes to replace the perspex, including different depths of water. Each soft tissue substitute was also scanned 5 times. Phantoms 2 and 3 were used to assess the sensitivity of the DXA scanner in detecting small fracture gaps. The phantoms were set with decreasing gap widths using a feeler gauge, before repeatedly scanning 5 times. This group of phantoms was used to establish a protocol for monitoring patients, assess the sensitivity of the machine for different fracture gaps and configurations and to monitor the reproducibility of the results.

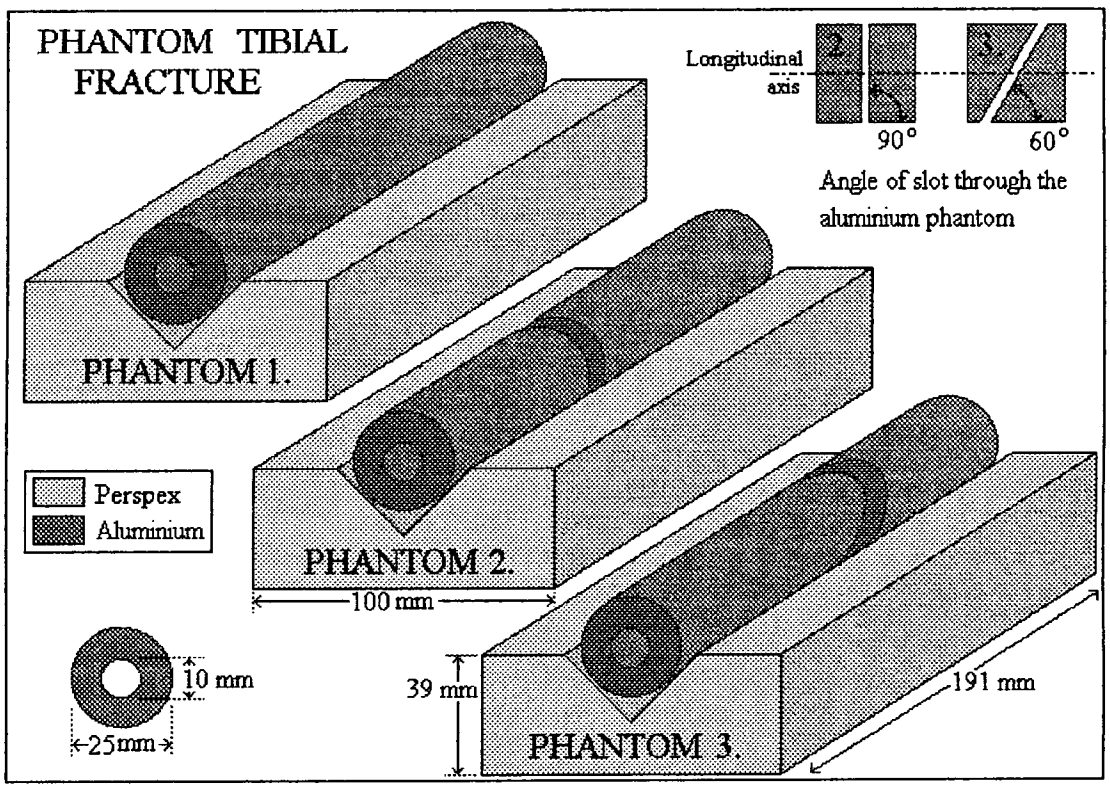

Figure 2.2. Diagram of the phantom tibial fractures. 1. No gap is present. 2. A transverse gap is present. 3. An oblique gap 60° to the longitudinal axis is present.

The third group of phantoms consisted of 28 small calcium hydroxyapatite samples which were used to determine the sensitivity of the DXA scanner when measuring areas of low density. Calcium hydroxyapatite was roughly shaped into small pellets by hand and baked at 180 °C for approximately 30 minutes until they had hardened. The pellets were then finally shaped using a scalpel and fine emery paper to smooth each surface into rectangular shapes. The dimensions and mass of each sample was

measured 3 times before scanning and 3 times after scanning. The 28 samples ranged in thickness from 2.0 mm to 7.3 mm. The hydroxyapatite phantoms were used to assess the sensitivity of the DXA scanner in monitoring areas of low bone mineral density, likely to be found at a fracture site.

2.1.2 Scanner

A Lunar DPX-L scanner situated at South Cleveland Hospital, Middlesbrough, U.K., in conjunction with the forearm software supplied for use with this scanner, was used to acquire and analyse the data.

The software has two main functions, data acquisition and data analysis. The data acquisition level had several settings which had to be set before the scan could commence. The mode setting describes the speed of the scan, with fast mode (the standard operating speed), medium mode and slow mode available. The slowest mode is seldom used except for scanning excessively overweight patients and has a corresponding higher patient dosage than the fast mode. Table 2.1. shows the settings used for the phantom trials. The data acquisition levels were set at the same values as those used for patient scanning.

Acquisition Data	
Forearm length	200 mm
Patient side	Left
Mode	Fast
Voltage (kVp)	76
Current (μA)	150
Collimation	Fine
Sample size	0.6 x 1.2 mm
Sample interval (s)	1 / 64
Scan width	80 mm
Scan length	120 mm

Table 2.1. The acquisition data level settings of the forearm software for the phantom trials.

In addition personal data had to be entered into the computer in order to carry out the scan. This was kept constant for each trial. The personal data required included information on the patient's height, weight, ethnic origin and sex. This personal information is normally used to compare the bone mineral density values of the ulna and radius of a particular patient with the values of a reference population. However, for these trials no comparison of phantom results were made with a reference population, so the personal data had no effect.

The data analysis level was designed for the analysis of the forearm. There are 2 options available, auto analysis and manual analysis. The auto analysis detects the bone and soft tissue boundaries and locates specific regions of interest on the radius and ulna of a forearm scan. The manual analysis option allows the operator to locate a region of interest (ROI) of any size, in any position on the scan. This facility was used to analyse the phantom results and obtain values of the bone mineral density (BMD) in units of g cm^{-2} and the bone mineral content (BMC) measured in g, at a particular region of interest. The time for each phantom scan was 4 minutes, 18 seconds.

2.2 Results

2.2.1 Soft Tissue Effects

The aluminium phantoms A, B, and C were scanned repeatedly both with and without the perspex present. When no soft tissue substitute was used during the scan, the display on the computer monitor linked to the DXA scanner gave a very poor image, making repositioning between scans very difficult. It addition, it was not possible to discern the edge profile of the phantom. However, after leaving the data acquisition mode it was possible to obtain bone mineral density values by placing ROIs on to the phantom, during the data analysis mode. During the analysis stage a clearer image was displayed. Figure 2.3. shows the BMD values obtained with and without a soft tissue

substitute present, the values of BMD obtained without the perspex being consistently lower than the trials incorporating perspex. Due to the problems associated with not using a soft tissue substitute, causing a poor scan image and making repositioning difficult, all further phantom studies were carried out with a soft tissue substitute present.

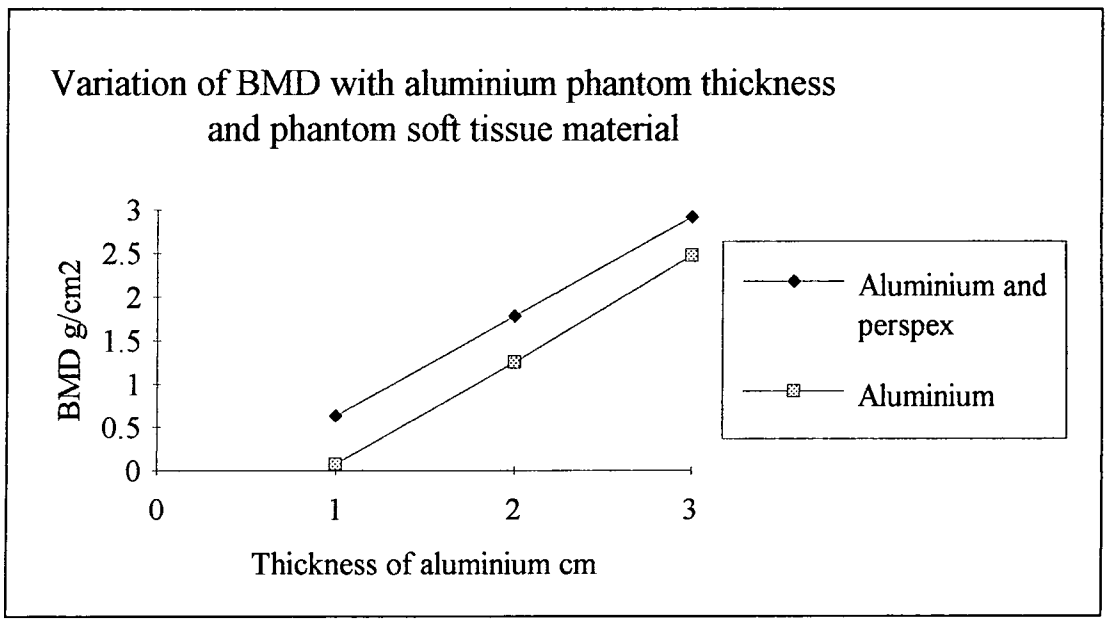

Figure 2.3. A graph showing the variation of BMD with aluminium thickness and phantom soft tissue material.

The cylindrical aluminium phantom (Phantom 1) was scanned 5 times with a variety of soft tissue substitutes to examine what effect, if any, these would have on the image during scanning, the bone mineral density (BMD) output values and the reproducibility of the results. The soft tissues tested included perspex, a polythene board and a water tank both with and without water. The phantom was analysed by placing a region of interest (ROI), of dimensions 1.2 mm by 2.4 mm, at adjacent intervals across the width of the phantom and recording the BMD data for each ROI. The results are shown in Figure 2.4. The change in BMD across the width of the phantom due to the geometry of the cross-section is clearly visible, as one might expect.

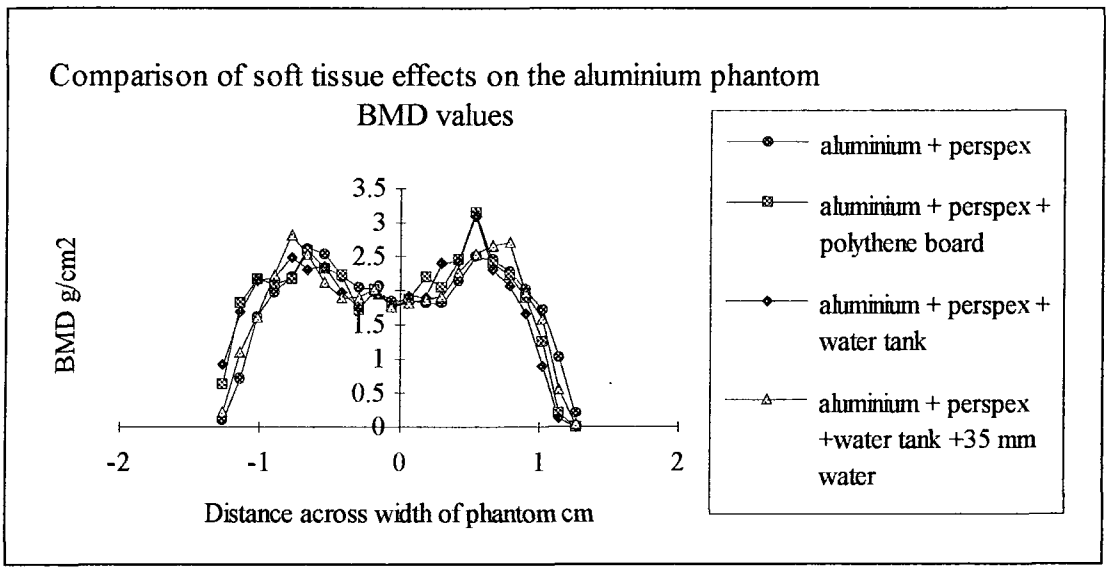

Figure 2.4. A graph showing the effect of different phantom soft tissue materials on the BMD output values on the Lunar DPX-L scanner.

The variation between output values for the different phantom compositions is negligible (Figure 2.4.). Each scan gave a clear image on the computer monitor allowing repositioning of the phantom between scans to be checked. The polythene board was used since occasionally it has been used by the radiographers to improve the image of the forearm or tibia, given on the computer monitor whilst scanning the patient. It appeared to make no noticeable difference to the BMD values of the aluminium and perspex phantom. It would seem reasonable therefore to assume that it would also have a negligible effect upon the results of any patient data. The effect of positioning a thin plastic water tank in the region of the scan also made no noticeable difference to the BMD values obtained for the aluminium phantom.

The use of water as a soft tissue substitute was investigated further by carrying out trials using Phantom 1, placed in a water tank and submerged beneath a depth of water ranging from 10 mm to 60 mm, in 10 mm intervals. The results were analysed using a region of interest the width of the cylinder, 25.2 mm and 4.8 mm long (Table 2.2.).

Table of the effects of varying the depth of water above the aluminium phantom.						
Depth of water above the aluminium phantom.	10 mm	20 mm	30 mm	40 mm	50 mm	60 mm
Average BMD g cm^{-2}	1.351	1.824	1.899	1.941	1.933	1.907
Standard deviation g cm^{-2}	0.015	0.017	0.018	0.022	0.028	0.022
Coefficient of variation.	1.1 %	1.0 %	0.9 %	1.1 %	1.4 %	1.2 %

Table 2.2. The effects of varying the depth of water above the aluminium phantom on the value of BMD output by the scanner.

With depths of water above 20 mm the BMD values remain relatively constant, between 1.899 g cm^{-2} and 1.941 g cm^{-2} and the reproducibility of results is good with coefficients of variation of less than 1.5 %. The values are comparable to those of using the perspex base alone. With water thicknesses of less than 30 mm the average BMD begin to decrease.

Table summarising the effects of varying the soft tissue substitutes with the aluminium phantom.					
Soft tissue substitute material	Perspex	Perspex + polythene board	Perspex + water tank	Perspex + water tank + 35 mm water	Water tank + 30 mm water
Average BMD g cm^{-2}	1.918	1.924	1.927	1.905	1.899
Standard deviation g cm^{-2}	0.022	0.030	0.037	0.025	0.018
Coefficient of variation	1.1 %	1.5 %	1.9 %	1.3 %	0.9 %

Table 2.3. Summary of the effects of varying the soft tissue substitutes with the aluminium phantom.

The bone mineral density output was compared for all of the soft tissue substitutes (Table 2.3.). There is very little difference between each combination of phantom.

The best reproducibility was obtained using the aluminium and water phantom, giving a coefficient of variation of 0.9 %. However the results were similar for the phantom using only perspex as a soft tissue substitute, giving a coefficient of variation of 1.1 %. Hence, for all further aluminium phantom trials a soft tissue substitute of perspex was used, as it was simple, consistent in size and gave good, reproducible results.

2.2.2 ROI Size

Using the unfractured cylindrical aluminium phantom, five repeated scans were taken and analysed to establish the optimum size of ROI (region of interest) to use for the patient trails. The ROI was adjusted to cover the width of the bone, to reduce any error in calculating the bone mineral content (BMC) due to the orientation of the limb about its longitudinal axis. The width of the ROI is limited to multiples of 0.6 mm, the minimum pixel width. The length of the ROI is limited to multiples of 1.2 mm, which is the smallest possible pixel length. In choosing a suitable ROI length, a compromise needed to be made between maintaining sensitivity, keeping the coefficient of variation low and keeping the analysis time to a practical level. The dimensions of the regions of interest which were tested were 25.2 mm wide (the width of the phantom) and set at lengths from 1.2 mm to 9.6 mm. The coefficient of variation and the average bone mineral density (BMD) for each set of results was calculated and is shown in Figure 2.5. and Figure 2.6. respectively.

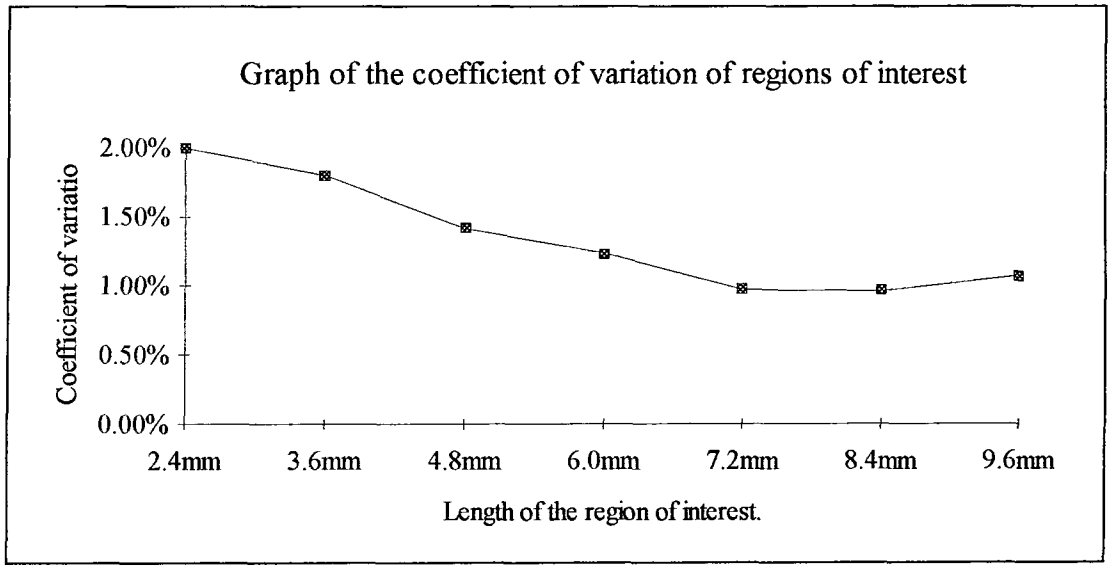

Figure 2.5. Graph showing the change in coefficient of variation for a cylindrical aluminium phantom analysed using a region of interest of constant width, 25.2 mm and increasing length from 2.4 mm to 9.6 mm.

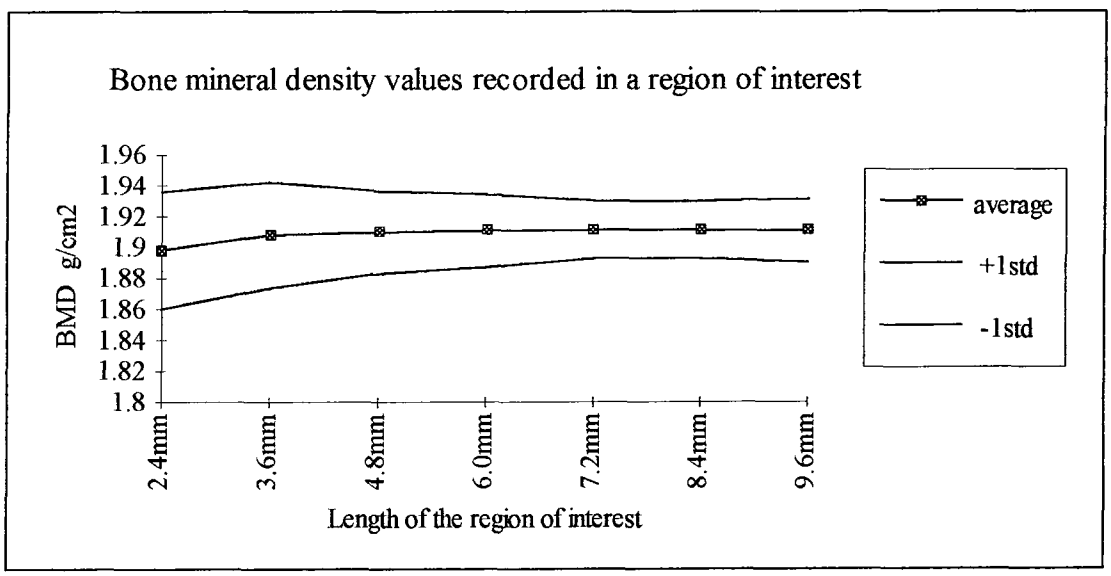

Figure 2.6. Graph showing the change in average bone mineral density for a cylindrical aluminium phantom analysed using a region of interest with a constant width of 25.2 mm and increasing length.

Using an ROI of length 4.8 mm, the coefficient of variation is below 1.5 %. and the standard deviation of results is approximately the same as for analysis carried out with larger ROIs. In addition the length of the tibia which was scanned in the patient trials was normally between 15 cm and 20 cm. To analyse a tibia using an ROI of length 4.8

mm would require between 30 and 40 ROIs along its length. A smaller ROI of length 3.6 mm would require about 45 to 55 regions along its length and a larger ROI of length 6.0 mm would require less than 20. It was decided that a region of interest 4.8 mm wide was the best size to use in all future analyses.

2.2.3 Relationship of Measured and True Density

In the study, the analysis of patient or phantom data was mainly concerned with relative changes in BMD readings between scans or across fracture sites. However, it is possible to correlate the scanner BMD output and the true area density of a particular bone phantom. A linear relationship between the two values can be derived both theoretically and calculated from the experimental results. This may demonstrate that the scanner can give true values of BMD for a material of known properties. It may also prove useful if true values of the area density of a bone phantom are required. Using an equation which relates true values to output values, it is very simple to convert the scanner output into accurate readings of bone mineral density.

From theory (Section 2.7.5) a simplified model which assumes the radiation quality and geometry are such that the photon energies perfectly obey Lambert's Law gives Equation 2.1. Equation 2.1. describes the attenuation of photon beams through a two component phantom of aluminium and perspex.

$$m_{output} = \frac{m_a\left[x\left[\mu'_s\mu_p - \mu_s\mu'_p\right] + \left[\mu'_s\mu_a - \mu_s\mu'_a\right]\right]}{\mu'_s\mu_b - \mu_s\mu'_b} \qquad \text{Equation 2.1.}$$

This expression above can be simplified to a linear equation, $y = jx + k$; Where x is the ratio of the area density of perspex (m_p) to aluminium (m_a) and y is ratio of the true area density of aluminium (m_a) to the bone mineral density output by the scanner (m_{output}). The constants j and k depend on the attenuation coefficients of each

material. Equation 2.1. gives the measured bone mineral density value of the phantom that is calculated and output by the densitometer. The Lunar software assumes actual bone and soft tissue are present in the scan path, not aluminium and perspex.

Table of mass attenuation coefficients ($cm^2\ g^{-1}$)			
Energy Level	(keV)	40 (μ)	70 (μ)
Cortical Bone [1]	μ_b	0.6400	0.2651
Soft Tissue [1]	μ_s	0.2605	0.1921
Aluminium [1]	μ_a	0.5830	0.2389
Hydroxyapatite [2]	μ_h	0.9880	0.3130
Perspex [1]	μ_p	0.2340	0.1835
Water [1]	μ_w	0.2605	0.1945

Table 2.4. Mass attenuation coefficients for biological and phantom equivalent materials ([1] Hubbell, 1982 and [2] Jonson, 1993).

The mass attenuation coefficients for the soft and hard tissues and the phantom materials are given in Table 2.4. at energy levels of 40 keV and 70 keV, which are the two photon energy levels at which the Lunar DPX-L operates. Using this data, the constants j and k can be calculated for a particular phantom configuration and substituted into Equation 2.1. This will then give the theoretical relationship between the actual area density for a bone phantom and the bone mineral density output from the scanner (Table 2.5.).

Relationship derived theoretically, between phantom materials and the bone mineral density output from the Lunar DPX-L scanner.		
Material	Bone substitute	
Soft tissue substitute	Aluminium m_a	Hydroxyapatite m_h
Perspex m_p	$\frac{m_{output}}{m_a} = -0.053\frac{m_p}{m_a} + 0.923$	$\frac{m_{output}}{m_h} = -0.053\frac{m_p}{m_h} + 2.008$
Water m_w	$\frac{m_{output}}{m_a} = -0.012\frac{m_w}{m_a} + 0.923$	$\frac{m_{output}}{m_h} = -0.012\frac{m_w}{m_h} + 2.008$

Table 2.5. Theoretical relationship between phantom materials and bone mineral density output from scanner.

From the experiments carried out on the three aluminium and perspex specimens, A, B and C, the BMD output values can be plotted versus the true values of aluminium area density on a graph. A relationship can be derived, using the least squares method, to calculate a best fit line, for the relationship between the output and true values of aluminium area density. Linear regression lines can also be calculated for the hydroxyapatite phantoms. The constants of j and k are different to those obtained from the simple model given in Table 2.5. The equations in Table 2.6. were derived from the results of the phantom trials and show the experimental relationship between the actual area density and the scanner output BMD. The scanner output for all of the tested phantoms, was very well correlated with the true area density values. The coefficients of determination for each relationship, given by r^2, are very high (Table 2.6.). These equations allow accurate BMD values to be calculated for the bone phantoms after data has been obtained from the scanner output.

Relationship derived experimentally, between phantom materials and the bone mineral density output from the Lunar DPX-L scanner.		
Phantom composition	r^2 (a)	Equation
Aluminium and perspex	0.965	$\frac{m_{output}}{m_a} = -0.125\frac{m_p}{m_a} + 0.423$
Hydroxyapatite and perspex	0.973	$\frac{m_{output}}{m_h} = -0.002\frac{m_p}{m_h} + 0.820$
Hydroxyapatite and water	0.989	$\frac{m_{output}}{m_h} = -0.006\frac{m_w}{m_h} + 0.830$

Table 2.6. Experimental relationship between phantom materials and bone mineral density output from scanner. (a) r^2 is the coefficient of determination for the linear regression line through the experimental data points used to derive the equations.

As can be seen from Table 2.5. and Table 2.6. the theoretical and the experimental relationships are different. If for example a 1 cm thickness of aluminium is scanned with a 3.9 cm thickness of perspex, the BMD scanner output will be 25 % of the calculated theoretical value. The accuracy for the calcium hydroxyapatite phantom is slightly better. For a 1 cm thickness of hydroxyapatite and a soft tissue substitute of perspex of thickness 3.9 cm, the BMD output is 47 % of the theoretical value. Using a soft tissue substitute of 3 cm of water as a soft tissue substitute gives a BMD output value of approximately 92 % of the theoretical BMD value. The equations derived from theory (Table 2.5.) calculated the coefficients j and k by assuming that the photon beams perfectly obeyed Lambert's Law of attenuation through a material. However, in practice this is not the case and errors occur due to the imperfect behaviour of the photon beams, such as scattering and reflection. This may help to account for the different values of the coefficients j and k in the experimentally derived relationships (Table 2.6.). These experimental equations can be used to convert the scanner BMD

output results for a particular phantom, to the true area density values of the bone substitute.

Since the relationship between m_a or m_h, and m_{output} is linear for a given phantom, it is possible to assess relative changes in phantom area density without needing to convert each output value to its true value.

2.3 Gap Size and Orientation

The cylindrical aluminium phantom, Phantom 2, was used to simulate a simple transverse fracture. Fracture gaps of between 0.05 mm and 1.0 mm were produced using a feeler gauge and 5 repeated scans were taken for each fracture gap setting. The phantom was analysed by using a region of interest (ROI), the width of the phantom, 25.2 mm, by 4.8 mm long. With this configuration of fracture, the gap was discernible upon the computer monitor, even at its minimum width of 0.05 mm. An ROI was located directly over the fracture gap to record the minimum value of BMD and additional ROIs were placed adjacent to each other along the length of the phantom to measure the unfractured bone mineral density of the phantom. The results obtained are shown in Figure 2.7.

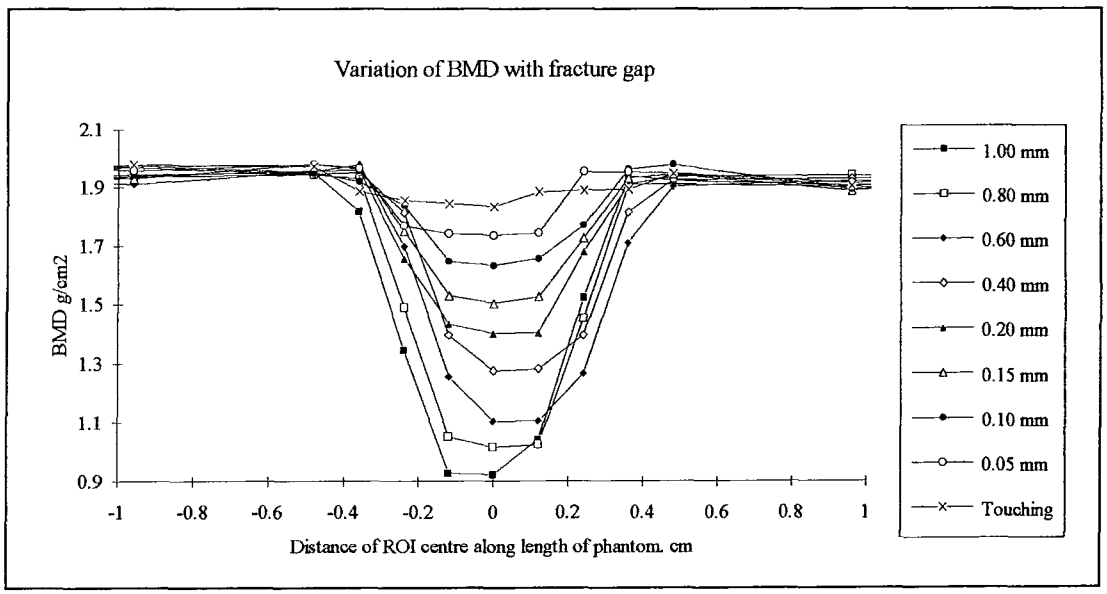

Figure 2.7. A graph showing the variation of BMD along the length of an aluminium and perspex phantom with a transverse fracture gap. The dimensions of the ROI were 25.2 mm by 4.8 mm.

The BMD in a region of interest containing no fracture gap was calculated. From this value the percentage decrease was also calculated for a similar region of interest containing a certain width of fracture gap and was described as the theoretical BMD across a fracture site. The BMD experimentally measured in a region of interest including a fracture gap was expressed as a percentage of the maximum BMD, *i.e.* the BMD in a region of interest not including a fracture gap. The experimental and the theoretical results were compared and are shown in Figure 2.8.

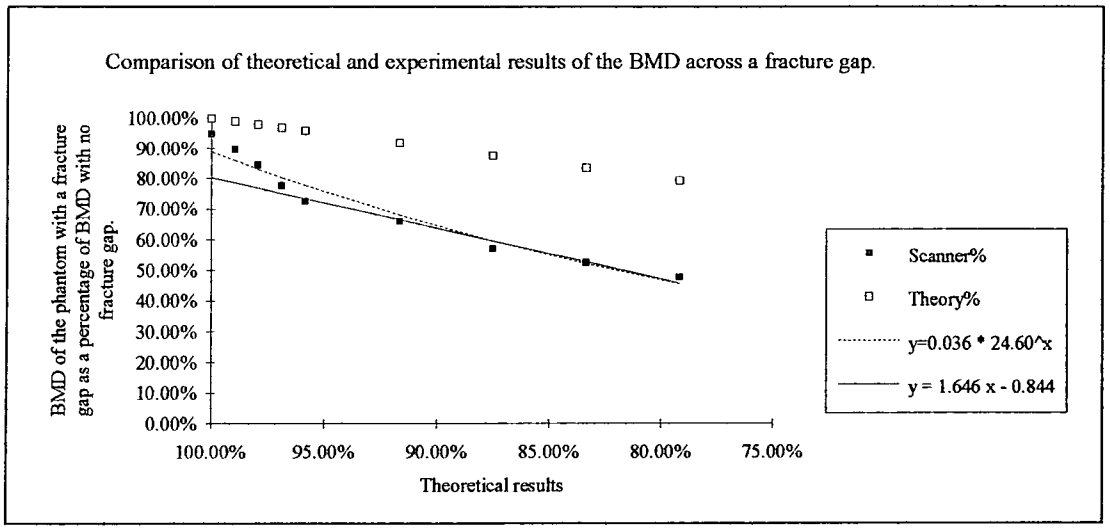

Figure 2.8. A comparison of the theoretical and experimental BMD values across a phantom fracture gap. The region of interest was 25.2 mm wide, the width of the aluminium phantom, and 4.8 mm long, the same as that used on patient analysis.

The ratio of the BMD actually measured across the fracture gap, to the BMD of an equivalent region of interest containing no fracture gap, is denoted by y. The ratio of the BMD expected across the fracture gap, to the BMD of an equivalent region of interest containing no fracture gap, is described as the theoretical result and is denoted by x. An exponential curve, $y = 0.036 * 24.60^{x}$, was fitted to the experimental results with a coefficient of determination of $r^2 = 0.96$. A linear line, $y = 1.646\,x - 0.844$, was also fitted to the same results with a coefficient of determination of $r^2 = 0.975$. Both results showed a significance of $P<0.05$ for a one tailed t-test. The F-observed value for both equations is substantially greater than the F-critical value from a single tailed test. Therefore the regression equations obtained are useful in predicting the BMD across the fracture site of the phantom and are unlikely to have been obtained by chance.

It is interesting to note that the experimental results show a more pronounced presence of a fracture gap than it should in theory. This could be due to factors such as beam hardening and reflection of the photons, as well as the fact that the scanner is

small fracture gaps are highly detectable using the phantom model, then this could be advantageous in the monitoring of low bone mineral density changes during fracture healing.

In a clinical situation it is unlikely that a neat transverse fracture would be observed. Consequently, a phantom was constructed to simulate an oblique fracture. The oblique fracture gap was orientated in two positions (Figure 2.9.). The first set of tests were carried out with the fracture gap parallel to the path of the x-ray beam such that the photons could pass through unobstructed. The second set of tests was carried out on the same aluminium phantom but after it had been rotated about its longitudinal axis by 90°, such that the fracture gap was almost perpendicular to the path of the x-ray. The fracture gap was set at widths of 0.2 mm, 0.1 mm and 0.5 mm using a feeler gauge and scanned five times at each setting. Analysis of the results was carried out by locating regions of interest 25.2 mm wide and 4.8 mm long, adjacent to each other along the length of the phantom and across the fracture gap.

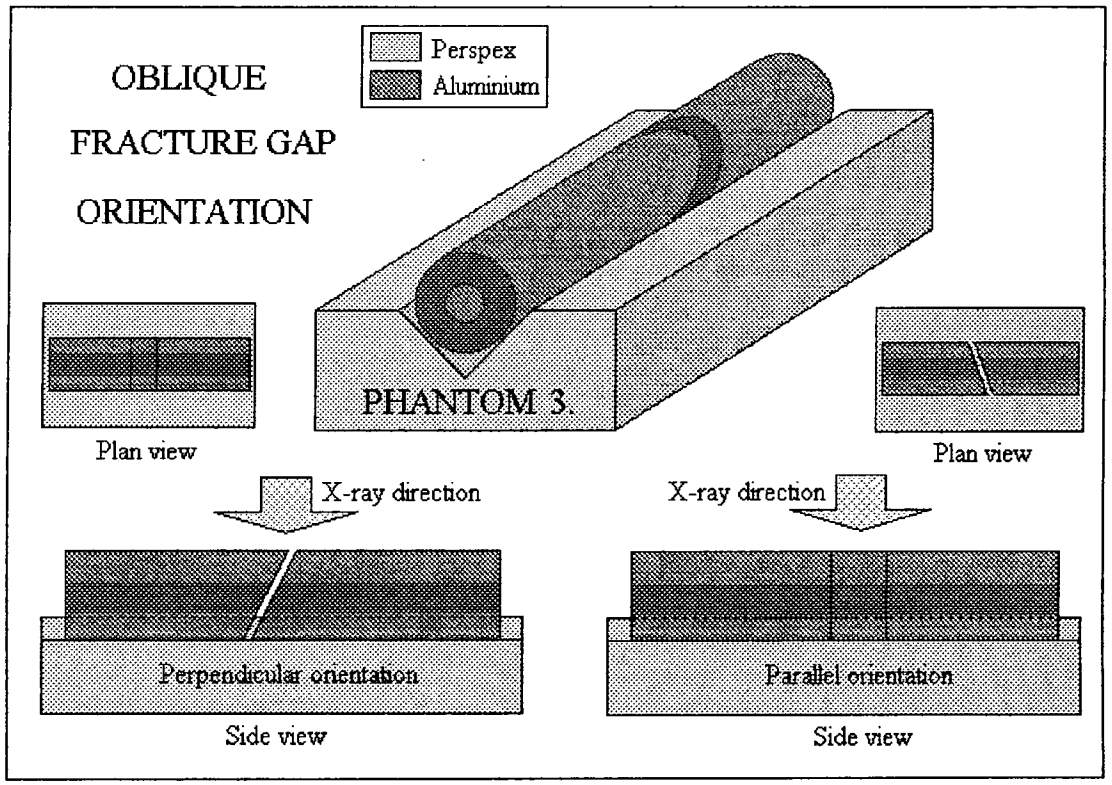

Figure 2.9. Diagram of the oblique fracture phantom 3. The phantom was positioned such that the fracture gap was orientated both parallel and nearly perpendicular to the path of the x-ray beam.

The results of analysing the oblique fracture gap, located parallel to the x-ray beam are shown in Figure 2.10. The line of the fracture was detectable on the computer monitor, hence the regions of interest could be easily located across the fracture gap. The experimental results clearly indicate the presence of a fracture gap. The standard deviation of results away from the fracture site is given in Figure 2.10. to demonstrate that the results for the fracture site are not within the normal range of values observed.

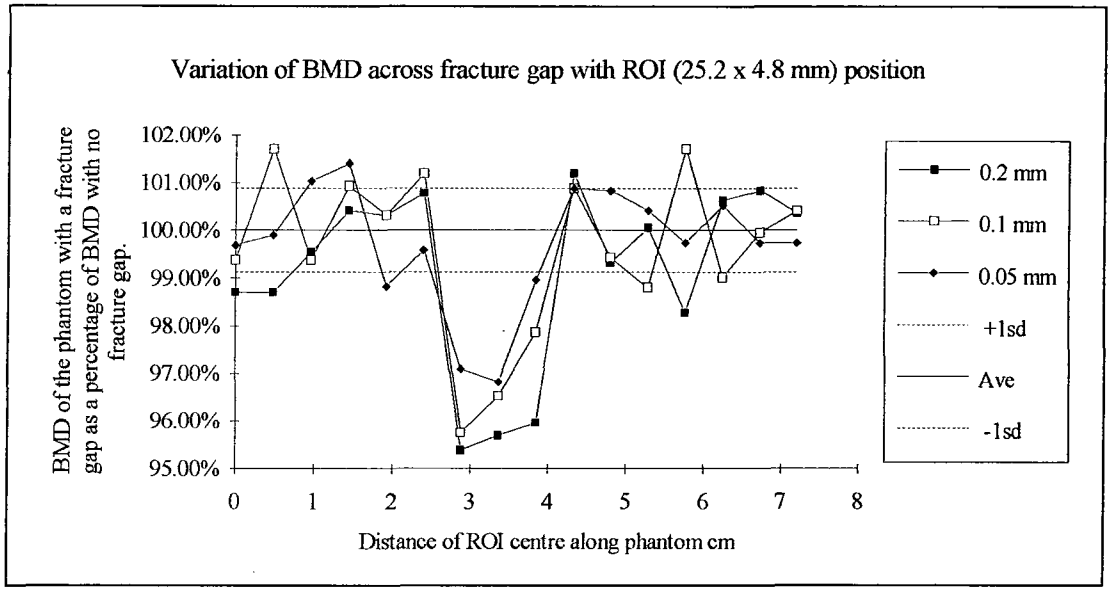

Figure 2.10. A graph showing the detection of an oblique fracture gap in an aluminium and perspex phantom, with an ROI 25.2 mm by 4.8 mm. The fracture gap was orientated parallel to the x-ray beam.

When the phantom was rotated about 90° so that the gap was almost perpendicular to the x-ray beam, the fracture gap was not discernible upon the image displayed on the computer monitor. However, regions of interest were placed along the length of the aluminium phantom, adjacent to each other to analyse the BMD results and assess whether the gap could be detected in this manner. The results are shown in Figure 2.11. The standard deviation of results away from the fracture site is given to demonstrate that the results for the fracture site are not within the normal range of values observed.

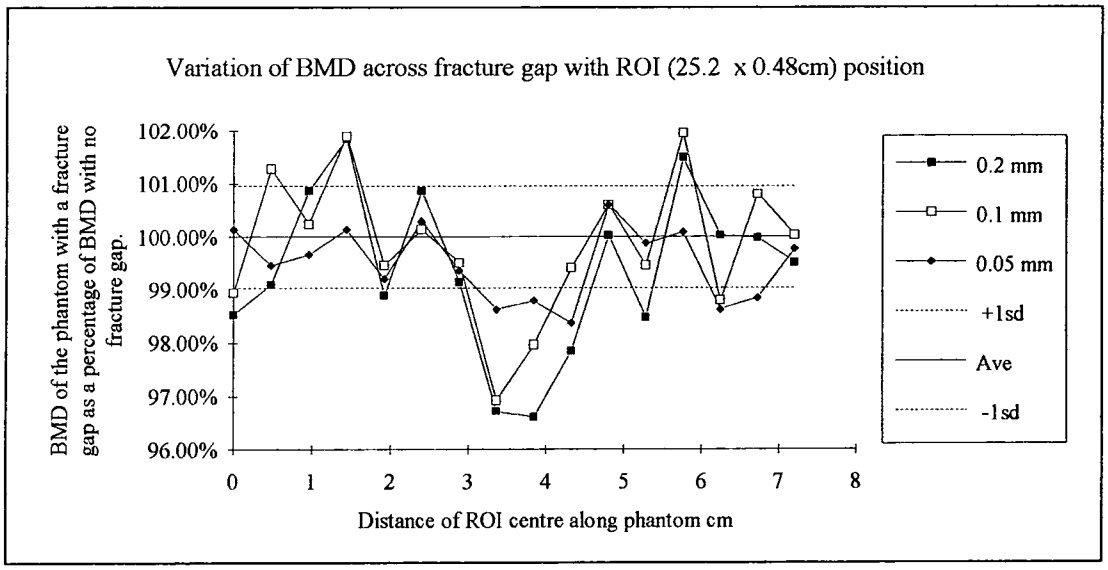

Figure 2.11. A graph showing the detection of an oblique fracture gap in an aluminium and perspex phantom, with an ROI 25.2 mm by 4.8 mm. The fracture gap is placed perpendicular to the x-ray beam.

The bone mineral density across the fracture gap in Figure 2.11. is significantly lower that the surrounding unfractured regions of aluminium, though to a lesser extent than the results shown in Figure 2.10. The difficulty with the orientation of the fracture gap perpendicular to the path of the x-ray is that it cannot be seen on the image displayed on the computer monitor during scanning. However, it could be potentially very useful to be able to detect a fracture gap which cannot be seen, but which can be measured by placing regions of interest along the length of the aluminium and analysing the BMD values.

The oblique fracture gap is quite clearly marked by a reduction of BMD in the experimental results for both orientations. When the same phantom is analysed theoretically to determine the expected magnitude of the BMD values, depending on the location of the region of interest, it appears that the gap should not be so clearly discernible (Figure 2.12.). The theoretical BMD was derived by first calculating the BMD for a region of interest across an unfractured portion of the phantom, then by calculating the percentage reduction in BMD for a similar ROI but this time located

across an oblique fracture gap. The theory derived for the oblique fracture gap is valid for any orientation of the aluminium about its longitudinal axis. It dose not take into account any variation caused by imperfect photon behaviour such as scattering.

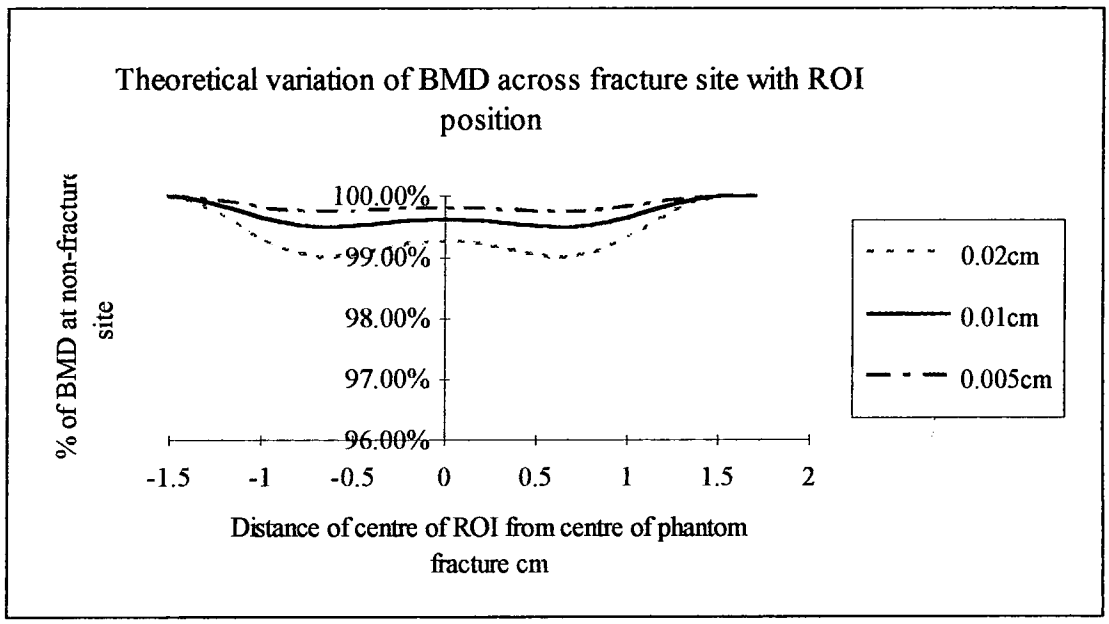

Figure 2.12. A graph of the theoretical variation of BMD for an aluminium and perspex phantom with an oblique fracture gap of width 0.02 cm, 0.01 cm and 0.005 cm. The analysis was carried out using a region of interest of dimensions 25.2 mm by 4.8 mm. The results are expressed as a percentage of the maximum BMD, *i.e.* the BMD at a non-fractured site.

Figure 2.12. shows that in theory, for the fracture gaps analysed, the percentage reduction of bone mineral density in a region of interest should not produce BMD values less than 99 % of the maximum unfractured BMD. If the reduction of BMD is within 99 %, fracture gaps would not be detectable and would fall into an experimental error region of 1 standard deviation. However, the experimental results clearly show that an oblique fracture gap is significantly detectable, with bone mineral density values of less than 96 % in some instances. The fact that the DXA scanner may appear more sensitive than expected for detecting oblique fractures is a useful attribute, as very small fracture defects may become detectable even if they are perpendicular to the x-ray beam.

2.2.5 Low Density

The 28 calcium hydroxyapatite specimens were scanned 5 times each, both with a soft tissue substitute of perspex and also a 35 mm thickness of water in a water tank above them. The bone mineral content output from the DXA scanner was plotted against the mass of the sample measured before and after the tests in the laboratory. (Figure 2.13.).

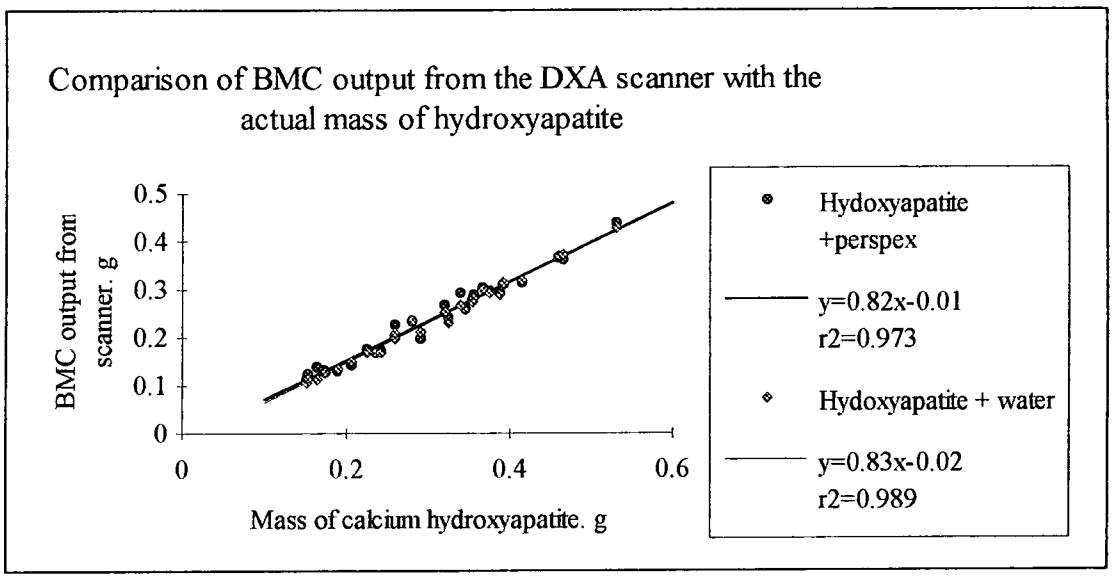

Figure 2.13. Comparison between the actual mass of calcium hydroxyapatite and the bone mineral content values given for the scanner. The best-fit linear equations are given for each set of data points. The actual mass of hydroxyapatite is denoted by x and the bone mineral content output from the scanner is denoted by y.

The actual mass and the bone mineral content as measured by the DXA machine, are well correlated (Figure 2.13.). A linear equation was fitted to each data series using the least squares method. The linear relationship between the phantom measurements and scanner results is valid for quantities as small as 0.15 g of hydroxyapatite. There was a negligible difference between the measurements made using the perspex base as a soft tissue substitute, when compared to the scan using a 35 mm thickness of water.

The bone mineral content is a measure of the mass of bone mineral present in a particular region of interest, its value depends on the size of ROI used. However, when monitoring a patient's tibia it is useful to be able to compare values at different sites along the length of the bone, independent of the geometry of ROI utilised. A measurement of bone mineral density (BMD) allows these comparisons to be made. Hence, the hydroxyapatite samples were used to compare the BMD output from the scanner with the calculated area density for the same sized region of interest. The results are shown in Figure 2.14.

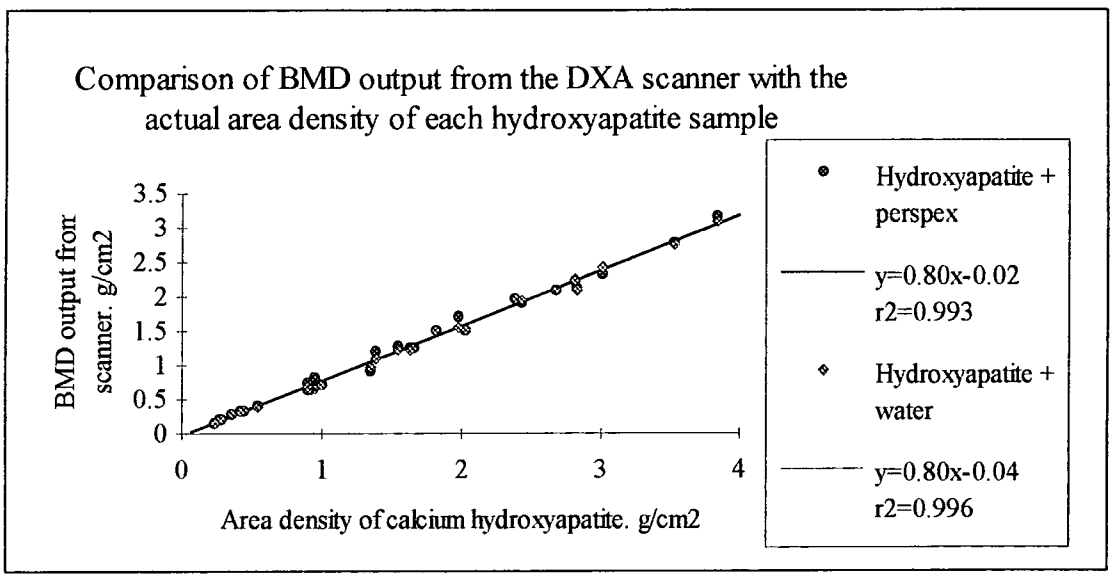

Figure 2.14. Comparison between the actual area density of calcium hydroxyapatite and the bone mineral density values given for the scanner. The best-fit linear equations are given for each series of data points.

The area density of a hydroxyapatite specimen is proportional to the thickness of the sample. The average density of the samples was 968 kg m^{-3} ± 26.23 kg m^{-3} (average ± standard deviation). To produce a range of bone mineral densities from approximately 0.2 g cm^{-2} to 3.9 g cm^{-2}, the specimens were varied in thickness using the equation BMD $=\rho * t$, where the material density is denoted by ρ and the thickness of the sample is given by t. There was an excellent linear correlation between the calculated

area density and the bone mineral density measured by the machine, with coefficients of determination of $r^2 = 0.993$ and $r^2 = 0.996$, for the tests carried out on phantoms using perspex and water as soft tissue substitutes respectively. The machine was able to accurately detect small bone mineral densities, giving valid results as low as 0.16 g cm^{-2}. Normal bone mineral density values of a healthy adult tibia, studied during patient trials, were usually between 0.9 g cm^{-2} and 1.8 g cm^{-2}. The phantom trials were capable of monitoring much lower bone mineral densities. Therefore it would appear that the DXA scanner can give reliable data in regions of low bone mineral density, which one might expect at a fracture site.

2.3 Summary

Using an aluminium and perspex phantom to simulate a fractured tibia it was shown that the optimum size of ROI for use during patient analysis had dimensions equivalent to the width of the tibia and a length of 4.8 mm, giving a coefficient of variation of less than 1.5 % and a standard deviation of results of 0.03 g cm^{-2}. To analyse a patient tibia would require about 30 to 40 ROIs of this size. In addition it was shown that the occasional use of a polythene board by the radiographers to improve the scan image of a patient's fractured tibia, would have a negligible effect upon the BMD results. The reproducibility of results for the aluminium and perspex phantom was good with a coefficient of variation of 1.1 %.

The DXA machine was sensitive to small fracture gaps created in the aluminium and perspex phantom. Although the fracture site was not always visible on the scan image, it was possible to detect a reduction of BMD across a simple transverse fracture gap of less than 0.05 mm and also an oblique fracture gap of the same size, regardless of its orientation about the longitudinal axis.

Using calcium hydroxyapatite specimens it was shown that the machine was capable of measuring bone mineral in small areas of low density. The minimum BMD measured was 0.16 g cm^{-2}. The normal range of BMD in a healthy tibia is between 0.9 g cm^{-2} and 1.8 g cm^{-2}, so it would appear that the DXA scanner is able to accurately measure the areas of low bone mineral densities which one might expect at a fracture site.

The relationship between the actual area density of a bone substitute material and the experimental BMD output by the scanner was linear, which made it possible to assess relative changes in the area density of the phantom without needing to convert each output value to its true value. The scanner is programmed to expect bone and soft tissue, not the substitute materials, hence by using the derived experimental relationships between area density and the scanner BMD output, it is possible to obtain accurate BMD values for the bone phantom.

CHAPTER 3
Patient Trials

3.1 Patients and Methodology

16 Patients with a fracture of the tibia, were referred to South Cleveland Hospital, Middlesbrough, U.K. from October 1992 to September 1993, and participated in the fracture healing study. Only patients with intramedullary nails or external fixators were admitted to the study; alternative fracture management methods, such as plaster casts and internal plating were excluded from the trials. Of the 16 patients initially recruited, two subsequently failed to attend more than one densitometry scan and were therefore lost to follow up.

3.1.1 Patients

14 Patients were included in the fracture healing study. The age of the participants ranged between 22 and 72, with an average age of 33.4. Nine of the patients were under 30 years of age. Details of the fracture types and method of fixation used in all 14 patients are shown in Table 3.1.

Details of Patients involved with the fracture healing study.		
		Number
Bones fractured		
	Fractures of the tibia and fibula	8
	Fracture of the tibia only	6
Type of fracture		
	Transverse	2
	Oblique	3
	Spiral	7
	Comminuted	2
Fixation method		
	Intramedullary nail	6
	External fixator	8
Fracture location		
	Upper third	1
	Mid shaft	11
	Lower third	2

Table 3.1. Details of the type, location and fixation method used for 14 patients with tibial fractures.

Four of the patients were female and 8 were male. The data collected for each patient included personal details such as height and weight. Any special information relating to a particular patient, for example a change of fracture management technique, will be detailed in the results section. Patients were requested to have their first scan taken within 14 days of the fracture occurring. However, in practice the date of the first scan for the patients involved in the fracture healing study ranged between 5 and 25 days post-fracture. Subsequent scans occurred at 4 to 6 week intervals thereafter. Typically each patient attended for a densitometry scan on 4 different occasions. The patients were numbered from 1 to 14 to maintain patient confidentiality.

3.1.2 Scanner

All scans were performed on a Lunar DPX-L scanner. The Lunar forearm software and the Lunar orthopaedic software were used to acquire and analyse the data. 8 Patients were scanned using the forearm software, 4 were scanned using the orthopaedic software and 2 patients were scanned using both types of software. The

Lunar software required certain data acquisition levels to be set and these were kept constant for each patient. The fast scan mode was used, the smallest sample setting selected giving a pixel size of 0.6 mm by 1.2 mm and the sample interval was set at 1/64 s. The time taken for a single scan was between 12 and 15 minutes depending on the length of tibia scanned.

Two software packages called the Lunar orthopaedic software and the Lunar forearm software, were initially used with the scanner in order to collect data for this study. The Lunar forearm software had been designed to monitor bone changes in the distal radius and had been intended to study fracture risk at this site and the effect of certain diseases such as diabetes on bone loss. The software algorithms detect the interface between soft tissue and bone and then locate regions of interest to measure the bone mineral content (BMC) and the bone mineral density (BMD) in specific areas of the radius and ulna. The forearm software also has the facility to carry out manual analysis, where the operator is able to locate a region of interest (ROI) of any size, at any position of the scan.

The Lunar orthopaedic software was designed to monitor changes in bone mineral of the proximal femur adjacent to prosthetic implants. Algorithms automatically detect the interfaces between bone, implant material and soft tissue and a reproducible origin point is identified at the extreme medial border of the lesser trochanter and positions 4 regions of interest (ROI) based on this co-ordinate system. The measured bone mineral content (BMC) for a ROI is divided by the projected area of the ROI and therefore gives the bone mineral density (BMD) in units of g cm^{-1}. The orthopaedic software also has the facility for manual analysis which enables an ROI of any size and shape to be located in any chosen position.

During the early scans of patients, it was found that the orthopaedic software did not give satisfactory results when trying to analyse data. Further details will be given in Section 3.2.1 of the problems which occurred when using this software. Consequently the majority of the fracture healing results were analysed using the forearm software.

3.1.3 Analysis

Patients were positioned upon the scan table and the limb being scanned was held in position by securing the foot to a foot board. The x-ray beams passed posterior to anterior, enabling an unobscured scan of both the tibia and fibula to be obtained. Depending upon the clarity of the scan image which appeared on the computer monitor, the patients limb may have been scanned with the addition of a polythene board to improve the quality of the image produced. During phantom trials the addition of a polythene board appeared to make no difference to the BMD values output on the scanner (Section 2.2.1). The starting position of the x-ray beam was located by the use of anatomical landmarks, such as the entry point in the skin of a fixator screw. Whenever possible the non-fractured contra-lateral leg was scanned at the same time as the fractured limb.

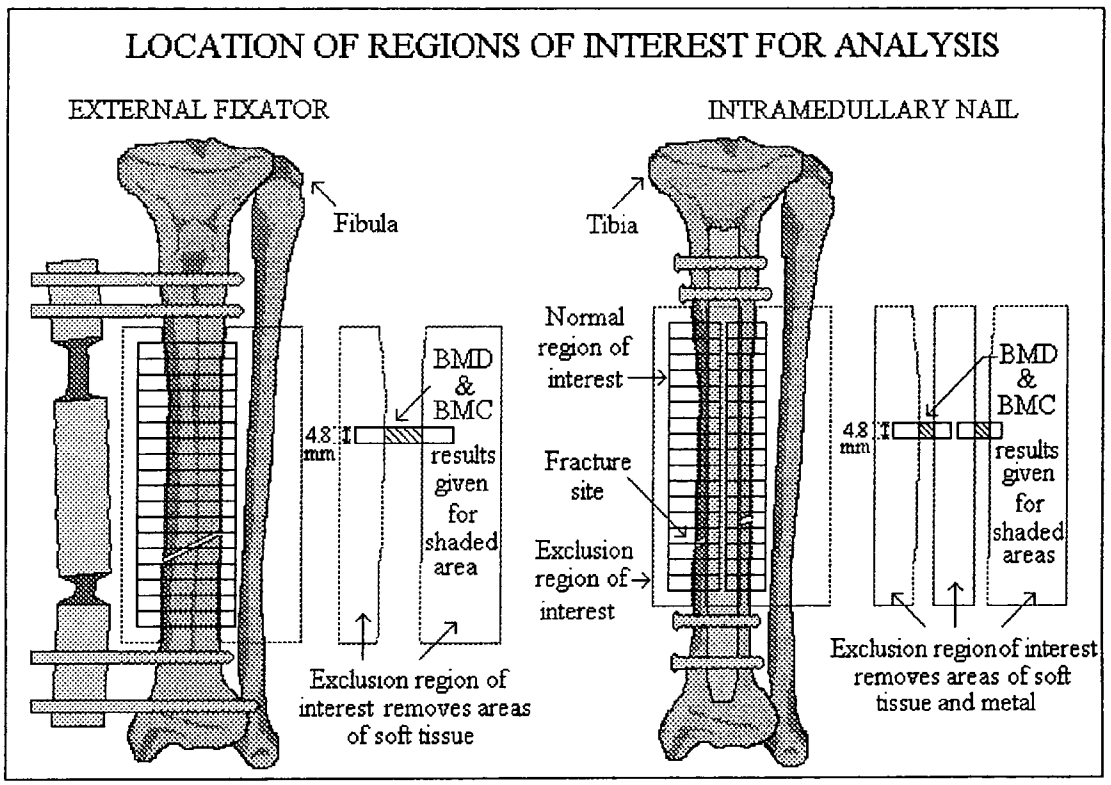

Figure 3.1. Schematic representation of a fractured tibia. The positioning of the regions of interest is shown. Exclusion regions of interest are used to remove soft tissue and metal from the areas of interest, allowing just bone mineral content (BMC) and bone mineral density (BMD) to be measured.

The patient data was analysed by using the manual analysis option on the Lunar software. Regions of interest (ROIs) were located adjacent to each other, along the length of the tibia (Figure 3.1.). Exclusions regions of interest were used to remove areas containing soft tissue and metal from the analysed regions of interest. One exclusion ROI was placed along each side of the tibia and if an intramedullary nail was present, an exclusion ROI was also located over the nail. The normal regions of interest were 4.8 mm long and covered the width of the tibia. In the case of patients with internal fixation, the medial and lateral sides of the tibia were measured separately. The bone mineral data collected for each patient was analysed using a database and statistical computer package (Microsoft® Excel for Windows™). The BMD results for each patient were plotted on a graph to display the change in BMD along the length of the tibia with each scan, the x-axis giving the position of the region

of interest along the tibial shaft in the proximal to distal direction and the y-axis giving the BMD for the region of interest.

3.2 Results

3.2.1 Lunar software

6 Patients were initially scanned using the Lunar orthopaedic software. However, many problems were experienced using this software both at the time of scanning and during analysis of the data. These problems are described below.

Whilst the patient was being scanned, the image displayed on the computer screen was not clear and the outline of the tibia and fibula could not be discerned. A variety of packing materials were introduced to surround the patients leg, including a polythene board and bags of rice as recommended by the manufacturer of the scanner (Lunar). However, the x-ray beam did not appear sufficiently attenuated to produce a clear picture. This is probably due to the orthopaedic software being designed for scanning the proximal femur, where the thickness of the soft tissue present at the proximal femur is significantly greater than that at the tibia. The lack of a clear image made repositioning the limb between scans difficult to monitor.

The image displayed on the computer monitor in the analysis mode was better than that displayed during the scanning mode and was sufficient to locate regions of interest adjacent to each other along the length of the tibia as described in Section 3.1.3. However, problems did occur with the computer crashing regularly during analysis, with a run time error. Results for every patient scanned using the orthopaedic software showed erratic BMD results. For example one patient with an intramedullary nail gave readings of bone mineral density for the first month of about 11 g cm^{-2}, the following month readings of about 4 g cm^{-2} were obtained and subsequent scan

readings varied between 2 g cm^{-2} and 7 g cm^{-2} (Figure 3.2.). For a normal, unfractured tibia BMD values have been reported of about 0.9 g cm^{-2} (Eyres *et al.*, 1993 (a)). All of the other patients scanned using the orthopaedic software produced similarly erratic results.

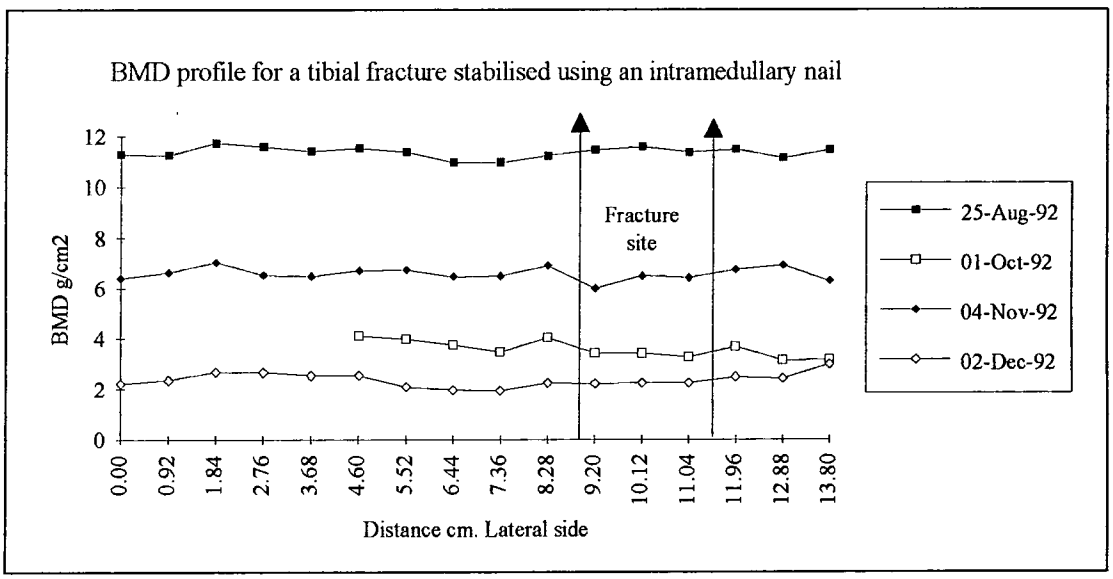

Figure 3.2. BMD profile for Patient 12 treated with an intramedullary nail and analysed using the Lunar orthopaedic software.

Different analysis techniques were tried, such as including the metal in regions of interest, but this did not improve the results. It would appear that these erratic results are due to an intrinsic error caused by the software, whilst scanning a non-standard application. Consequently the subsequent patient analysis was carried out using only the forearm software.

3.2.2 Reproducibility

To obtain the reproducibility of results, Patient 1 had his fractured tibia scanned 3 times, using the forearm software, during one visit. The patient was moved from the densitometry table and repositioned between each scan. Regions of interest were placed adjacent to each other along the length of the tibia as previously described and

the bone mineral density results analysed. The results for each scan, for each location of a region of interest, were compared to obtain an indication of the reproducibility of the results and the standard deviation of a bone mineral density reading. For the 37 ROIs placed along the length of the tibia, an average coefficient of variation of 3.36 % was obtained, with a maximum coefficient of variation of 8.15 % and a minimum of 0.82 % (Figure 3.3.). The coefficient of variation is greater at higher values of BMD due to the larger standard deviation of the higher BMD results. Good reproducibility of results was also obtained.

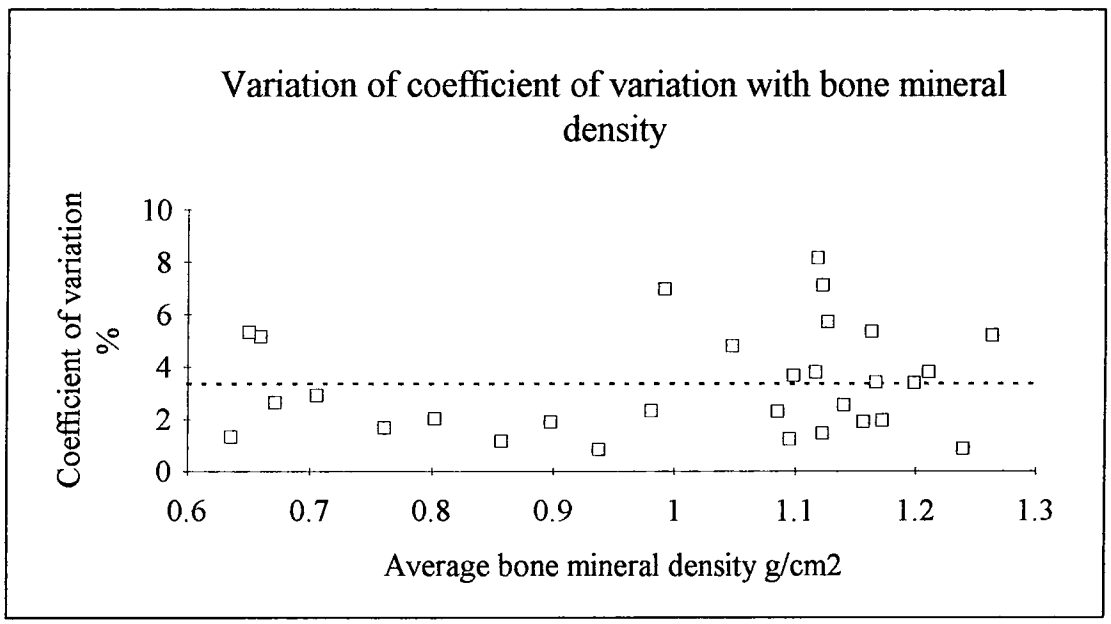

Figure 3.3. Graph showing the coefficient of variation versus the bone mineral density obtained from the repeated scanning of a patient's fractured tibia.

The average standard deviation obtained from the bone mineral density results was 0.03 g cm^{-2}, with a maximum of 0.09 g cm^{-2} and a minimum of 0.01 g cm^{-2}. It would appear from Figure 3.4. that the standard deviation of the results for the patient analysed, was typically smaller in regions of low bone mineral density, than at bone mineral density values of above 1 g cm^{-2}.

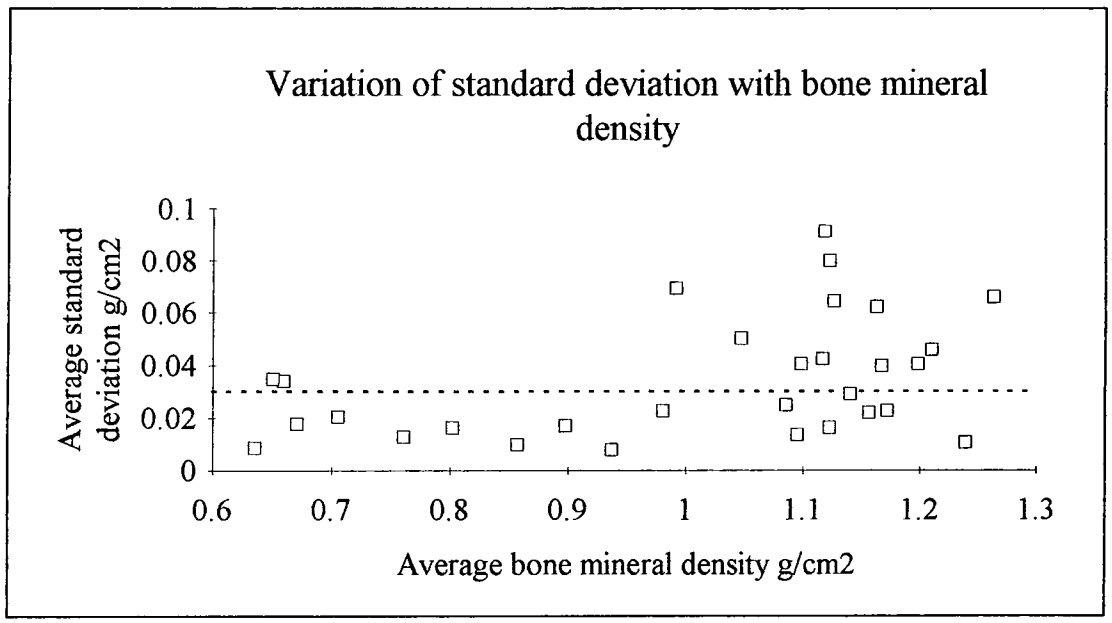

Figure 3.4. Graph showing the variation of the standard deviation against the bone mineral density obtained from the repeated scanning of one fractured patient tibia.

Three patients on at least 3 different dates, had their healthy contra-lateral leg scanned at the same time as their fractured limb was scanned. By analysing these results, it was possible to obtain a measure of the long term reproducibility of the results. Regions of interest were placed adjacent to each other along the length of the healthy limb and the bone mineral density values obtained for each region of interest compared between scans. The standard deviation and the coefficient of variation for each region of interest was calculated and the average results are shown in Table 3.2.

Reproducibility of BMD results, with time for the unfractured tibia of three patients.				
Patient Number	Standard deviation g cm^{-2}	Coefficient of variation %	Number of scans	Time between first and last scan
3	0.03	3.39	3	11 weeks 3 days
4	0.08	5.64	4	13 weeks 4 days
9	0.04	3.37	5	19 weeks 4 days
Average	0.05	4.13	4	~15 weeks

Table 3.2. Table of the average standard deviation and coefficient of variation for the repeated scanning of 3 patients' unfractured tibias.

3.2.3 Healthy Non-fractured Limb

When the bone mineral profile for the unfractured limb of the three patients was plotted on a graph, there appeared to be no change in the bone mineral profiles obtained between each scan, an example is shown for Patient 9 in Figure 3.5. Studies of the healthy contra-lateral leg of patients with tibial fractures, have shown that no significant changes occur in the bone mineral density of the healthy limb with time (Ulivieri *et al.*, 1990). Sarangi *et al.* (1993) demonstrated that for patients with fractures of the tibial shaft, there was no significant change in BMD of the uninjured leg, from the time of injury to the time of union. Since there appears to be little variation of the healthy leg with time, it would appear reasonable to assume that any scan of the healthy limb, made throughout the duration of the fracture healing study for a particular patient, would give an accurate representation of the BMD profile of the healthy tibia.

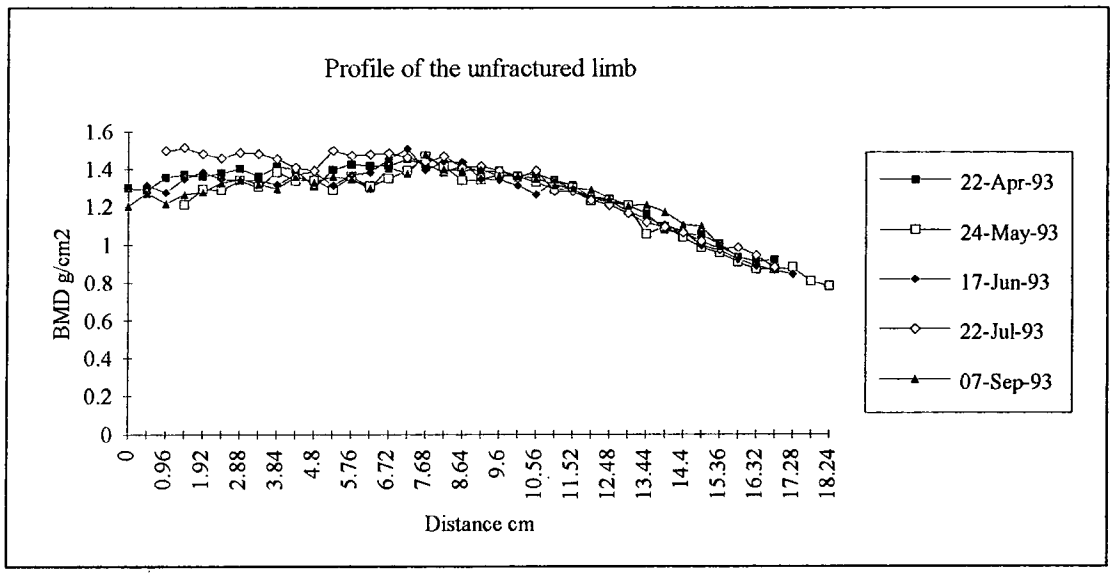

Figure 3.5. Bone mineral density profiles of the healthy, unfractured tibia for Patient 9.

Previous studies have also shown that although there is much variation in BMD between subjects at the same site in a bone (Carter *et al.*, 1992), there is no significant difference between similar locations in both legs for a particular individual (Sarangi *et al.*, 1993). Therefore by comparing the fractured tibia with the contra-lateral tibia, an assessment can be made regarding the progression of the fractured limb towards a normal BMD profile. Since the BMD of the healthy limb does not significantly vary with time, comparison between the BMD of the fractured and unfractured limb could be made, as long as at least one scan of the healthy unfractured tibia had been taken during the fracture healing study.

3.2.4 External Fixation

The bone mineral density (BMD) profiles obtained for Patients 1, 3, 4, 6, 9 and 10, with tibial fractures stabilised using external fixators are given in this section. These patients all exhibited uncomplicated fracture healing. An example of the computer display produced during analysis of the scan using the Lunar forearm software, for a patient with an external fixator is given in Figure 3.6. The standard regions of interest

are shown by the red rectangles placed along the length of the tibia and the cyan boxes are the exclusion regions of interest.

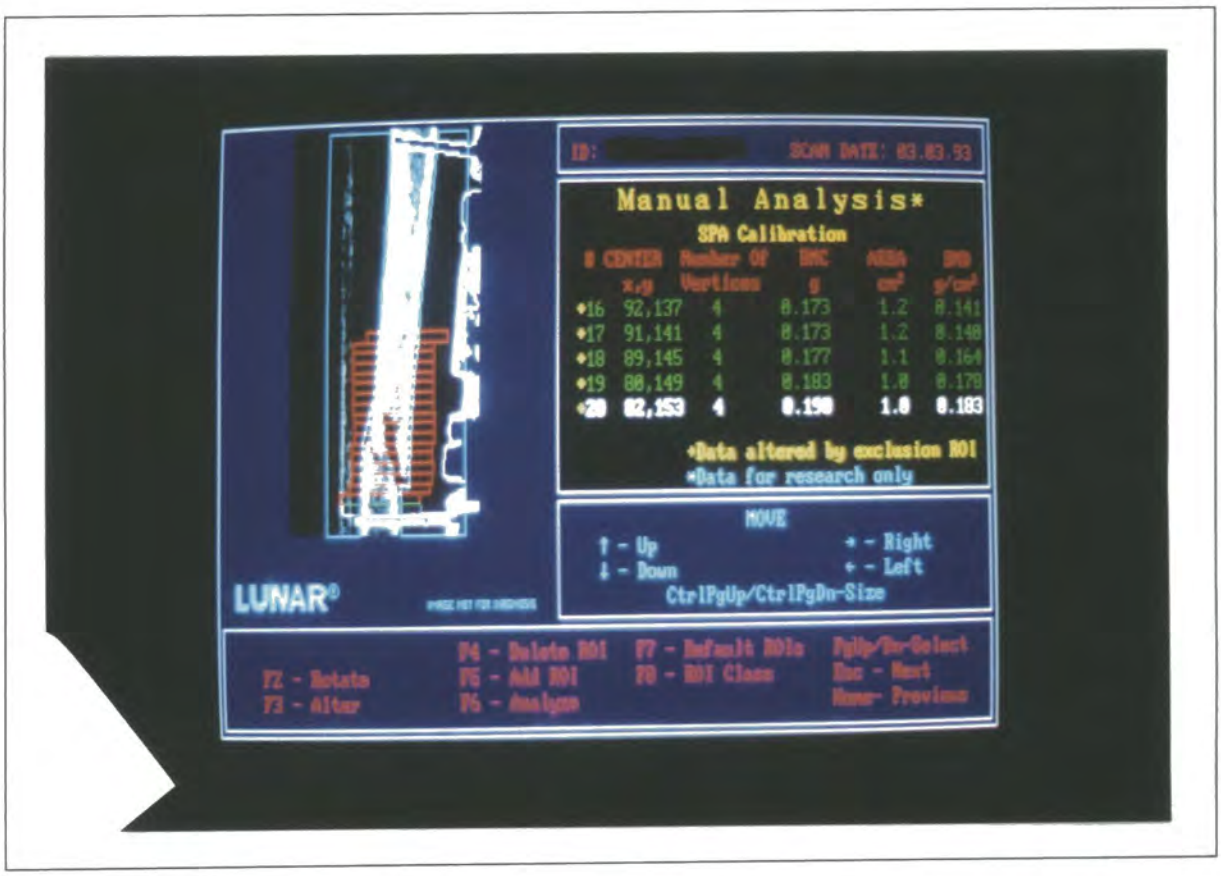

Figure 3.6. Lunar software computer display during analysis of Patient 3 with an external fixator.

Patient 1

The first scan for Patient 1 was taken 8 days post-fracture (Figure 3.7). No scan of the contra-lateral limb was performed for this patient. X-rays of the patient on the day of the fracture and after the external fixator had been applied, are shown in Figure 3.8. and Figure 3.9. respectively, on which the fracture gap is clearly visible.

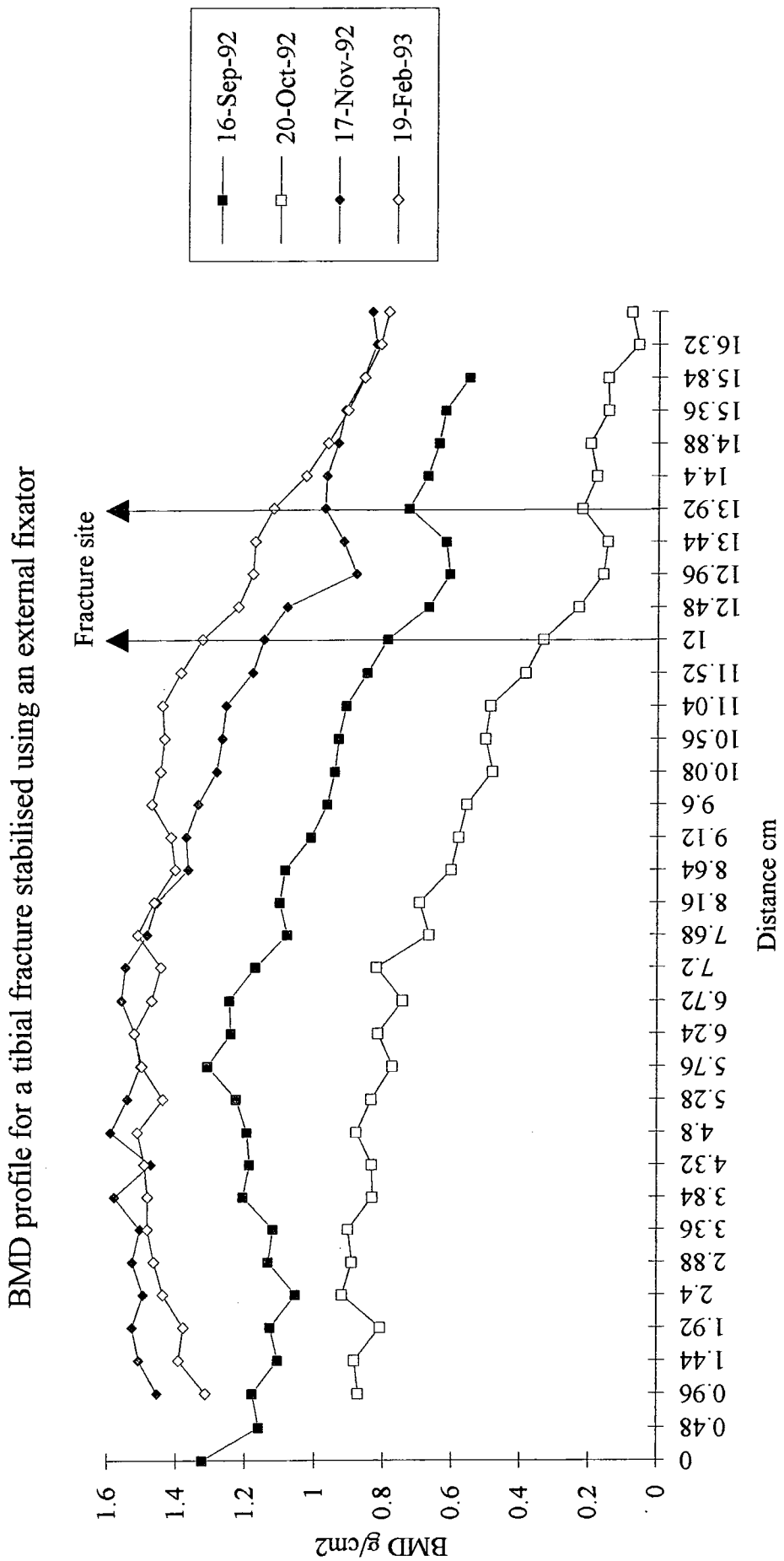

Figure 3.7. BMD profile for Patient 1 with a mid shaft spiral fracture. The fixator was removed after the scan in November. The date of the fracture was 8-Sep-92.

Figure 3.8. X-ray of Patient 1 showing the anterior-posterior view and the medial-lateral view of the fractured tibia before fixation. 8-Sep-92.

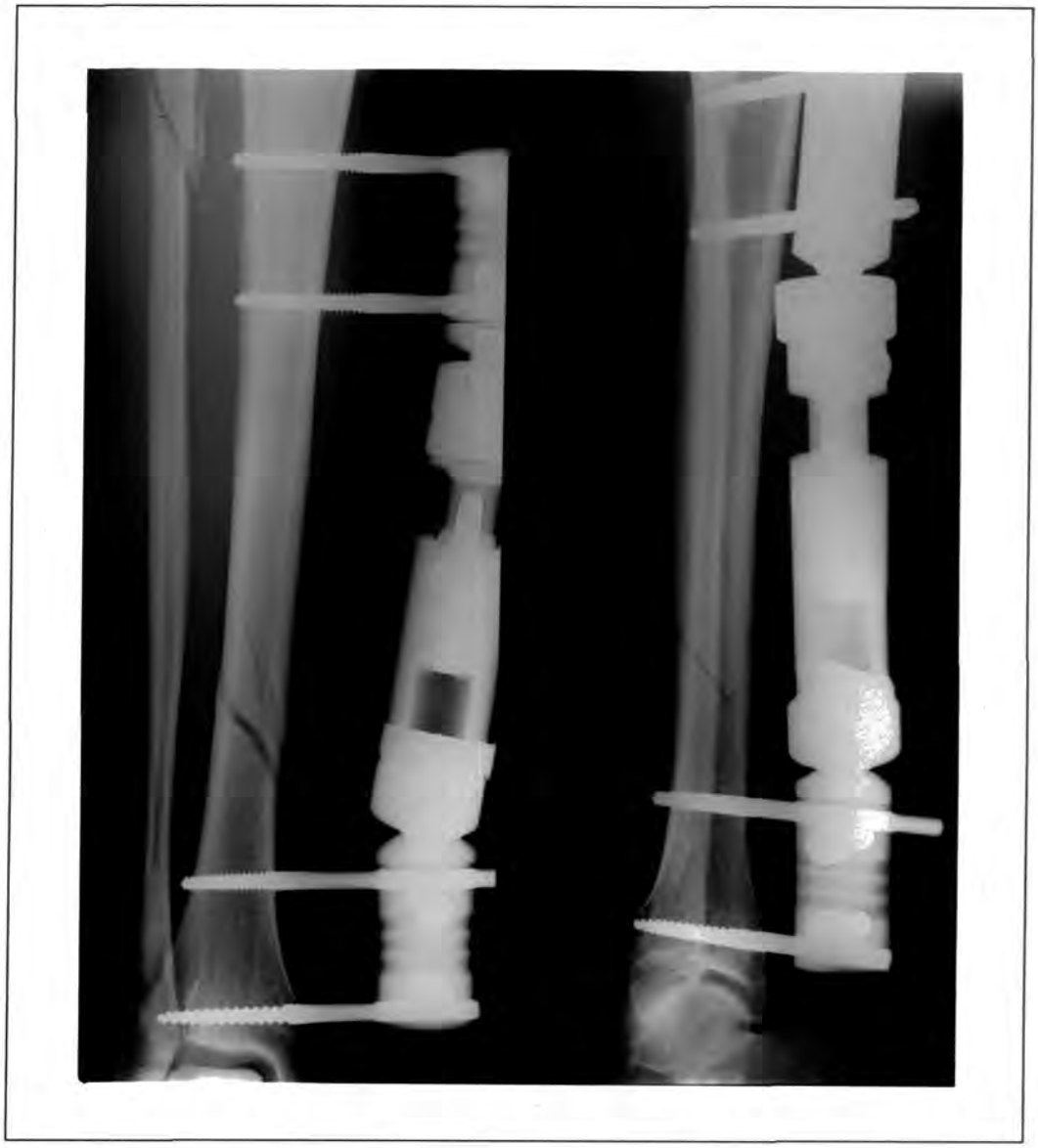

Figure 3.9. X-ray of Patient 1 showing the anterior-posterior view and the medial-lateral view of the fractured tibia after fixation. 9-Sep-92.

The scan taken of this patient in February, 24 weeks post fracture, shows negligible variation in BMD in regions distant to the site of the fracture, when compared to the BMD values obtained in November. Consequently it was used to give an indication of the profile of a healthy tibia by which to compare the other scans taken for this patient. The percentage change for each scan when compared to the scan taken 24 weeks post fracture is given in Table 3.3.

% BMD compared to an equivalent region of interest on 19-Feb-93. (Average ± 1 Standard deviation)				
Regions of interest.		16-Sep-92	20-Oct-92	17-Nov-92
Distant to the fracture site.	0.0 - 9.12 cm	79.6 ± 5.2 %	55.0 ± 7.4 %	101.5 ± 4.5 %
Near to the fracture site.	9.6 -11.52 cm 14.4 - 15.84 cm	64.9 ± 2.1 %	26.6 ± 8.7 %	92.5 ± 5.8 %
Across the fracture site.	12.0 - 13.92 cm	56.7 ± 5.5 %	18.1 ± 5.1 %	82.9 ± 6.1 %

Table 3.3. The BMD values along the fractured tibia of Patient 1 expressed as a percentage of the BMD values obtained at the same location on 19-Feb-93.

The bone mineral density along the length of the tibia had already reduced at 8 days post-fracture when compared to the February results. There was a gradual reduction in BMD along the length of the fractured tibia, which continued until the measurements obtained on 20-Oct-92, 6 weeks post-fracture. The most significant decrease was seen across the fracture site, with a BMD value of 18.1 % of the same location on the February scan. Bone necrosis and resorption of the fractured bone ends may be the largest contributory factor for this reduction in BMD. The fixator was removed after the scan in November, when the BMD recorded along the length of the bone had greatly increased. The fracture site was still clearly visible on the DXA scan, but had mineralised to 82.9 % of the BMD obtained at the same site nearly 14 weeks later. When examining the x-rays taken on the 26-Jan-93, the location of the fracture and some external callus formation can be seen (Figure 3.10.). The BMD profile taken on 19-Feb-92 exhibited a normal BMD profile and the location of the fracture site was not obvious. In general the extent of bone loss was lower at the regions of interest distant from the fracture site.

Figure 3.10. X-ray of Patient 1 showing the anterior-posterior view and the medial-lateral view of the fractured tibia after removal of the fixator. 26-Jan-93.

Patient 3

Scans of the healthy contra-lateral limb for Patient 3 (Figure 3.11.) were obtained and were used as a control to compare with scans of the fractured limb. The first scan was performed 13 days post-fracture and showed a marked decrease in bone mineral density along the length of the fractured tibia. At the fracture site the bone mineral density was 21.3 % of the equivalent region in the control tibia (Table 3.4.). However, by the second and third scans, at about 6 and 10 weeks post-fracture respectively, the BMD distant to the fracture site had nearly returned to its pre-fracture level, while at the site of the fracture there was still a marked deficit of BMD compared to the healthy limb. As can be seen in Table 3.4. the bone mineral density at the fracture site, following removal of the fixator on 3-Jun-93, at 15 weeks post-fracture, was greater than the control value. This may be a result of the presence of the fracture callus.

% BMD compared to an equivalent region of interest on the unfractured limb. (Average ± 1 Standard deviation)						
Regions of interest.		3-Mar-93	31-Mar-93	27-Apr-93	3-Jun-93	16-Jul-93
Distant to the fracture site.	0.0 - 8.16 cm	42.9 ± 4.2 %	94.8 ± 4.1 %	95.5 ± 4.9 %	103.6 ± 6.1 %	104.3 ± 4.5 %
Near to the fracture site.	8.64 -11.04 cm 16.32 - 16.8 cm	37.5 ± 10.9 %	87.0 ± 8.0%	89.3 ± 7.0 %	101.8 ± 3.5 %	104.2 ± 3.6 %
Across the fracture site.	11.52 - 15.84 cm	21.3 ± 8.9 %	71.4 ± 6.2 %	81.1 ± 3.0 %	109.2 ± 6.1 %	122.8 ± 11.0 %

Table 3.4. The BMD values along the fractured tibia of Patient 3 expressed as a percentage of the BMD values obtained at an equivalent location on the healthy contra-lateral limb 16-Jul-93.

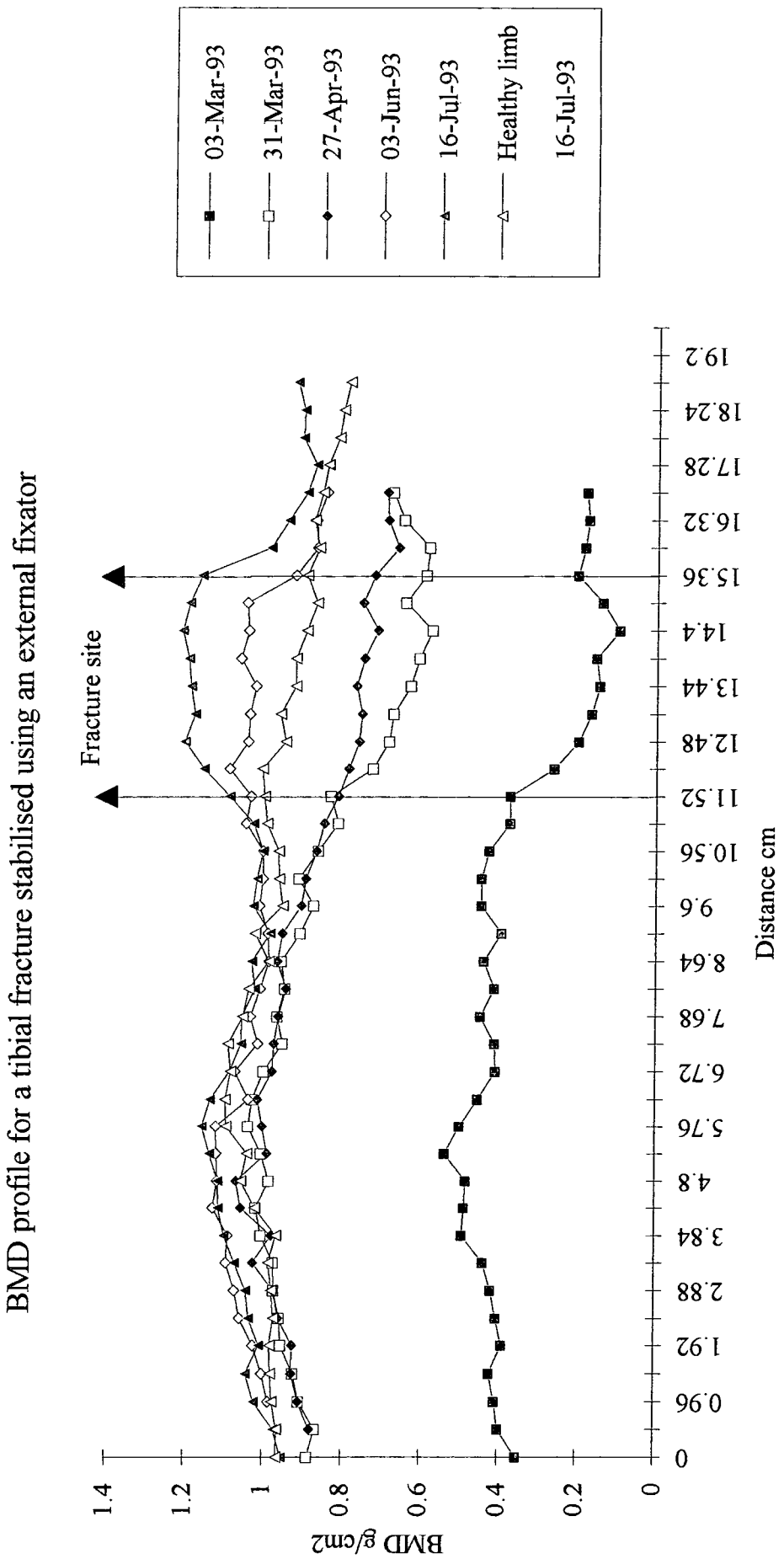

Figure 3.11. BMD profile for Patient 3 with a mid shaft spiral tibial fracture. The fixator was removed after the scan in June. The date of fracture was 18-Feb-93.

Patient 4

The contra-lateral limb for Patient 4 was used as a control for comparison with the BMD profiles obtained for the fractured tibia (Figure 3.12.). The fracture site was clearly seen on all of the DXA scans. Compared to the unfractured tibia the BMD across the fracture site 22 days post-fracture, was only 37.7 % of the equivalent position on the control limb, while the remainder of the diaphysis experienced an average BMD reduction of 53.1 % of the control tibia (Table 3.5.). However after the first scan there was a steady rise in the BMD along the length of the tibia, continuing to the time of the last scan at 13 weeks post-fracture, and reaching a value of 85.4 % of the control tibia. However, the fracture site was still clearly discernible on the last DXA scan taken in July. The BMD profile had not returned to normal and the BMD measured across the fracture site was 70.9 % of that of the control tibia.

% BMD compared to an equivalent region of interest on the unfractured limb. (Average ± 1 Standard deviation)				
Regions of interest.		21-May-93	22-Jun-93	27-Jul-93
Across the fracture site.	0.96 - 6.72 cm	37.7 ± 13.9 %	66.0 ± 13.9 %	70.9 ± 12.5 %
Near to the fracture site.	0.0 - 0.96 cm 6.72 - 16.32 cm	53.1 ± 5.0 %	79.2 ± 4.2 %	85.4 ± 4.6 %

Table 3.5. The BMD values along the fractured tibia of Patient 4 expressed as a percentage of the BMD values obtained at an equivalent location on the healthy contra-lateral limb 27-Jul-93.

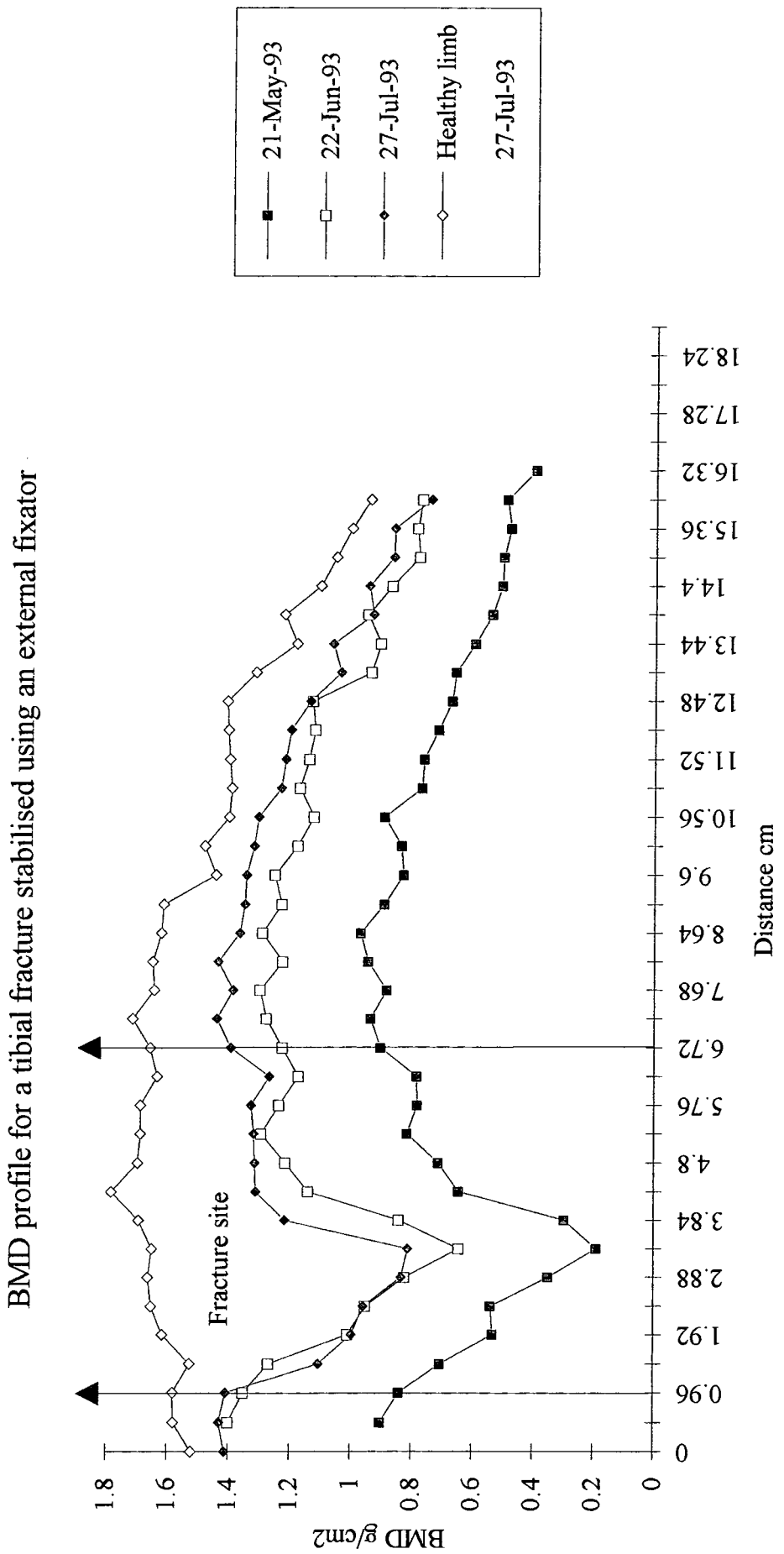

Figure 3.12. BMD profile for Patient 4 with a uni-cortical comminuted upper 1/3 tibial fracture. The date of fracture was 29-Apr-93.

Patient 6

Patient 6 had complications associated with the delayed union of the fracture and as a consequence the BMD profiles obtained for the fractured limb did not follow the trends exhibited by the other patients in this study.

This patient had a particularly complicated open fracture and experienced delayed union of the tibia which eventually required a bone graft. A scan of the healthy contra-lateral tibia was used to compare with the BMD profiles obtained for the fractured tibia (Figure 3.13.). Along the length of the tibia, away from the fracture site, the BMD fell to 58.3 % of the control values by the date of the first scan at 23 days post-fracture (Table 3.6.). By the second scan, at 8 weeks post-fracture, the BMD along the length of the fractured tibia was approaching that of the unfractured limb, with a value of 96.1 % of control values. Due to pin-tract infection the external fixator was changed for another model of external fixator after the scan in March. From the scan taken in April a decrease in the BMD along the tibia was observed with the measured BMD falling to 77.1 % of the control limb values. It remained at approximately this level for the following scan taken in May, at 17 weeks post-fracture.

% BMD compared to an equivalent region of interest on the unfractured limb. (Average ± 1 Standard deviation)					
Regions of interest.		11-Feb-93	16-Mar-93	20-Apr-93	18-May-93
Across the fracture site.	12.96 - 15.36 cm	35.1 ± 11.0 %	58.4 ± 2.6 %	47.2 ± 5.0 %	45.1 ± 2.8 %
Near to the fracture site.	2.88 - 12.48 cm	58.3 ± 3.3 %	96.1 ± 3.5 %	77.1 ± 4.8 %	77.9 ± 4.0 %

Table 3.6. The BMD values along the fractured tibia of Patient 6 expressed as a percentage of the BMD values obtained at an equivalent location on the healthy contra-lateral limb on 18-May-93.

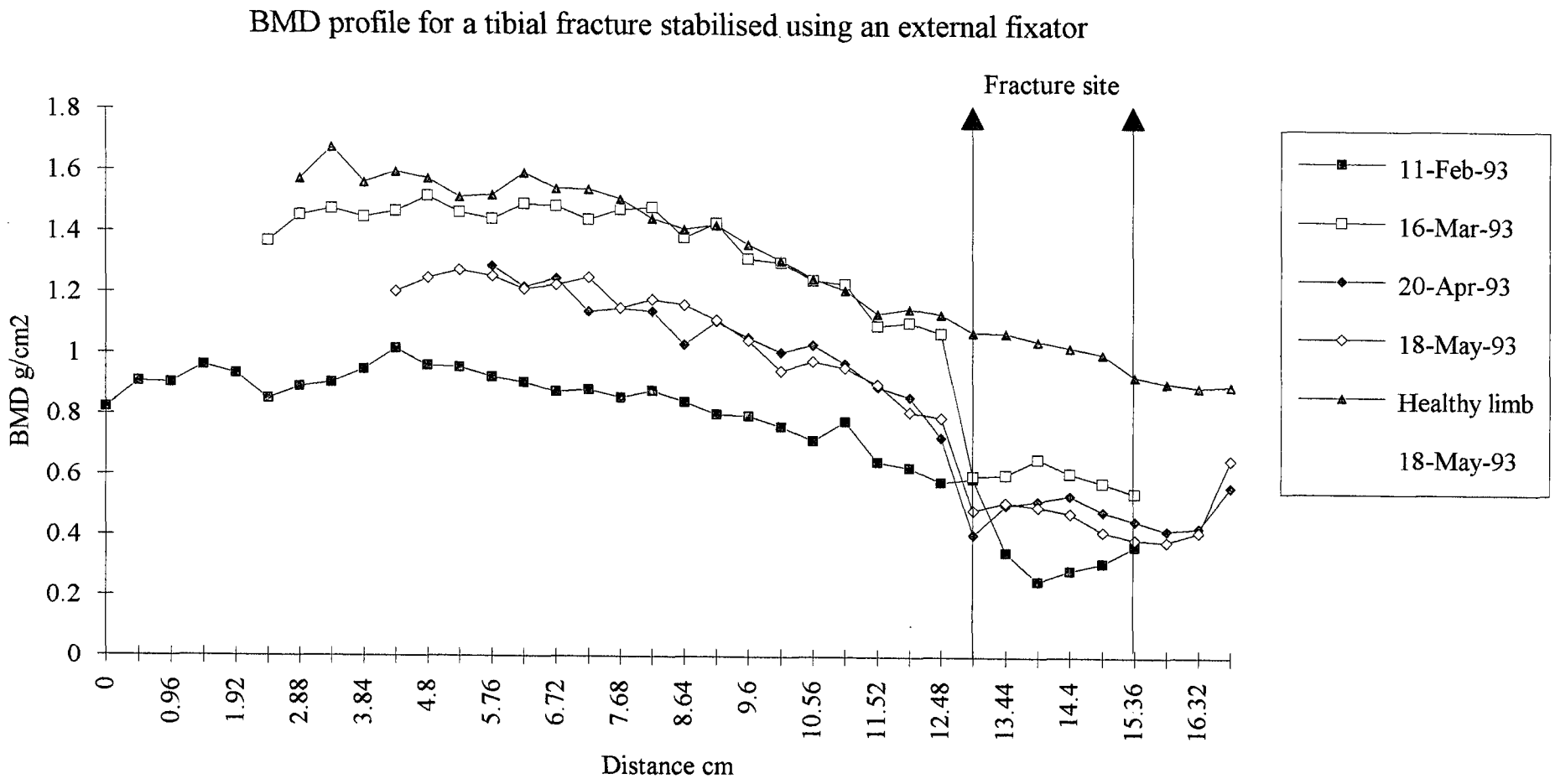

Figure 3.13. BMD profile for Patient 6 with a lower 1/3 transverse tibial fracture. The external fixator was changed on 16-Mar-93 and a bone graft performed following the last scan. The date of fracture was 19-Jan-93.

The fracture site was clearly visible on the DXA scan and the BMD profiles (Figure 3.13.). Across the fracture site the BMD was 35.1 % of that of the control limb by the date of the first scan, 23 days post-fracture. There was an increase to 58.4 % in March, but following the change of fixator the BMD fell to 47.2 %. It stayed at about 45 % for the last BMD measurement at 17 weeks post-fracture. The fracture gap was still clearly visible on the DXA scan and there was a significant difference in the extent of mineral present at the fracture site compared to the adjacent bone. A sharp fall of bone mineral at the area of the fracture site was observed on the BMD profile (Figure 3.13.) and the BMD values stayed fairly constant. Following the scan in May delayed union was diagnosed, patient had a bone graft and no further scans were obtained.

Patient 9

The first scan for Patient 9 was taken at 11 days post-fracture. X-rays of the tibia on the date of the fracture, 11-Apr -93, both before and after the application of an external fixator are shown in Figures 3.14. and 3.15. respectively. From these Figures the size and configuration of the fracture can be clearly seen, which also showed up on the DXA scan.

Figure 3.14. X-ray of Patient 9 showing the anterior-posterior view and the medial-lateral view of the fractured tibia before fixation. 11-Apr-93.

Figure 3.15. X-ray of Patient 9 showing the anterior-posterior view and the medial-lateral view of the fractured tibia after fixation. 11-Apr-93.

The contra-lateral tibia of this patient was used as a control to compare with the fractured tibia (Figure 3.16.). The BMD along the length of the tibia had fallen to 71.1 % of the control value at 11 days post-fracture. There was a slightly greater reduction across the fracture site, with the BMD falling to 67.1 % of the control values. The BMD continued to fall along the length of the tibia until the scan taken in June, nearly 10 weeks post-fracture (Table 3.7.). The BMD was 42.2 % of the control across the

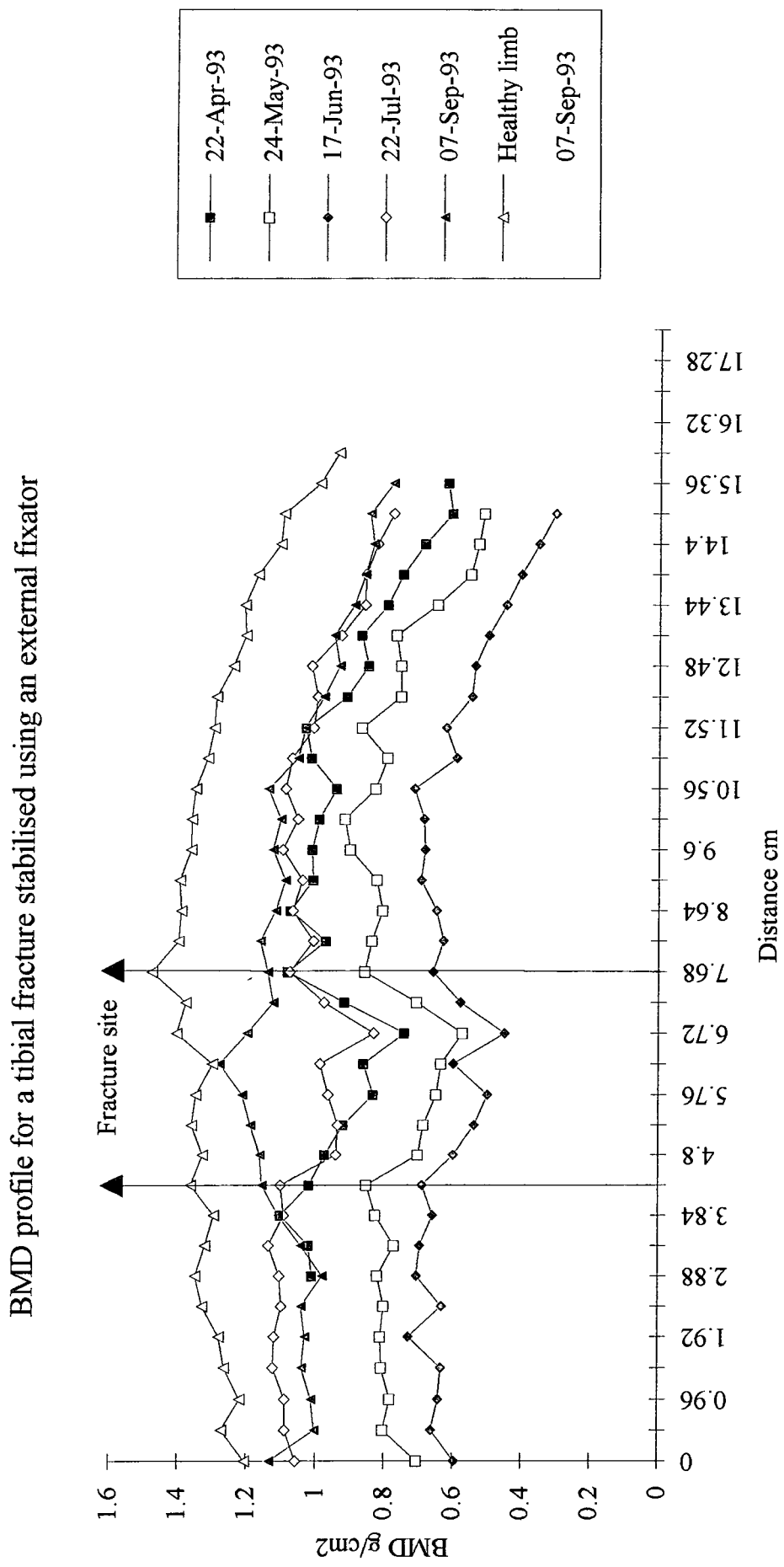

Figure 3.16. BMD profile for Patient 9 with an oblique mid shaft tibial fracture. The date of fracture was 11-Apr-93.

fracture site and 46.3 % for remainder of the tibia. The greater loss across the fracture site is probably due to necrosis and greater resorption at the fractured ends of bone.

% BMD compared to an equivalent region of interest on the unfractured limb. (Average ± 1 Standard deviation)						
Regions of interest.		22-Apr-93	24-May-93	17-Jun-93	22-Jul-93	7-Sep-93
Across the fracture site.	4.32 - 7.68 cm	67.1 ± 7.2 %	51.7 ± 6.6 %	42.2 ± 5.8 %	71.4 ± 6.2 %	86.6 ± 6.2 %
Near to the fracture site.	0.0 - 3.84 cm 8.16 - 15.36 cm	71.1 ± 7.1 %	59.8 ± 5.8 %	46.3 ± 7.3 %	80.1 ± 5.7 %	79.7 ± 4.5 %

Table 3.7. The BMD values along the fractured tibia of Patient 9 expressed as a percentage of the BMD values obtained at an equivalent location on the healthy contra-lateral limb on 7-Sep-93.

By examining the shape of the fracture healing profiles (Figure 3.16.) it can be seen that the fracture site was clearly visible and had a lower BMD than the surrounding bone until the scan in September. At this time a faster recovery of bone mineral at the fracture site had occurred than in the surrounding tibia. Across the fracture gap in September, over 21 weeks post-fracture, the BMD was 86.6 % of the equivalent region in the control tibia, whereas for the remainder of the tibia the BMD was 79.7 % of the control values. The callus at the site of the fracture therefore appeared to be undergoing a faster rate of mineralisation than the regions of bone away from the fracture site.

The BMD profiles of the unfractured healthy tibia for Patient 9 are shown in Figure 3.17. There is very little difference in the BMD values between each scan which have a coefficient of variation of 3.37 %, with the exception of the profile for 22-Jul-93. At the proximal end of the diaphysis, indicated between 0.0 cm and 6.24 cm on Figure 3.17. the BMD values are approximately 9 % higher than the average of the BMD

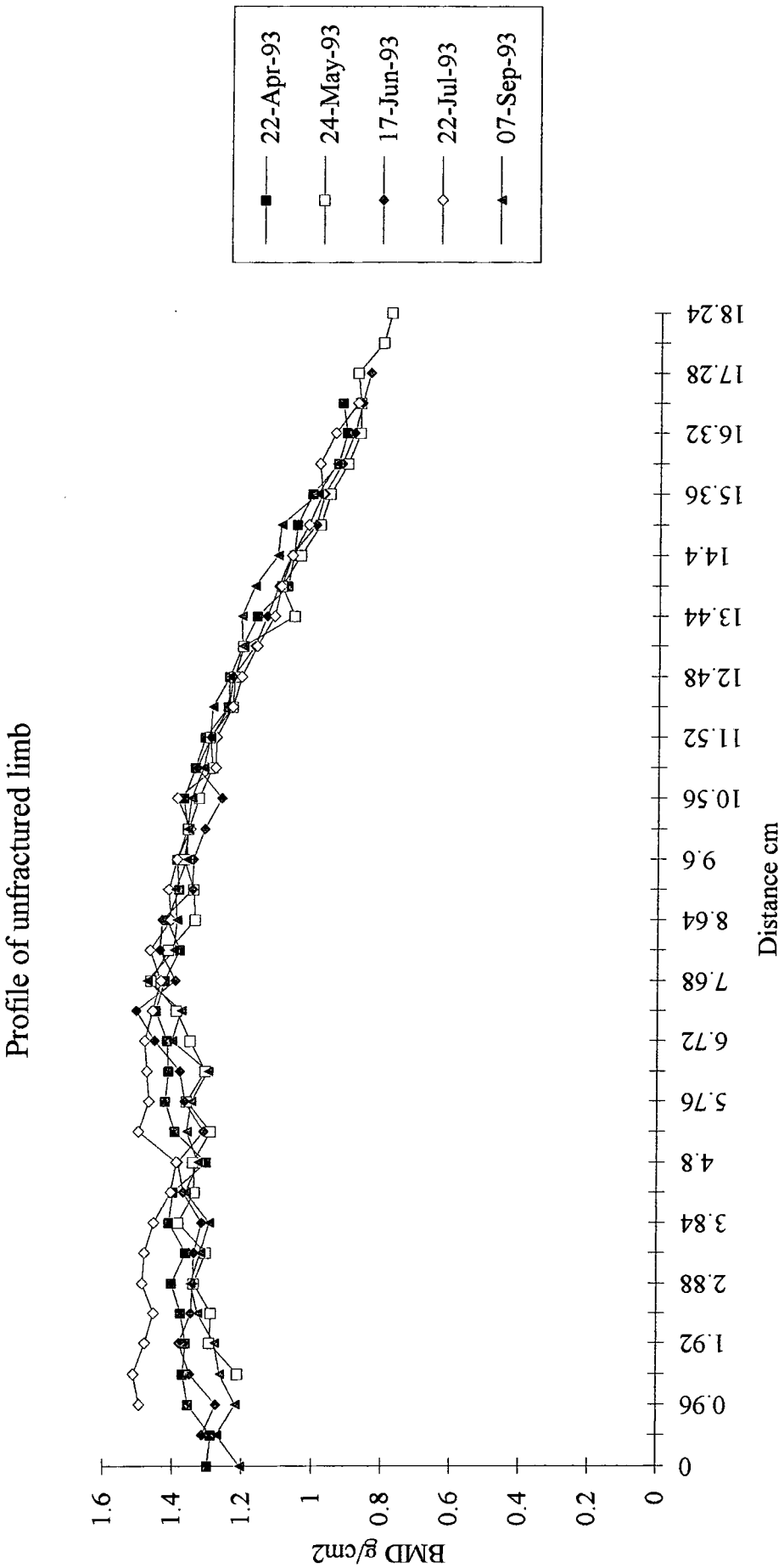

Figure 3.17. BMD profile for the unfractured tibia of Patient 9.

values in that region for the other scan dates. This is probably due to a slight variation in the positioning of the limb during the scan.

Patient 10

A scan of the healthy contra-lateral limb was available for this patient and was used to provide control values to compare with the BMD of the fractured tibia (Figure 3.18.). The first scan was taken 15 days post-fracture, and as in all the previous cases, there had been a marked drop in the bone mineral density values along the length of the tibia. The fracture site was clearly visible on the DXA scan and the BMD across the region of the fracture had reduced to 57.8 % of the equivalent part of the control limb (Table 3.8.). The bone mineral profile of the second scan in July, 6 weeks post-fracture appeared similar to the first scan. In the intermediate period there may have been a further decline in the bone mineral density values, followed by a gradual increase to the same level. Alternatively there may have been a stagnant period with no change. There was nothing noted in the medical records to indicate any complications and an increase in the BMD profile was seen in the scan taken in November.

% BMD compared to an equivalent region of interest on the unfractured limb. (Average ± 1 Standard deviation)				
Regions of interest.		21-Jun-93	20-Jul-93	2-Sep-93
Across the fracture site.	6.72 - 9.12 cm	57.8 ± 8.2 %	58.4 ± 5.6 %	81.5 ± 5.8 %
Near to the fracture site.	2.4 - 6.24 cm 10.56 - 14.88 cm	70.7 ± 3.3 %	70.5 ± 2.7 %	92.1 ± 3.8 %

Table 3.8. The BMD values along the fractured tibia of Patient 10 expressed as a percentage of the BMD values obtained at an equivalent location on the healthy contra-lateral limb on 2-Sep-93.

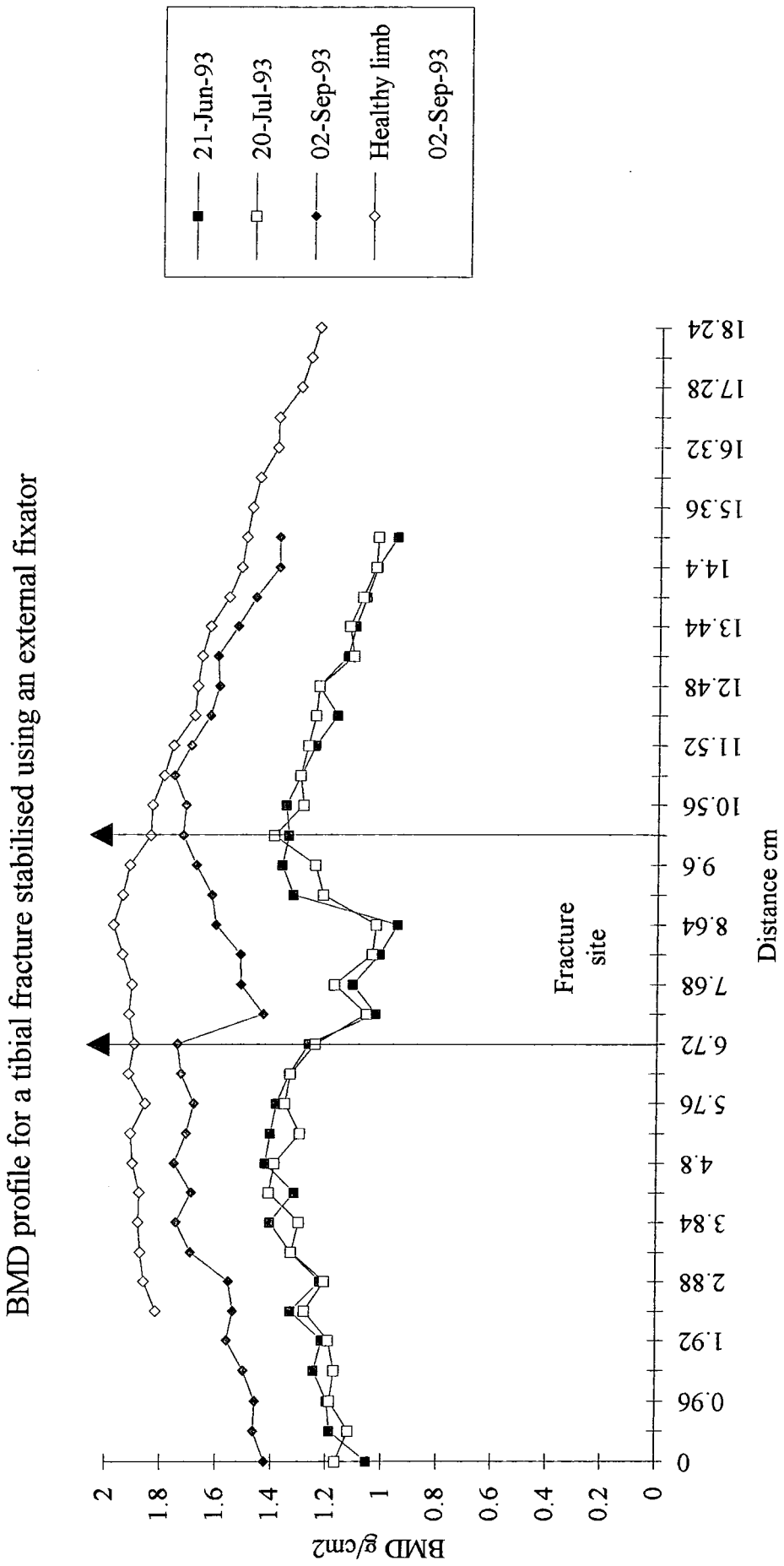

Figure 3.18. BMD profile for Patient 10 with an oblique mid shaft fracture. The date of fracture was 6-Jun-93.

For the scan taken in September, at 12 weeks post-fracture the BMD along the length of the bone was approaching control values. However, the location of the fracture site still showed a significantly lower BMD at 81.5 % of the control, the bone adjacent to the fracture site which was 92.1 % of the control values.

3.2.5 Internal Fixation

This section contains the results for Patient 2 and Patient 8 who had intramedullary nails for the management of their tibial fractures. Figure 3.19. shows the location of the standard and exclusion regions of interest for a patient with an intramedullary nail. No scans of the healthy limb were available for comparison with the fractured limb for these patients, but relative changes in BMD with time could be assessed.

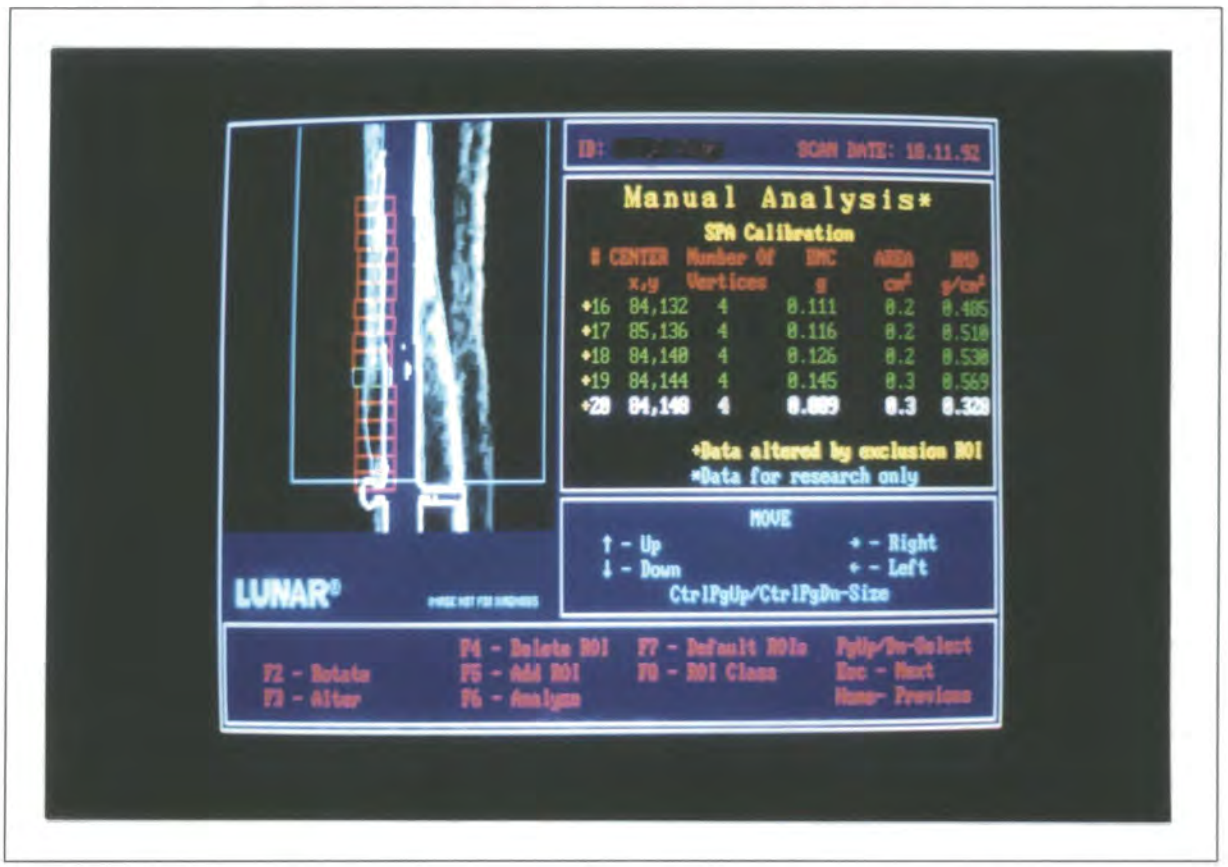

Figure 3.19. Lunar software computer display during analysis of Patient 2 with an intramedullary nail.

Patient 2

Change in BMD along the length of the tibia and across the fracture site with time were determined for this patient and the medial and lateral sides of the tibia, adjacent to the intramedullary nail were examined separately.

The first scan was taken 10 days post-fracture and although the fracture gap could be clearly viewed on the scan image, its position on the BMD profile of the lateral side could not be seen (Figure 3.20.). This is probably due to the angle and geometry of the fracture site. However, when the BMD changes across the fracture site were compared with the BMD changes distant to the fracture site, both relative to the first scan, marked differences in the rates of bone mineral resorption and deposition were seen for these different sites (Table 3.9.).

% BMD compared to an equivalent region of interest on 18-Nov-92. (Average ± 1 Standard deviation)				
Region of interest		15-Dec-92	14-Jan-93	10-Feb-93
Across the fracture site. Lateral side	12.0 - 16.32 cm	67.7 ± 7.9 %	91.0 ± 13.2 %	106.2 ± 18.2 %
Near to the fracture site. Lateral side	0.0 - 11.52 cm	66.8 ± 10.9 %	69.8 ± 10.0 %	54.8 ± 12.0 %
Across the fracture site. Medial side*	15.84 - 18.24 cm	112.7 %	132.7 %	168.5 %
Near to the fracture site. Medial side	0.0 - 15.36 cm	90.0 ± 8.3 %	71.3 ± 8.8 %	62.8 ± 6.3 %

Table 3.9. The BMD values along the lateral and medial side of the fractured tibia of Patient 2 expressed as a percentage of the BMD values obtained at the same location on 18-Nov-92. * The average values for the % change in BMD across the fracture site on the medial side are exaggerated for this patient as the reference BMD values are very low, hence any difference will appear as a large % change.

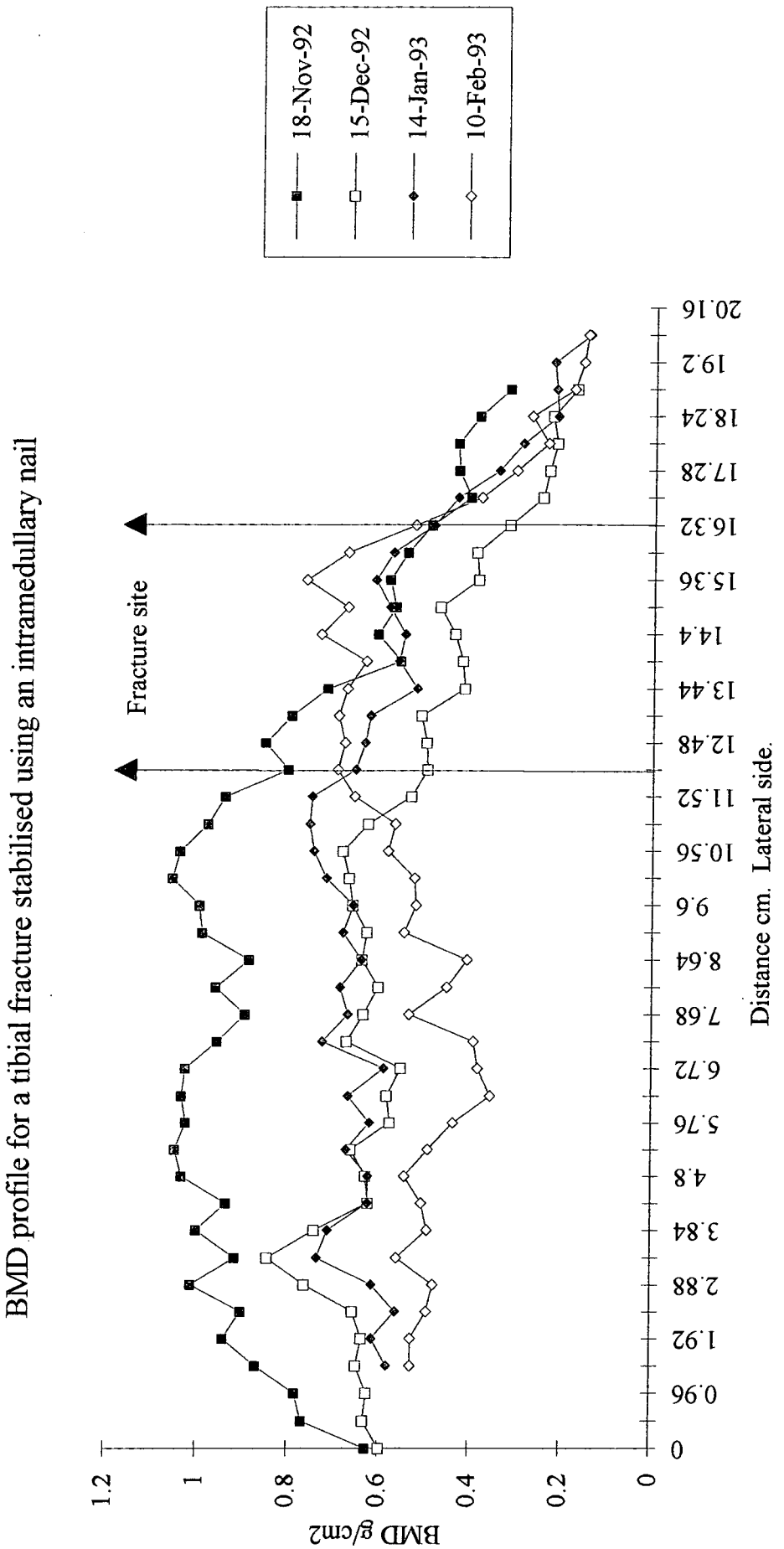

Figure 3.20. BMD profile for Patient 2 with a mid shaft spiral fracture. The date of fracture was 8-Nov-92.

Across the fracture gap on the lateral side, there was over a 30 % fall in the BMD between the first scan and the second scan in December, at 5 weeks post-fracture. However, for the third and fourth scan, at 9 weeks and 13 weeks post-fracture respectively, the BMD across the fracture gradually increased and exceeded the value measured during the first scan in November. There was also a decrease in the bone mineral density along the length of the tibia away from the fracture site which continued after the first scan in November, for every subsequent scan until February, falling to 54.8 % of the BMD value measured at the same area 3 months previously. A similar decline in the BMD along the length of the tibia was seen on the medial side of the tibia (Figure 3.21.), away from the fracture site, with values gradually falling to 62.8 % of the BMD values measured at the first scan. It would appear from Table 3.9. that there was a large increase in BMD across the fracture site between November and February, but although the percentage change may be large, the actual increase in BMD is less 0.01 g cm^{-2} over 3 months. The BMD profile for the medial side of the fractured tibia, across the fracture site, underwent very little change with time (Figure 3.21.). It was still clearly visible 3 months later on the DXA scan, whereas there was a substantial measured improvement in BMD of the fracture site on the lateral side. The geometry of the fracture was such that a much larger gap was present on the lateral side than the medial side of the tibia. As a result a greater period of time would be required for the bone mineral density of the lateral side of the tibia to be restored to pre-fracture levels, whereas on the medial side the fractured bone ends were almost adjacent.

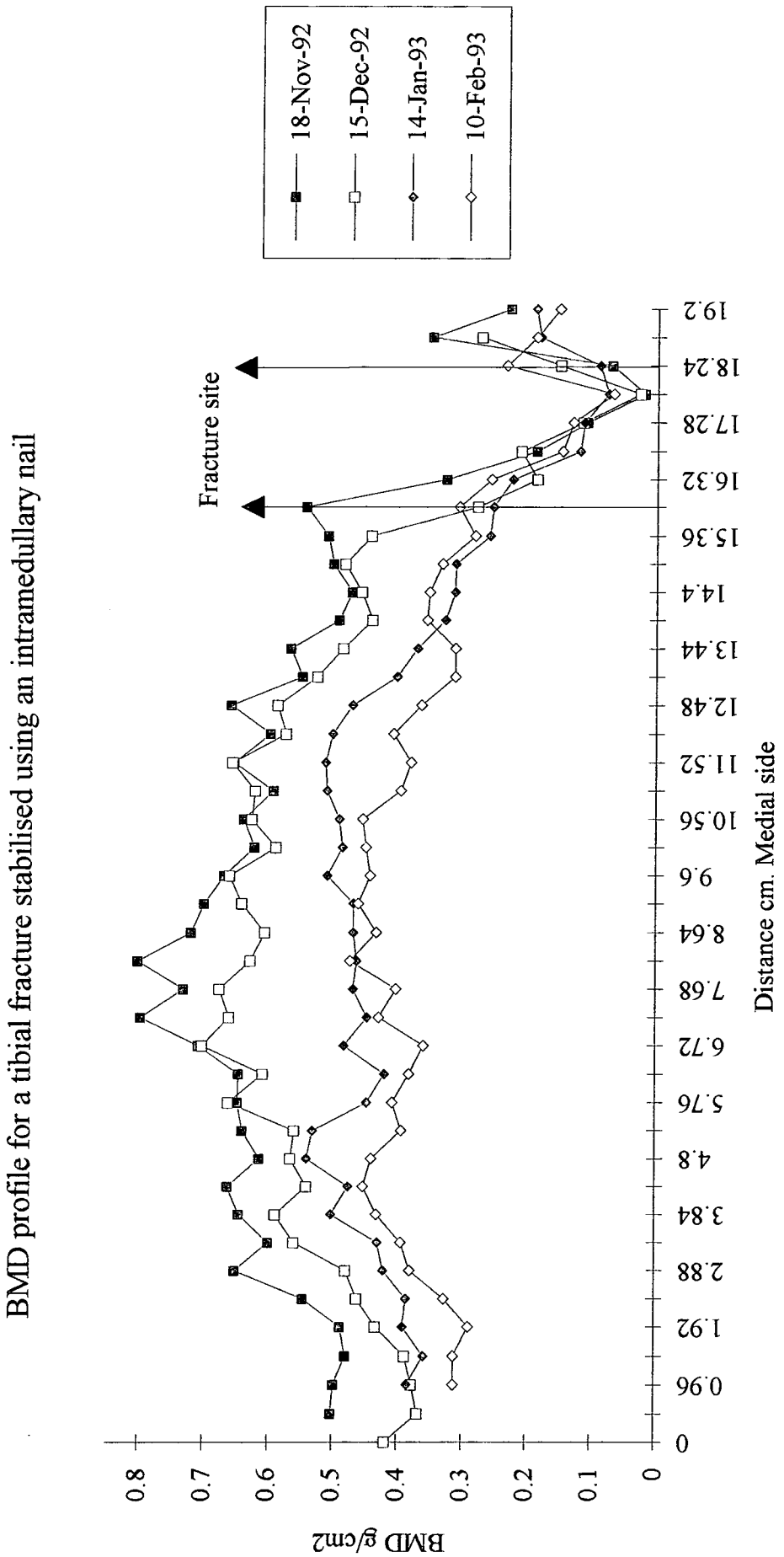

Figure 3.21. BMD profile for Patient 2 with a mid shaft spiral fracture. The date of fracture was 8-Nov-92.

Patient 8

No scan of the healthy contra-lateral limb was available for this patient, but in order to assess the relative changes in BMD along the length of the tibia with time, each scan was compared to the first scan obtained in November, at 25 days post-fracture. The lateral and medial side of the fractured tibia, adjacent to the intramedullary nail were analysed separately (Figures 3.22. and 3.23.). An x-ray of the fractured tibia taken on 15-Oct-92 and shows the extent of the injury before fixation (Figure 3.24.).

The average BMD for the lateral side of the fractured limb, across the fracture site exhibited over a 25 % reduction between the time of the first scan and the second scan (Table 3.10.). By January the BMD across the fracture gap had increased to values approaching those measured 12 weeks earlier at the time of the first scan. The x-ray taken of the fractured limb in January showed the formation of callus at the fracture site which seems to indicate progression towards union and compliments the findings using DXA. The scan taken in February demonstrated that the average BMD across the fracture site had exceeded the values obtained in November by 18.5 %. The rate of healing measured on the medial side of the tibia was faster than that measured on the lateral side, again probably due to the geometry of the fracture. On the lateral side of the tibia the fracture gap was much larger than on the medial side where the fractured bone ends were more closely aligned. From November, the BMD across the medial side of the fracture site steadily increased by 7.3 % in December, 39.6 % in January and 98.5 % in February, at 16 weeks post-fracture. The rate of mineralisation across the fracture site on the lateral side lagged behind the healing rate on the medial side, due to the large fracture gap present, requiring a greater quantity of new bone formation than the medial side to restore the BMD across the fracture site to pre-fracture values.

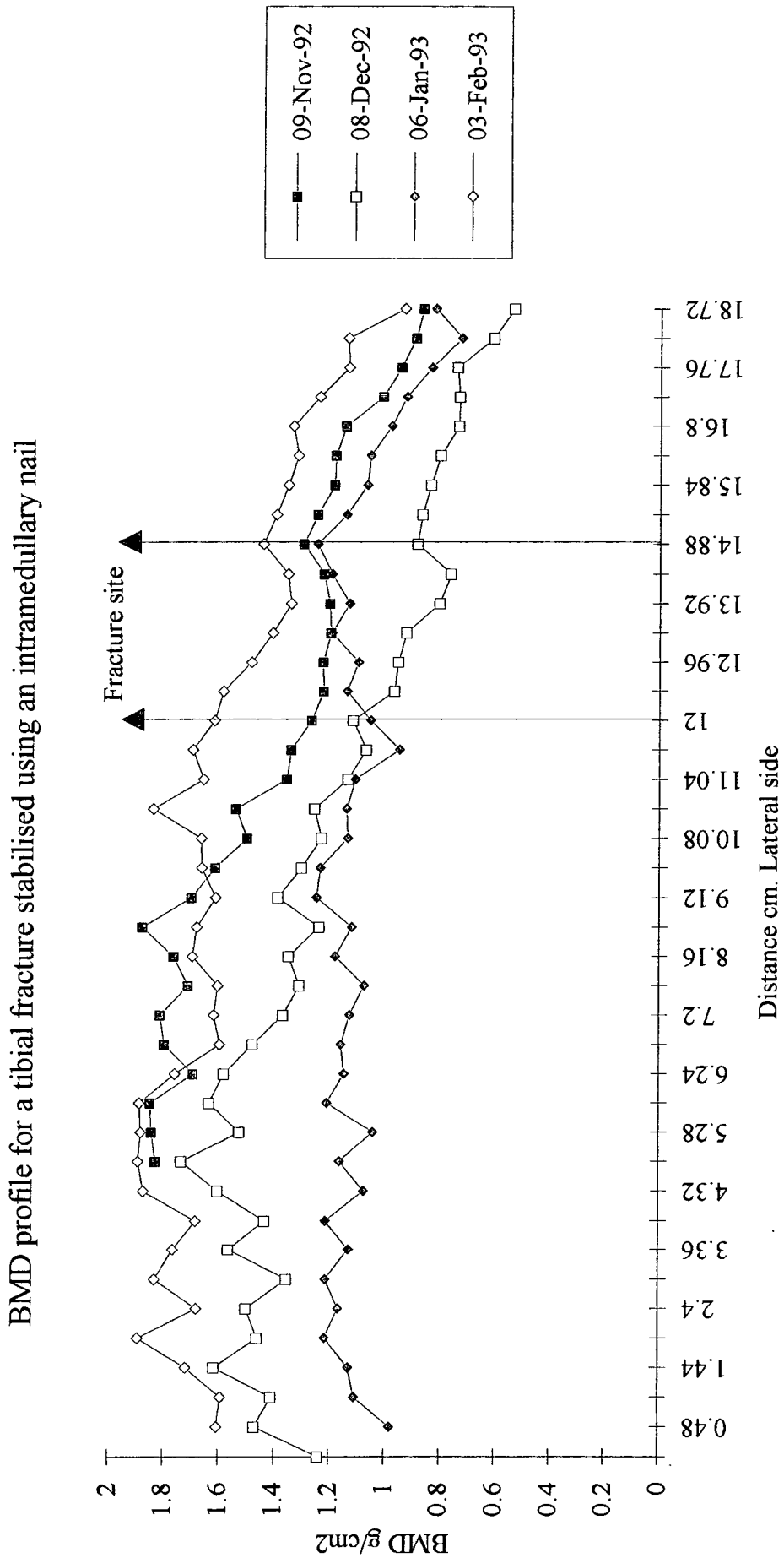

Figure 3.22. BMD profile for Patient 8 with a mid shaft spiral fracture. The date of fracture was 15-Oct-92.

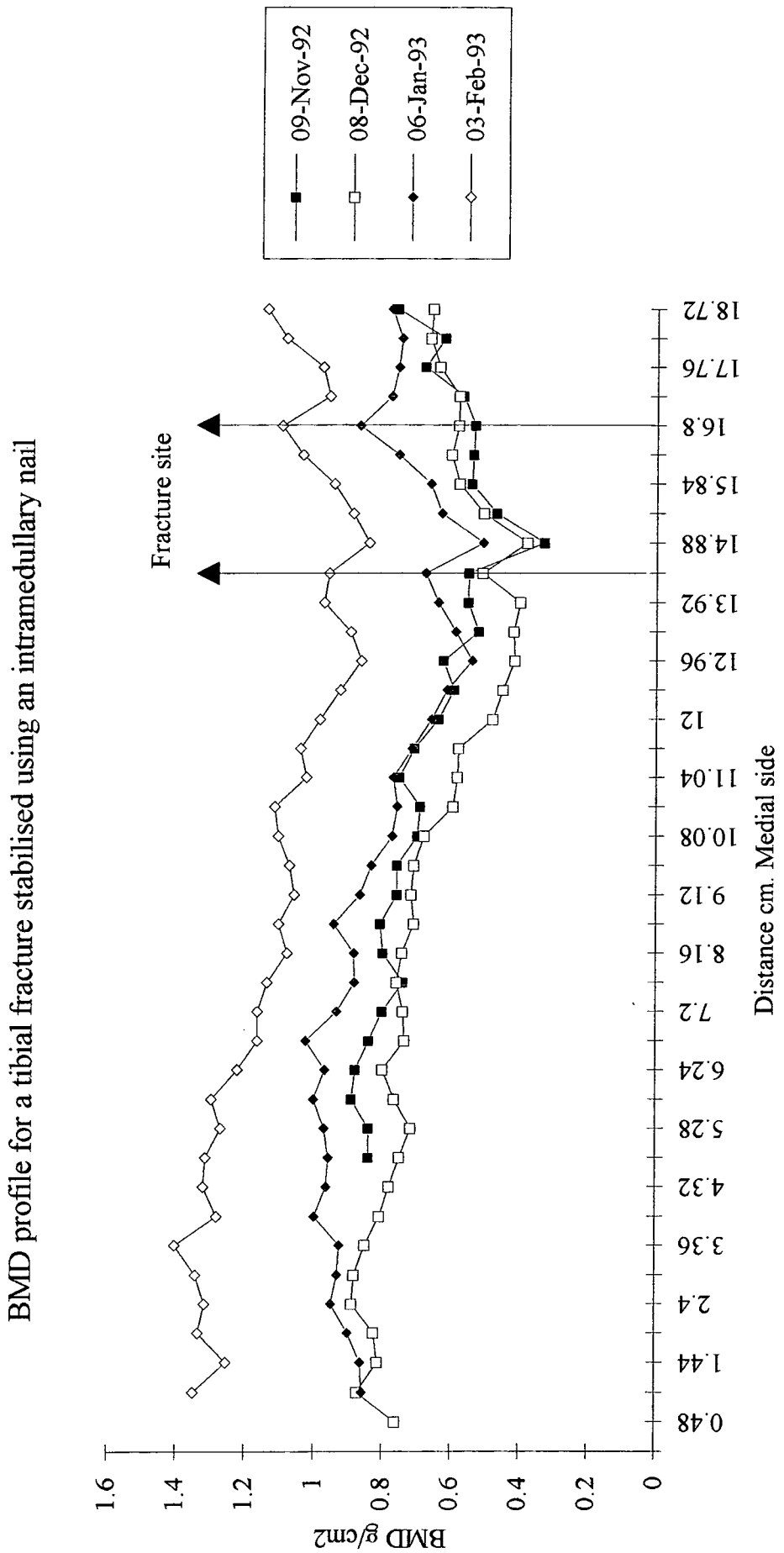

Figure 3.23. BMD profile for Patient 8 with a mid shaft spiral tibial fracture. The date of fracture was 15-Oct-92.

Figure 3.24. X-ray of Patient 8 showing the anterior-posterior view of the fractured tibia before fixation. 15-Oct-92.

% BMD compared to an equivalent region of interest on 09-Nov-92. (Average ± 1 Standard deviation)				
Region of interest		08-Dec-92	06-Jan-93	03-Feb-93
Across the fracture site. Lateral side	12.0 - 16.32 cm	74.2 ± 8.9 %	93.3 ± 5.6 %	118.5 ± 7.9 %
Near to the fracture site. Lateral side	0.0 - 11.52 cm	75.3 ± 9.5 %	78.1 ± 13.7 %	106.3 ± 10.8 %
Across the fracture site. Medial side	15.84 - 18.24 cm	107.3 ± 7.8 %	139.6 ± 6.6 %	198.5 ± 30.3 %
Near to the fracture site. Medial side	0.0 - 15.36 cm	88.4 ± 9.6 %	111.4 ± 9.6 %	149.6 ± 11.6 %

Table 3.10. The BMD values along the lateral and medial side of the fractured tibia of Patient 8 expressed as a percentage of the BMD values obtained at the same location on 15-Oct-92.

The remainder of the tibia, adjacent to the fracture site was slower at recovering bone mass than the area of bone at the fracture site. On the lateral side of the tibia the BMD continued to fall until the second scan in December. After this decline it began to gradually increase until February, when the measured bone mineral density was about 6 % higher than in November. The change in BMD on the medial side was slightly greater. The BMD only fell by 11.6 % from November to December, compared to the lateral side which decreased by 24.7 %. By February the BMD measured near to the fracture site on the medial side was nearly 50 % higher than the BMD of the same area measured the previous November.

Figure 3.25. X-ray of Patient 8 showing the anterior-posterior view of the fractured tibia at 3 months post-fracture. 8-Jan-93.

3.2.6 Complex Fixation

Patient 5 and 7 were included in this section due to the nature of the fixation devices applied, which both interfered with the collection of BMD data of the fractured tibia. Patient 5 was fitted with an Orthofix external fixator, with the addition of a screw across the fractured tibia to secure the fractured bone ends together. This screw completely obscured the site of the fracture, so analysis was carried out by using an exclusion ROI to eliminate the screw and standard regions of interest located along the length of the tibia as before. Patient 7 was fitted with an Ilizarov circular frame fixator. The large amount of metal associated with this type of fixator made positioning and analysing this patient difficult. However, analysis was carried out for the region of fractured tibia which could be seen through the Ilizarov frame (Figure 3.26.).

Figure 3.26. Lunar software computer display during analysis of Patient 7 with an Ilizarov frame.

Patient 5

No contra-lateral scan of the healthy limb was available for this patient (Figure 3.27.). From the BMD profiles obtained of the fractured tibia, the location of the fracture gap was not easily detectable. The fracture gap had a screw holding the bone ends together which partially obscured the fracture site. In addition the fracture was reduced such that the ends of the fractured bone were adjacent. Both of these factors make detection of the region of the fracture difficult. There was no significant change in BMD between the first and second scan. However, there was a drop of approximately 55 % in the BMD along the length of the tibia on the last scan when compared to the first scan. This reduction was slightly slower than that noted in the other patients with external fixators, which fell between 15 days and 9 weeks. The patient had reduced weight bearing in November because of pain in the limb and the reduction in BMD measured along the tibia may be a result of disuse osteoporosis.

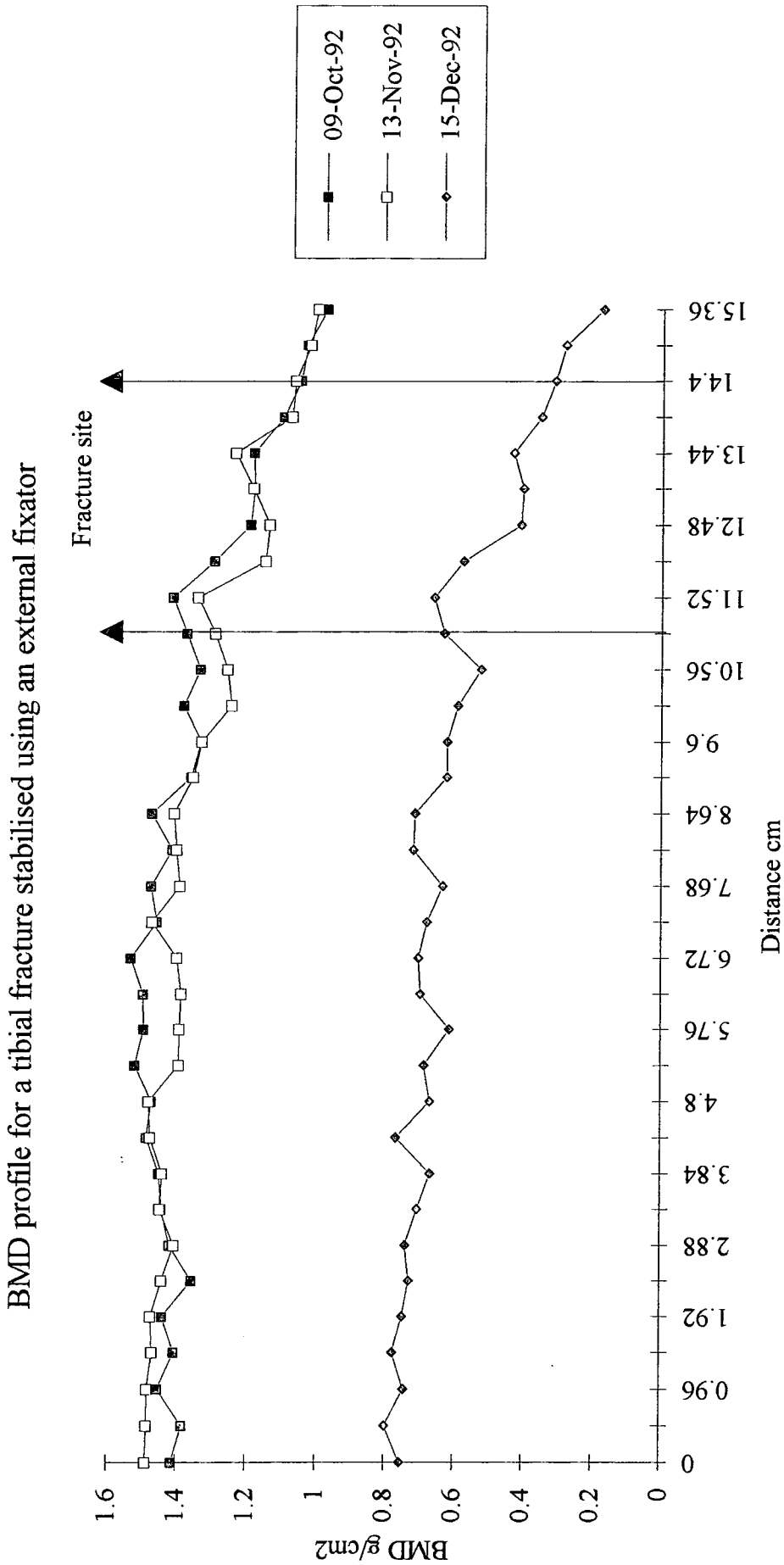

Figure 3.27. BMD profile for Patient 5 with a mid shaft tibial fracture. The date of fracture was 27-Sep-92.

Patient 7

The contra-lateral healthy for this patient was scanned and used as a comparison with the fractured tibia. Figure 3.28. shows an x-ray of the fractured limb before fixation. This patient's fracture was stabilised using an Ilizarov circular frame fixator which made analysis of the fractured tibia difficult, due to the metal frame and wires obscuring the scan image (Figure 3.29.). However the region of the fractured tibia which could be viewed was analysed and compared to the same area of the contra-lateral tibia (Figure 3.30.).

The BMD across the fracture site had fallen to 22.6 % of the BMD in the equivalent area of the unfractured tibia by the time of the first scan, taken 13 days post-fracture (Table 3.11.). This large decline in bone mineral was particularly emphasised due to the geometry of the break, and as a result the fracture site only crossed two regions of interest. There was an improvement in the quantity of bone mineral measured across the fracture site to 51.8 % in the December scan, taken 6 weeks post-fracture. However, the BMD remained relatively constant for the subsequent scans, at approximately 50 % of the equivalent region of the control limb.

Figure 3.28. X-ray of Patient 7 showing the anterior-posterior view and the medial-lateral view of the fractured tibia before fixation. 22-Oct-92.

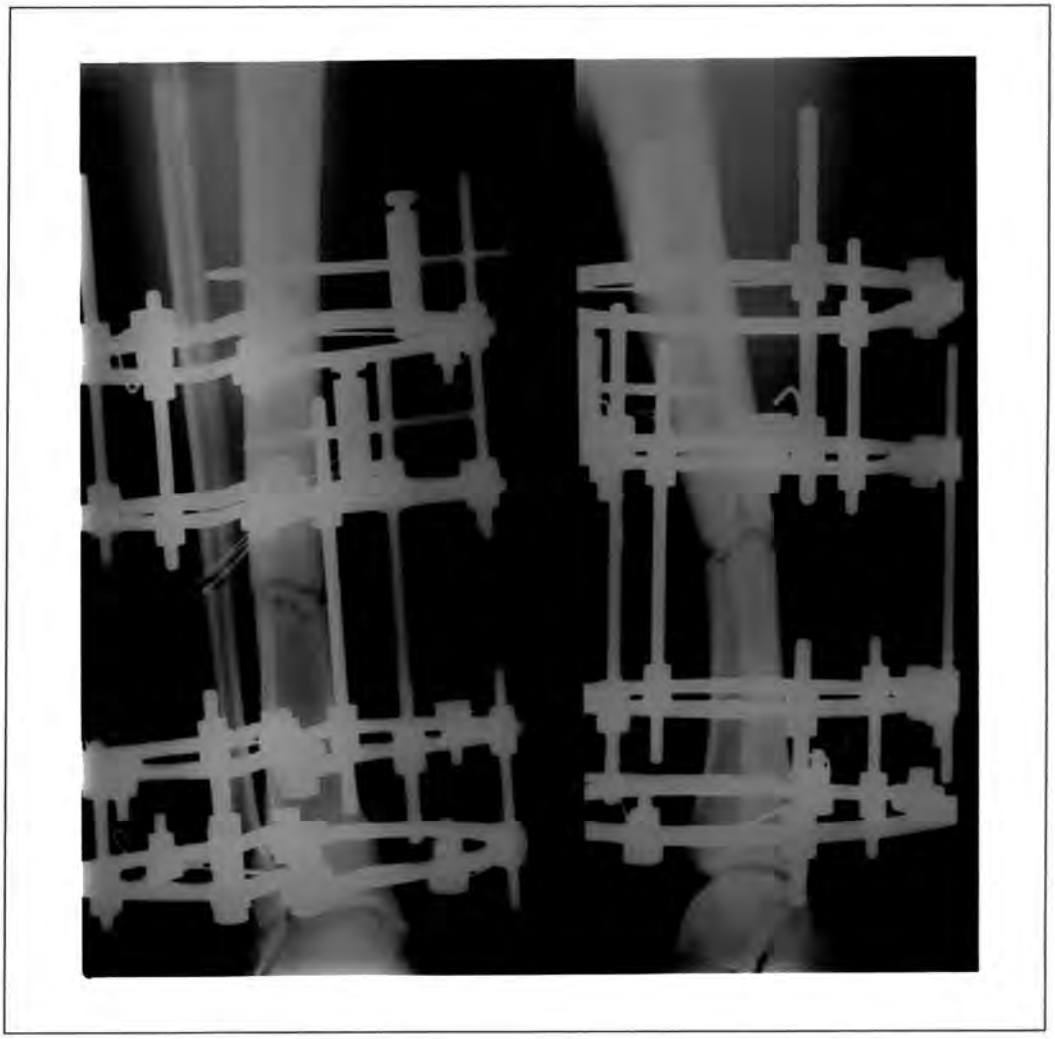

Figure 3.29. X-ray of Patient 7 showing the anterior-posterior view and the medial-lateral view of the fractured tibia after fixation with an Ilizarov fixator. 23-Oct-92.

% BMD compared to an equivalent region of interest on the unfractured limb. (Average ± 1 Standard deviation)					
Regions of interest.		04-Nov-92	02-Dec-92	06-Jan-93	03-Feb-93
Across the fracture site.	0.96 -1.44 cm	22.6 ± 1.3 %	51.8 ± 2.5 %	47.7 ± 2.8 %	50.9 ± 4.5 %
Near to the fracture site.	0.0 - 0.48 cm 1.92 - 4.32 cm	33.3 ± 8.0 %	58.6 ± 2.1 %	52.0 ± 2.7 %	56.5 ± 2.7 %

Table 3.11. The BMD values along the fractured tibia of Patient 7 expressed as a percentage of the BMD values obtained at an equivalent location on the healthy contra-lateral limb on 3-Feb-93.

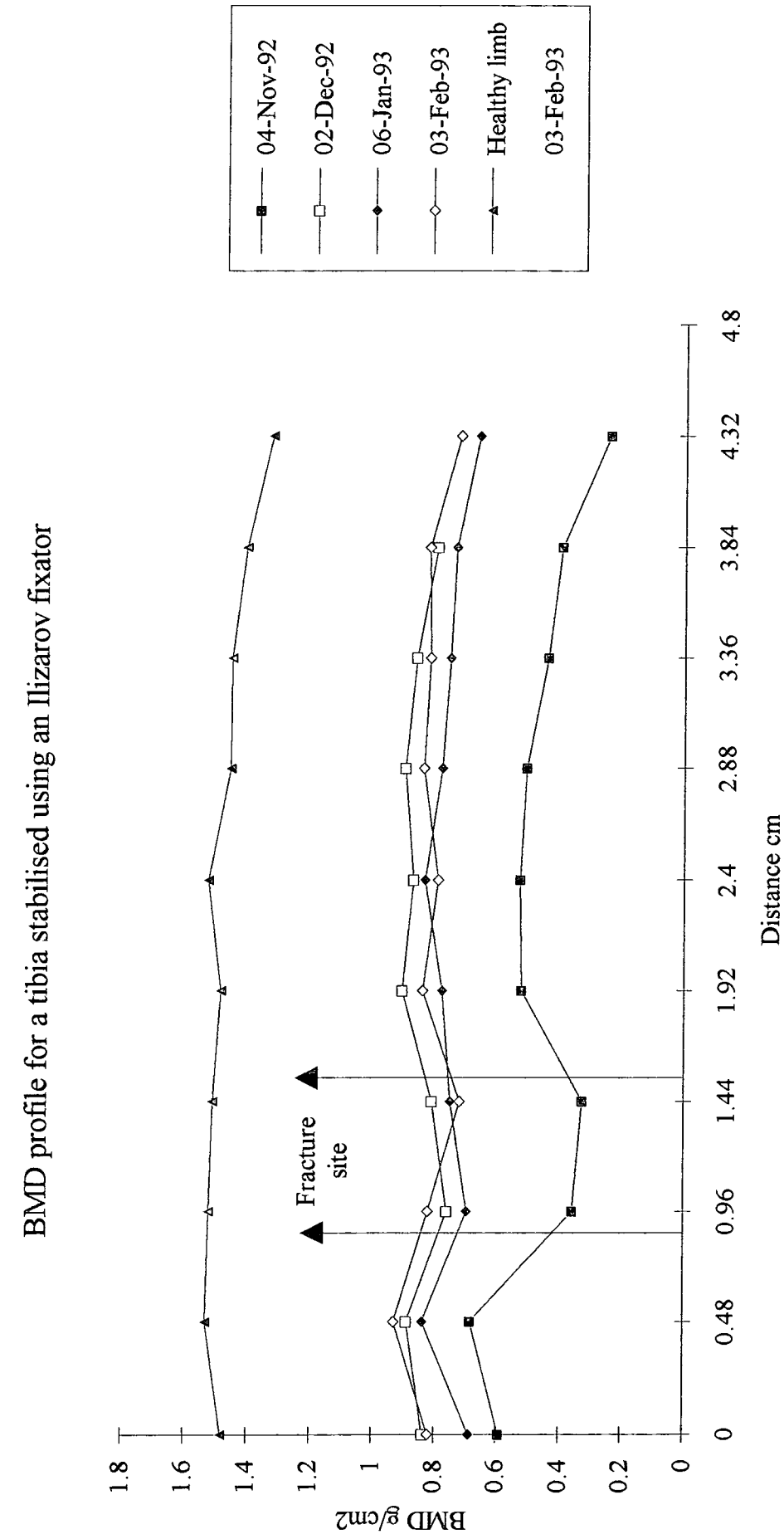

Figure 3.30. BMD profile for Patient 7 with a mid shaft transverse tibial fracture. The date of fracture was22-Oct-92.

The BMD measured in November, near to the fracture site also showed an initial decline to 33.3 % of the control tibia, although it was not as large as the fall across the fracture site. After the first scan, the BMD increased and remained between 52.0 % and 58.6 % of the control values for the following 3 scans. There appeared to be little improvement in the BMD along the length of the tibia during the final 3 months of the study. The difference in bone mineral across the fracture site and the area of bone adjacent was fairly small, approximately 5 %. After the last scan the Ilizarov frame was removed and the patient fitted with a plaster cast. With improved weight bearing it is likely that the BMD along the length of the tibia would increase.

CHAPTER 4

Discussion

To assess the potential of using DXA in the evaluation of tibial fracture healing, trials were undertaken on aluminium and hydroxyapatite phantoms to determine the accuracy, sensitivity and reproducibility of the DXA measurements. Using aluminium phantoms to simulate transverse and oblique tibial fractures it was found that the DXA machine could detect the presence of gaps of less than 0.05 mm, independent of the fracture gap's orientation. In a clinical situation the fracture is unlikely to be orientated such that it is parallel to the path of the photon beam and it was important to determine whether the BMD across a fracture gap could be monitored regardless of its size or orientation.

Excellent repeatability of the aluminium phantom results was achieved with a coefficient of variation of 1.1 %. The mass of small samples of calcium hydroxyapatite were found to be closely correlated ($r^2 = 0.99$) with the value of bone mineral content given by the scanner for samples weighing between 0.15 g and 0.53 g. The DXA machine and software were designed for monitoring the unfractured forearm, hence it was important to establish that small areas of low bone mineral density could be accurately measured. Areas of low bone mineral density, which one might expect across a fracture site, could be detected down to a BMD value of 0.16 g cm^{-2}, the BMD for an area of the distal tibial shaft being 0.9 g cm^{-2} for an unfractured tibia (Eyres *et al.*, 1993 (a)). In addition, a protocol for the patient analysis was developed and the optimum size for a region of interest was established.

14 Patients with tibial fractures were monitored during the fracture healing study. They were studied at 4 week intervals following trauma. Of these 14 patients, 8 were treated with external fixators and 6 were treated with intramedullary nails. It was found during the early patient trials that in order to obtain accurate and reproducible results using DXA, that only the forearm software could be used and not the orthopaedic software. The values of BMD obtained from analysing a patient with the orthopaedic software were erratic and the image of the scan displayed on the computer screen was not clear. This is probably due to the orthopaedic software being designed for scanning the proximal femur, where the thickness of the soft tissue present is significantly greater than that at the tibia and also the software expects to see an orthopaedic implant present in the scan path. Consequently the BMD at regions of interest along the tibial shaft was analysed using the forearm software supplied with the DXA machine. Anatomical landmarks were used to relocate the regions of interest between scans, the metal implant was excluded from the regions of interest using exclusion ROIs and using this method good reproducibility was obtained. The short term coefficient of variation was 3.36 % and the long term coefficient of variation was 4.13 %. The long term repeatability of BMD results for a patient trial carried out by Ulivieri *et al.* (1990) obtained using a DPA machine for the analysis of fractured tibiae was 5.4 %, which compares favourably with the results obtained in this study.

A summary of the results obtained for all of the patients treated with external fixation is given in Table 4.1. All of the patients exhibited a fall in BMD along the length of the tibia, typically reaching a minimum value between 1 and 9 weeks post-fracture. The loss of bone mineral from the tibia was greater nearer to the fracture, with the largest percentage of bone mineral lost across the fracture site, this probably being due to necrosis and resorption of bone at the fracture ends. The effect of disuse osteoporosis (Le Veau, 1992) and increased bone resorption in response to the fracture (Sarangi *et al.*, 1993), are the factors most likely to have affected the loss of BMD along the length of the bone, distant from the fracture site. The minimum BMD recorded at the

Summary of BMD changes, compared to the control limb, of the fracture study patients with external fixation.					
Patient number	Region of interest	Minimum BMD [1] (%)	Time to minimum BMD [2] (weeks)	Maximum BMD [3] (%)	Time to maximum BMD [4] (weeks)
1	Fracture site	18.1	1-6	100.0	23
	Near to fracture	26.6		100.0	
	Distant to fracture	55.0		101.5	17
3	Fracture site	21.3	2-6	122.8	18
	Near to fracture	37.5		104.2	
	Distant to fracture	42.9		104.3	
4	Fracture site	37.7	3-8	70.9	13
	Near to fracture	53.1		85.4	
9	Fracture site	42.2	6-9	86.6.	21
	Near to fracture	46.3		79.7	
10	Fracture site	57.8	2-6	81.5	15
	Near to fracture	70.7		92.1	
6	Fracture site	35.1	2-5	45.1	17 [5]
	Near to fracture	58.3		77.9	

Table 4.1. Summary of the patient results for the fracture healing study. [1]The minimum BMD is expressed as a % of the value obtained for the non-fractured contra-lateral limb. [2]The time to minimum BMD is the period of time post-fracture for which a decrease in BMD was likely to have occurred between scans. [3]The maximum BMD measured during the fracture healing study is expressed as a % of the non-fractured healthy contra-lateral limb. [4]The time to maximum BMD is the period of time post-fracture at which the maximum BMD was observed. [5]The time to maximum BMD was observed 8 weeks post-fracture and declined gradually to the values given 17 weeks post-fracture when delayed union was diagnosed.

fracture site was 18.1 % of the value obtained for the control limb and the minimum recorded away from the fracture site was 42.9 %. The minimum bone mineral distant to a tibial shaft fracture, measured using SPA by Andersson *et al.* (1979) was 45 % of the value obtained of the control limb.

All of the patients with external fixation who progressed to union demonstrated a gradual increase of bone mineral, following the initial decline along the length of the bone, which continued until the end of the measurements. By examining the BMD profiles for each patient, it appears that the BMD along the length of the tibia would rise until it approached pre-fractured values, after which there was increased mineralisation at the fracture site and BMD values in this area would often exceed the pre-fracture levels. During this study a BMD 22.8 % higher than the pre-fracture value was measured across the fracture site 6 weeks after the removal of an external fixator. Janes *et al.* (1993) observed for 13 patients with plated tibial fractures that the mineralisation across the fracture site exceeded the mineral content at an equivalent area of the unfractured contra-lateral tibia by approximately 20 % after union had been clinically diagnosed and 2 weeks after the plate had been removed. Only two patients had their fixators removed during the course of the study. Patient 1 had their external fixator removed at around 17 weeks post-fracture when the bone mineral density across the fracture site was 85 % of the control limb values. Patient 3 had the fixator removed 15 weeks post-fracture when the bone mineral density across the fracture site was about 103 % of the control limb values. Both of these patients had BMD profiles at the time of removal of the fixator on which the fracture gap was indistinguishable from the BMD profile of the normal unfractured tibia.

DXA can be used to accurately measure bone mineral density changes in patients and detect atypical healing trends in patients with fracture complications. Patient 5 had reduced weight bearing for one month during the study due to pain in the limb. This reduced activity was reflected by a simultaneous period of continued low bone mineral

density, probably due to disuse osteoporosis, along the length of the tibia, whereas the trends exhibited by the other patients in the study indicated that the BMD levels should be gradually increasing at this stage during the fracture healing process. Patient 6 who eventually required a bone graft to treat a delayed union clearly showed no significant improvement in BMD over a 3 month period. Despite a small rise in the BMD measured in the second month post-fracture, the actual bone mineral density across the fracture site was significantly lower than the surrounding bone and failed to show a significant increase for 3 months, indicating insufficient bone regeneration (Table 4.1). Three months post-fracture delayed union was diagnosed and a bone graft was carried out. This observation implies that it may be possible to diagnose delayed union at an early stage using DXA and that a change in treatment or surgical intervention could occur sooner, thus improving the rehabilitation time for the patient.

A summary of the results for both of the patients treated with intramedullary nails, who experienced no complications is given in Table 4.2. Both of the patients exhibited a fall in BMD along the length of the tibia, but at different rates depending on the location of the region of interest. It appeared that the BMD across the fracture site declined the most rapidly, reaching a minimum value approximately 4 or 5 weeks before the BMD at regions away from the fracture site, probably due to bone necrosis and resorption of the fractured bone ends.

Following an initial decline lasting about 10 weeks, the BMD increased along the length of the tibia, a larger increase being observed across the fracture site than distant from the fracture site, probably due to mineralisation of the fracture callus. For both patients, the rate of mineralisation at the fracture site was faster on the lateral side of the tibia than on the medial side and when the BMD profile of the last scan was examined, the location of the fracture site was not visible on the lateral side of the tibia, whereas on the medial side the fracture site was still evident. This was probably due to the geometry of the fracture for each of these patients, where there was a much

larger gap present on the lateral side than the medial side of the tibia. As a result, a greater period of time would be required for the bone mineral density of the lateral side of the tibia to be restored to pre-fracture levels.

Summary of BMD changes of the fracture study patients with intramedullary nails and without complications.				
Patient number	Region of interest.	Time to minimum BMD [1] (weeks)	Visible fracture gap [2]	Time to maximum BMD [3] (weeks)
2	Fracture site Lateral side	5-10	No	14
	Near fracture Lateral side	10-14	-	-
	Fracture site Medial side	5-10	Yes	14
	Near fracture Medial side	9-14	-	-
8	Fracture site Lateral side	4-8	No	16
	Near fracture Lateral side	4-8	-	16
	Fracture site Medial side	0-4	Yes	16
	Near fracture Medial side	4-8	-	16

Table 4.2. Summary of the patient results for the fracture healing study. [1]The minimum BMD is the period of time post-fracture for which a decrease in BMD was likely to have occurred between scans. [2]The visible fracture gap was assessed on the last scan profile. [3]The maximum BMD is the period of time post-fracture at which the maximum BMD was observed.

The rate of mineralisation across the fracture site for patients with internal fixation was slower than for patients treated with external fixation. The slower rate of recovery observed in the patients with intramedullary nails may be due to the high rigidity of the nail discouraging callus formation (Rockwood *et al.*, 1984.) and perhaps also due to the greater disruption to the cortical blood supply caused by the insertion of the nails

(Whittle *et al.*, 1992). Neither of these patients had their intramedullary nail removed during the course of the study.

The two patients with complex fixation, which had metalwork obscuring certain areas of the fractured tibia, were still able to be analysed using the DXA machine. Exclusion ROIs were used to eliminate the areas of metal from the regions of interest located along the length of the tibia. Similar time dependant changes in BMD were observed for each patient with complex fixation, as was seen in patients treated with standard external fixation. However, the BMD results obtained for these patients, were limited to areas of the tibia which were not obscured by the metalwork of the fixation devices, the fracture site of Patient 5 was obscured by a screw and only a small area of the tibia was visible for Patient 7 who was treated with an Ilizarov external fixator.

The time to removal of the external fixator would seem to depend primarily upon the bone mineral density across the fracture site having reached a certain value, where it is indistinguishable from the BMD profile of the tibia. For the two patients who progressed to union and had their external fixators removed, the bone mineral density across the fracture site was between 85 % and 103 % of the equivalent position on the unfractured contra-lateral limb prior to removal of the fixator. For each patient treated with an external fixator, the bone mineral density values across the fracture site expressed as a percentage of the same location on the unfractured contra-lateral limb, with time post-fracture, are shown in Figure 4.1. To give an indication of the typical rate of mineralisation across the fracture site with time, a straight line was fitted to the data obtained for the patients without complications (Patients 1,3,4,9,10). Obviously a linear relationship cannot perfectly describe the rate of healing for every patient, as the severity of the injury and method of fixation will affect the results, but it does however give an indication of the values of BMD which could be expected during the uncomplicated healing of a patient with an external fixator monitored in this study. The linear equation predicts that the BMD across the fracture site will reach 100 % of

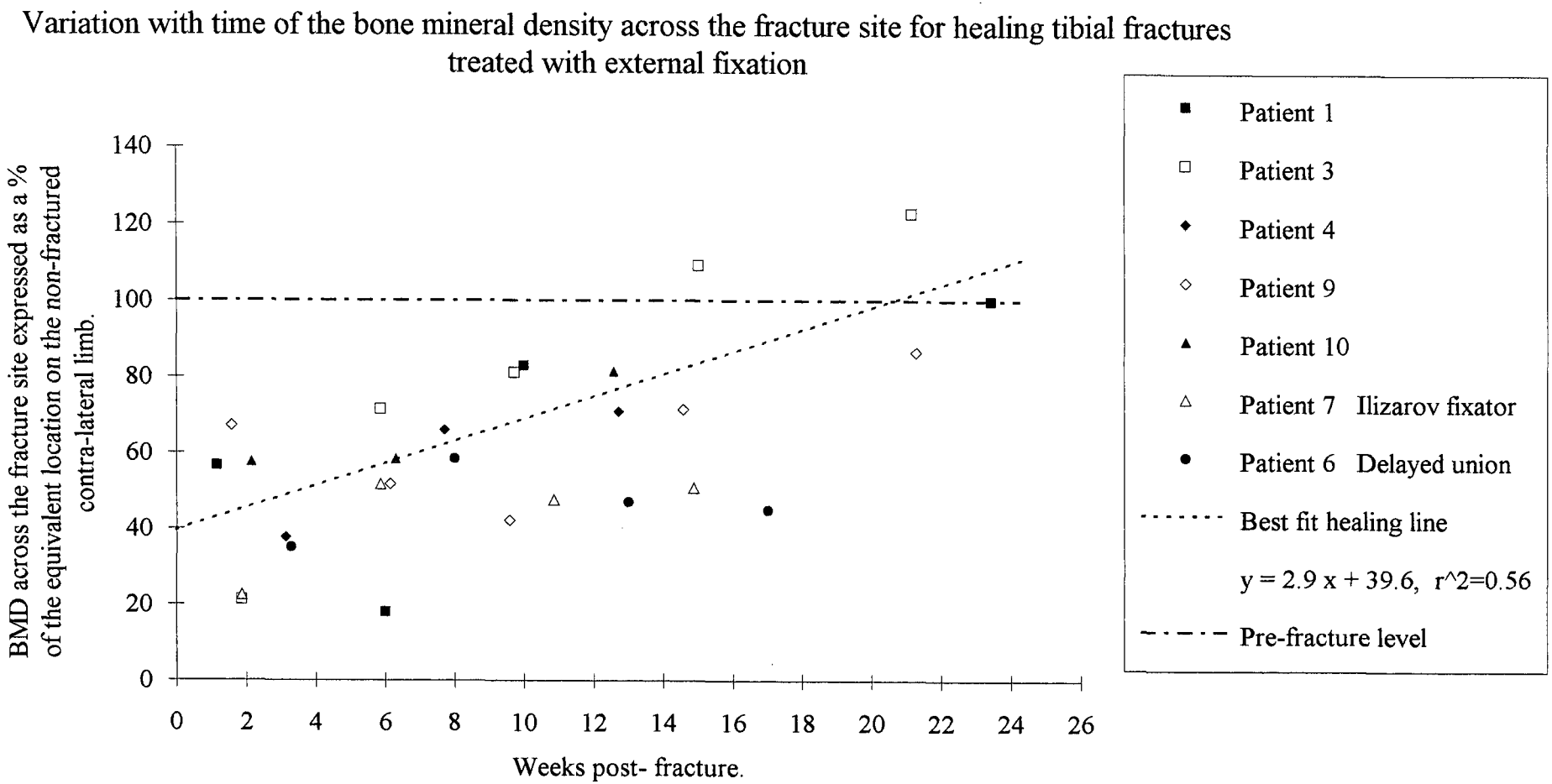

Figure 4.1. Graph showing the variation of BMD across the fracture site with time. A best fit line was fitted using the least squares method, to the data for patients 1, 3, 4, 9, 10, with uncomplicated tibial fractures treated with external fixators.

the control limb at 21 weeks post-fracture. To achieve the BMD values of between 85 % and 103 % when clinical healing was diagnosed in this study, the time post-fracture predicted by Figure 4.1. is between 16 and 22 weeks. At 10 weeks post-fracture it is quite clear that the BMD values of both the patient diagnosed with delayed union and the patient with the Ilizarov fixator, are below the values of the other patients treated with external fixation. This observation suggest that unsatisfactory fracture healing might be detected and treated as early as 10 weeks post-fracture. Figure 4.1. also provides a useful indication of when a fractured tibia is likely to have clinically healed or whether it is progressing towards delayed union.

Removal of the fixation device can occur when the fracture has healed sufficiently not to re-fracture on functional loading. The fracture stiffness should be high enough for the fractured limb to be able to withstand normal forces exerted by the muscles and weight bearing. Richardson *et al.* (1992) attempted to establish a threshold value of fracture stiffness at which independent weight bearing could be permitted and found that no refractures or angulation occurred in fractured tibias with a stiffness greater than or equal to 15 Nm degree^{-1}. Jernberger (1970) gave a mean value of stiffness for an intact male tibia to be 65 N m degree^{-1} and this suggests that a fracture can be said to have "healed" when its stiffness is about 25 % of that of an intact tibia bone. It has also been shown that stiffness is related to the mineralisation of the fracture gap (Currey, 1969) and *in vitro* studies have demonstrated that bone mineral density accounts for 80 % to 90 % of the measured variation of bone strength in intact bone (Mazess, 1990). The return of the ultimate strength of the fractured bone is an indication of the end of healing (Black *et al.*, 1984). However, there are many problems associated with measuring fracture stiffness *in vivo,* so a non-invasive measure of callus density could be used as an alternative method of predicting fracture stiffness and strength as fracture healing progresses. However, during this clinical study, healing of a tibial shaft fracture was diagnosed when the bone mineral density of the fracture site was between 85 % and 103% of the equivalent position in the

unfractured contra-lateral limb. From previous research, the stiffness of the fractured limb when clinical healing is diagnosed was approximately 25 % of the intact tibia (Richardson *et al.*, 1992). These findings would seem to indicate that the stiffness of the limb is not solely dependent upon the mineral content of the fracture callus. It has been reported that only 27 % to 29 % of the variation in rigidity of a long bone can be explained by the mineral content alone (Chakkalakal *et al.*, 1990). Factors in addition to the bone mineral such as the micro-structure and remodelling of the new bone will also affect the stiffness of the limb (Currey, 1969).

This study has demonstrated the viability of using DXA to accurately monitor changes in bone mineral density in and around a fracture site, for tibiae stabilised using either intramedullary nails or external fixators. DXA can be used to quantify the extent of mineralisation of the fracture site, which could be used as a useful predictor of healing, or impending delayed or non-union. Significant disuse osteoporosis was observed along the length of the tibia which can persist long after clinical healing of the fracture has taken place.

CHAPTER 5

Conclusions and Future Work

Aluminium and hydroxyapatite phantoms were used to simulate a fractured tibia, so that the sensitivity and accuracy of using DXA to monitor the healing of fractured tibiae could be assessed. It was demonstrated that the DXA machine was capable of detecting small fracture gaps of widths less than 0.05 mm, including transverse and oblique fractures orientated perpendicular and parallel to the path of the x-ray beam. The Lunar forearm software was able to accurately measure areas of low bone mineral density down to 0.16 g cm^{-2}, which one would expect to measure across a fracture site. Good reproducibility of results was obtained.

The patient scans were performed using the Lunar DPX-L scanner and the forearm software supplied with the machine. Regions of interest were located adjacent to each other along the length of the tibia and any metalwork present in the scan was eliminated by using exclusion regions of interest. Anatomical landmarks were used to relocate regions of interest between scans and using this protocol good repeatability of results was obtained, giving a long term coefficient of variation of 4.13 %. Poor results were obtained using the Lunar orthopaedic software, probably due to the software having been designed for scanning the proximal femur where a large thickness of soft tissue is present, whereas the tibia has a much smaller thickness of soft tissue.

All of the patients who were monitored during the fracture healing study, regardless of the fracture management method exhibited a fall in bone mineral density along the

length of the tibia, typically reaching a minimum value at between 1 and 9 weeks post-fracture which persisted for about 5 months, this being similar to that observed previously (Ulivieri *et al.*, 1990). This reduction in bone mineral density may be attributed to disuse osteoporosis (Le Veau, 1992) and partially to an increased rate of bone resorption triggered in response to the trauma (Wand *et al.*, 1992). The loss of bone mineral from the tibia was greater nearer to the fracture, with the largest percentage of bone mineral lost across the fracture site, probably due to bone necrosis and resorption.

It was possible, using DXA to detect atypical bone mineral density values during the study for patients with delayed union. These observations imply that it may be possible to diagnose delayed union at an early stage allowing surgical intervention or a change in treatment to occur sooner, thus improving the rehabilitation time for the patient.

The fracture healing study demonstrated the feasibility of using DXA to accurately monitor changes of bone mineral density in and around a healing fracture and can be used to quantify the extent of mineralisation of the fracture site and the significant osteoporotic changes caused by reduced mobilisation which can persist long after clinical healing of the fracture has taken place. For the two patients who progressed to union, the bone mineral density measured across the fracture site, prior to the external fixator being removed was between 85 % and 103 % of the equivalent position on the non-fractured contra-lateral tibia.

It would be useful to extend this study so that the initial patient scan is taken within the first two weeks and subsequent scans are performed at monthly intervals thereafter until the fracture has united and the patient has been discharged. The contra-lateral healthy limb should be scanned simultaneously to provide a reference with the fractured limb and to assess any changes, for example disuse osteoporosis which may occur in the unfractured tibia with time; however in this study no significant changes

were observed in the three patients for whom scans of the healthy limb were obtained during this study. The fractures should be monitored clinically and the bone mineral density changes correlated with the final clinical outcome. With this information it may be possible to define a time to union in terms of callus density. Since the mineral density of callus is related to the mechanical properties of bone it may be possible to infer the mechanical strength and stiffness of a healing fracture from this density (Aro *et al.*, 1989).

There are several methods of measuring the stiffness across a fracture, for example by measuring the deflection of the fracture resulting from a known load (Richardson *et al.*, 1992). Also techniques have been developed to measure the loading applied to a healing fracture (Kershaw *et al.*, 1993). Potentially if these measures of weight bearing and stiffness could be correlated with the bone mineral density values as healing progresses, a time may be defined in terms of these variables for the removal of the fixator and the correlation of these variables with clinical healing can be assessed.

It would also be useful to extend this study to examine the long term effect of fracture upon the bone mineral density of the tibia. Even after clinical union of the fracture, the bone mineral density along the length of the tibia is often lower than it was pre-fracture. Post-traumatic osteoporosis is thought to occur due to reduced functional loading of the limb (Le Veau, 1992) and increased bone resorption which occurs in response to the fracture (Sarangi *et al.*, 1993). By monitoring patients after successful clinical union of their fracture at say 6 month intervals, for a number of years, the long term effects of this disuse osteoporosis could be monitored since it is believed that post-traumatic osteoporosis could lead to permanent weakness of the bone and a predisposition to fracture (Wand *et al.*, 1992).

REFERENCES

AIRD EGA. *An introduction to Medical Physics.* Heinemann, London, 1975.

ALBRIGHT JA, BRAND RA. *The Scientific Basis of Orthopaedics, 2nd Ed.* Appleton & Lange, Connecticut, 1987: 161-212.

ALHAVA EM. Bone density measurements. *Calcified Tissue International* 1991; Supplement 49: 21-23.

ANDERSSON SM, NILSSON BE. Changes in Bone Mineral Content Following Tibia Shaft Fractures. *Clinical Orthopaedics and Related Research* 1979; 144: 266-229.

APLEY AG. *Apley's System of Orthopaedics and Fractures*, 6th Ed. Butterworths, UK, 1982: 331-368.

ARO HT, WIPPERMANN B, HODGSON S, WAHNER H, LEWALLEN D, CHAO E. Noninvasive monitoring of fracture callus mineralization using high-resolution single-photon absorptiometry. *34th Annual Meeting of Orthopaedic Research Society* 1988, USA: 415.

ARO HT, WIPPERMANN BW, HODGSON SF, WAHNER HW, LEWALLEN DG, CHAO EYS. Predictions of Properties of Fracture Callus by Measurement of Mineral Density using Micro-bone Densitometry. *The Journal of Bone and Joint Surgery* 1989; 71-A(7): 1020-1030.

AUCHINCLOSS JM, WATT I. Scintigraphy in the evaluation of potential fracture healing: A clinical study of tibial fractures. *The British Journal of Radiology* 1982; 55(658): 707-713.

BLACK J, PERDIGON P, BROWN N, POLLACK SR. Stiffness and strength of fracture callus: Relative rates of mechanical maturation as evaluated by a uniaxial tensile test. *Clinical Orthopaedics and Related Research* 1984; 182: 278-288.

BRANDRUP J, IMMERGUT EH. *Polymer Handbook*, 3rd Ed. Wiley, USA, 1989.

BRAUNSTEIN EM, GOLDSTEIN SA, KU J, SMITH P, MATTHEWS LS. Computed tomography and plain radiography in experimental fracture healing. *Skeletal Radiography* 1986; 15: 27-31.

CAMERON JR, SKOFRONICK JG. *Medical Physics.* John Wiley and Son, USA, 1978.

CARTER DR, BOULSEIN ML, MARCUS R. New approaches for interpreting projected Bone Density Data. *Journal of Bone and Mineral Research* 1992; 7(2): 137-145.

CHAKKALAKAL DA, LIPPIELLO L, WILSON RF, SHINDELL R, CONNOLLY JF. Mineral and Matrix contributions to Rigidity in Fracture Healing. *Journal of Biomechanics* 1990; 23(5): 425-434.

CULLITY BD. *Elements of X-ray Diffraction.* Addison Wesley, USA, 1967.

CURREY JD. The mechanical consequences of variation in the mineral content of bone. *Journal of Biomechanics* 1969; 2: 1-11.

DICKIE DL, GOLDSTEIN SA, FLYNN MJ, GE ZF, MATTHEWS LS. Vertebral rBMD distribution and fracture characteristics in vitro and in vivo results. *34th Annual Meeting of Orthopaedic Research Society* 1988, USA.

EGGER EL, GOTTSAUNER-WOLFF F, PALMER J, ARO HT, CHAO EYS. Effects of axial dynamization on bone healing. *The Journal of Trauma* 1993; 34(2): 185-192.

ELLIS H. The speed of fracture healing after fracture of the tibial shaft. *The Journal of Bone and Joint Surgery* 1958; 40-B(1): 42-46.

EYRES KS, BELL MJ, KANIS JA. Methods of assessing new bone formation during limb lengthening.[b] *The Journal of Bone and Joint Surgery* 1993; 75-B(3): 358-364.

EYRES KS, BELL MJ, KANIS JA. New Bone Formation during Leg Lengthening.[a] *The Journal of Bone and Joint Surgery* 1993; 75-B(1):96-106.

FOLKENS PA. *Human Osteology.* Academic Press, California, 1991: 10-26.

GAUTIER E, PERREN SM, GANZ R. Principles of internal fixation. *Current Orthopaedics* 1992; 6: 220-232.

GENANT HK, FAULKNER KG, GLÜER CC. Measurement of bone mineral density: Current status. *The American Journal of Medicine* 1991; 91 Supplement 5B: 49-53.

GENANT HK, GLÜER CC, FAULKNER KG, MAJUMDAR KG, HARRIS ST, ENGELKE K, VAN KUIJK C. Acronyms in Bone Densitometry. *The British Journal of Radiology* 1992; 65: 1148.

GILL PJ, BARR DA, MOLLAN RAB, GRAY R, CAMPBELL N. Conduction mode of ultrasound in bone. *Proceedings of Ultrasonic assessment of Bone II*, Harwell Biomedical Research, UK, 1992: 16.

GOLDSTEIN SA, WILSON DL, SONSTEGARD DA, MATTHEWS LS. The mechanical properties of human tibial trabecular bone as a function of metaphyseal location. *Journal of Biomechanics* 1983; 16(12): 965-969.

GOODSHIP AE, KENWRIGHT J. The influence of induced micromovement upon the healing of experimental tibial fractures. *The Journal of Bone and Joint Surgery* 1985; 67-B(4): 650-655.

GOODWIN PN. Methodologies for the Measurement of Bone Density and their Precision and Accuracy. *Seminars in Nuclear Medicine* 1987; 17(4): 293-304.

GRAY H. *Gray's Anatomy, 33rd Ed.* Longmans, UK, 1964.

HANGARTNER TN. Quantitative assessment of bone: Radiologic methods. *Current concepts of Bone Fragility.* Springer-Verlag, Berlin, 1986: 89-101.

HEPPENSTALL RB. *Fracture treatment and healing.* WB Saunders Co, USA, 1980.

HOLLINS M. *Medical Physics.* Macmillan, UK, 1991.

HUBBELL JH. Photon cross sections, attenuation coefficients and energy absorption coefficients from 10 keV to 100 GeV. *Current Constants / Physics and Chemistry of the Earth Sciences* 1982; 8: 22.

HUBBELL JH. Photon cross sections, attenuation coefficients and energy absorption coefficients from 10 keV to 100 GeV. *National Standard Reference Data System*; National Bureau of Standards 29, USA, 1969.

HUBBELL JH. Photon mass attenuation and energy-absorption coefficients from 1 keV to 20 MeV. *International Journal of Applied Radiation and Isotopes* 1982; 33: 1269-1290.

JANES GC, COLLOPY DM, PRICE R, SIKORSKI. Bone density changes after rigid plate fixation of tibial fractures. *The Journal of Bone and Joint Surgery* 1993; 75-B(6): 914-917.

JERNBERGER A. Measurement of stability of tibial fractures. *Acta Orthopaedica Scandinavica*, Supplement 135, Copenhagen, 1970.

JOHNSON J, DAWSON-HUGHS B. Precision and Stability of Dual-Energy X-ray Absorptiometry Measurements. *Calcified Tissue International* 1991; 49: 174-178.

JOHNSTON CC, SLEMENDA CW, MELTON LJ. Clinical use of bone densitometry. *The New England Journal of Medicine* 1991; 324(16): 1105-1109.

JONSON R. Mass attenuation coefficients, quantities and units for use in bone mineral determinations. *Osteoporosis International* 1993; 3: 103-106.

KALENDAR WA. A phantom for standardisation and quality control in spinal bone mineral measurements by QCT and DXA: Design considerations and specifications. *Medical Physics* 1992; 19(3): 583-586.

KAYE GWC, LABY TH. *Tables of Physical and Chemical Constants, 15th Ed.* Longman, UK, 1986.

KELLIE SE. Measurement of bone density with dual-energy x-ray absorptiometry (DEXA). *Journal of American Medical Association* 1992; 267(2): 286-294.

KENWRIGHT J. The principles of use of external fixation. *Current Orthopaedics* 1992; 6: 214-219.

KERSHAW CJ, CUNNINGHAM JL, KENWRIGHT J. Tibial external fixation, weight bearing and fracture management. *Clinical Orthopaedics and Related Research* 1993; 293: 28-36.

LANGTON CM. Recent Advances in the Ultrasonic Assessment of Bone. *Proceedings of Ultrasonic assessment of Bone II*, Harwell Biomedical Research, UK, 1992: 16.

LATTA LL, ZYCH GA. The mechanics of fracture fixation. *Current Orthopaedics* 1991; 5: 92-98.

LE VEAU BF. *Williams and Lissners Biomechanics of Human Motion, 3rd Ed.* WB Saunders Company, USA, 1992: 29-59.

LEWALLEN DG, ARO HT, CHAO EYS, BERQUIST TH, KELLY PJ. Noninvasive evaluation of bone healing using quantitative MRI imaging. *34th Annual Meeting of Orthopaedic Research Society* 1988, USA: 409.

LUNAR. *Technical manual.* Documentation version 7/91; DPX-L software version 1.2. Lunar Radiation Corporation, USA, 1991.

LUNAR. *Technical note #1 and #5.* Lunar Radiation Corporation, USA, 1988.

MACK PB, BROWN WN, TRAPP HD. The quantitative evaluation of bone density. *American Journal of Roentgenology* 1949; 6: 808-825.

MARKEL MD, WIKENHEISER MA, CHAO EYS. A study of fracture callus material properties: Relationship to the torsional strength of bone. *Journal of Orthopaedic Research 1990*; 8(6): 843-850.

MARKEY E, JURIST J. Tibial resonant frequency measurements as an index of the strength of fracture union. *Wisconsin Medical Journal* 1974; 73: 62-65.

MAZESS RB, CHESTNUT CH, McCLUNG M, GENANT HK. Enhanced Precision with Dual-Energy X-Ray Absorptiometry. *Calcified Tissue International* 1992; 51: 14-17.

MAZESS RB, COLLICK B, TREMPE J, BARDEN HS, HANSON J. Performance Evaluation of a Dual-Energy X-Ray Densitometer. *Calcified Tissue International* 1989; 44: 228-232.

MAZESS RB, BARDEN HS, BISEK JP, HANSON J. Dual-energy x-ray absorptiometry for total-body and regional bone-mineral and soft-tissue composition. *American Journal of Clinical Nutrition* 1990; 51: 1106-1112.

MAZESS RB. Bone Densitometry for Clinical Diagnosis and Monitoring. In: *Osteoporosis: Physiological Basis, Assessment and Treatment.* (Editors: DeLuca HF and Mazess RB) Elsevier Science Publishing Co, USA, 1990: 63-85.

McKIBBIN B. The biology of fracture healing in long bones. *The Journal of Bone and Joint Surgery* 1978; 60-B(2): 150-162.

MOW VC, HAYES WC. *Basic Orthopaedic Biomechanics.* Raven Press, USA, 1991: 93-142.

MÜLLER ME, ALLGÖWER M, SCHNEIDER R, WILLENEGGER H. *Manual of Internal Fixation, 3rd Ed.* Springer-Verlag, Berlin, 1991.

NICOLL EA. Fractures of the tibial shaft: A survey of 705 cases. *The Journal of Bone and Joint Surgery* 1964; 46-B(3): 373-387.

NILSSON BER. Post-traumatic Osteopenia: Quantitative study of the bone mineral mass in the femur following fracture of the tibia in man using americium-241 as a photon source. *Acta Orthopaedica Scandinavica* 1966; 91 (37): 14-24.

ONI 00A, HUI A, GREGG PJ. The healing of closed tibial shaft fractures. *Journal of Bone and Joint Surgery* 1988; 70-B: 787-790.

PAN WT, EINHORN TA. The Biochemistry of Fracture Healing. *Current Orthopaedics* 1992; 6: 207-213.

PANJABI MM, WHITE AA, SOUTHWICK WO. Temporal changes in the physical properties of healing fractures in rabbits. *Journal of Biomechanics* 1977; 10: 689-699.

PARTHASARADHI K, ESPOSITO A, PELLICCIONI M. Photon attenuation coefficients in tissue equivalent compounds. *Applied Radiation and Isotopes* 1992; 43(12): 1481-1484. International Journal of Radiation Applications and Instrumentation, Part A.

PELTONEN JI, KAHRI AI, LINDBERG LA, HEIKKIL PS, KARAHARJU EO, AALTO KA. Bone formation after distraction osteotomy of the radius in sheep. *Acta Orthopaedica Scandinavica* 1992; 63(6): 599-603.

PERREN SM, BOITZY A. Cellular Differentiation and Bone Biomechanics during the Consolidation of a Fracture. *Anatomical Clinica* 1978; 1: 13-28.

PYE DW. Estimation of the magnitude of the error in Bone Mineral measurements due to fat: The effect of Machine Calibration. *Clinical Physics and Physiological Measurement* 1991; 12(1): 87-91.

RADIN EL. *Orthopaedics for the Medical Student.* JB Lippencott, Philadelphia, 1987: 9-34.

RICHARDSON JB, KENWRIGHT J, CUNNINGHAM JL. Fracture Stiffness measurement in the Assessment and Management of Tibial Fractures. *Clinical Biomechanics* 1992; 7: 75-79.

ROCKWOOD CA, GREEN DP. *Fractures in adults, 2nd Ed.* JB Lippencott Company, USA, 1984; 147-167, 1593-1663.

ROOS B. Dual photon absorptiometry in lumbar vertebrae. *PhD Thesis, University of Gothenburg,* Sweden, 1984.

SARANGI PP, WARD AJ, SMITH EJ, STADDON GE, ATKINS RM. Algodystrophy and Osteoporosis after Tibial Fractures. *The Journal of Bone and Joint Surgery* 1993; 75-B: 450-452.

SARTORIS DJ, MOSCONA A, RESNICK D. Progress in radiology: Dual-energy radiographic absorptiometry for bone densitometry. *Annals New York Academy of Sciences* 1990; 592: 307-325.

SCHAFFLER MB, BURR DB. Stiffness of compact bone: Effects of porosity and density. *Journal of Biomechanics* 1988; 21(1): 13-16.

SELIGSON D. *Concepts in Intramedullary Healing.* Grune & Stratton, Florida, 1985: 27-49.

SHARRARD WJW. A double-blind trial of pulsed electromagnetic fields for delayed union of tibial fractures. *The Journal of Bone and Joint Surgery* 1990; 72-B(3): 347-355.

SHIPMAN P, WALKER A, BIRCHELL D. *The Human Skeleton.* Harvard University Press, Massachusetts, 1985: 18-63.

SMITH MA, JONES EA, STRACHAN RK, NICOLL JJ, BEST JJK, TOTHILL P, HUGHS SPF. Prediction of fracture healing in the tibia by quantitative radionuclide imaging. *The Journal of Bone and Joint Surgery* 1987; 69-B(3): 441-447.

SONSTEGARD DA, MATTHEWS LS. Sonic diagnosis of bone fracture healing - A preliminary study. *Journal of Biomechanics* 1976; 9: 694-698.

SORENSON JA, DUKE PR, SMITH SW. Simulation studies of dual-energy x-ray absorptiometry. *Medical Physics* 1989; 16(1): 75-80.

SPOKAS JJ, WHITE DR. A conducting plastic simulating cortical bone. *Physics in Medicine and Biology* 1982; 27(1): 115-121.

STORM E, GILBERT E, ISRAEL H. Gamma ray absorption coefficients for the elements 1 through 100 derived from the theoretical values of the national bureau of standards. *Los Almos Scientific Lab Report* 1958: LA 2237.

TIEDEMAN JJ, LIPPIELLO L, CONNOLLY J, STRATES BS. Quantitative Roentgenographic Densitometry for assessing Fracture healing. *Clinical Orthopaedics and Related Research* 1990; 253: 279-286.

TOTHILL P. Methods of bone mineral measurement. *Physics in Medicine and Biology* 1989; 34(5): 543-572.

TUCKER FR. The use of radioactive phosphorus in the diagnosis of avasular necrosis of the femoral head. *The Journal of Bone and Joint Surgery* 1950; 32-B: 100-107.

ULIVIERI F M; BOSSI E; AZZONI R; RONZANI C; TREVISAN C; MONTESANO A; ORTOLANI S. Quantification by Dual Photon Absorptiometry of Local Bone Loss After Fracture. *Clinical Orthopaedics* 1990; 250:291-296.

WAHNER HW, DUNN WL, MAZESS RB. Dual photon (Gd 153) absorptiometry of bone. *Radiology* 1985; 156: 203-206.

WAND JS, SMITH T, GREEN JR, HESP R, BRADBEER JN, REEVE J. Whole-body and site specific bone remodelling in patients with previous femoral fractures: Relationships between reduced physical activity, reduced bone mass and increased bone resorption. *Clinical Science* 1992; 83: 665-675.

WEBB S. *The Physics of Medical Imaging.* Adam Hilger, UK, 1990.

WHALEN RT, CARTER DR, STEELE CR. Influence of Physical Activity on the Regulation of Bone Density. *Journal of Biomechanics* 1988; 21(10): 825-837.

WHITE DR, CONSTANINOU C, MARTIN RJ. Foamed epoxy resin-based lung substitutes. *The British Journal of Radiology* 1986; 59: 787-790.

WHITE DR, CONSTANINOU C. Phantom materials in radiology. In: *Encyclopaedia of Medical Devices and Instruments*, (Editors: Webster JG), Wiley, UK, 1988 (4): 2238-2254.

WHITE DR, MARTIN RJ, DARLISON R. Epoxy resin based tissue substitutes. *British Journal of Radiology* 1977; 50: 814-821.

WHITE TD. *Human Osteology.* Academic Press, USA, 1991.

WHITTLE AP, RUSSELL TA, TAYLOR CJ, LAVELLE DG. Treatment of Open Fractures of the Tibial Shaft with the use of Interlocking Nailing without Reaming. *The Journal of Bone and Joint Surgery* 1992; 74-B(8): 1162-1171.

WOLFF J. Das gaetz der transformation. *Transformation der knochen.* Hirshwald, Germany, 1892.

YOUNG DR, NIKLOWITZ WJ, STEELE CR. Tibial changes in experimental disuse osteoporosis in the monkey. *Calcified Tissue International* 1983; 35: 304-308.